Nonlinear Adaptive Control for Robust Wide Speed Range Operation of IPMSM Drives

by

Garin Matthew Schoonhoven

Submitted in partial fulfillment of the requirements
for the degree of Master of Science in Engineering

Lakehead University
Thunder Bay, Ontario

April 28st, 2015

Abstract

Various applications, including robotics, spindle drives, machine tools, etc. rely on accurate, reliable controllers to deliver the required drive performance. With recent advances in magnetic materials and semiconductor technology, machines such as the permanent magnet synchronous machine (PMSM) family of ac drives have seen a rise in popularity, owing to the high power density, efficiency and relative longevity as compared to conventional ac motors. In particular, interior permanent magnet synchronous machines (IPMSM) are characterized by all the features of the PMSM family, with the additional possibility of improved efficiency due to rotor construction, making them ideal for critical applications with high performance demands.

Notably, despite the advantageous aspects of PMSM motors in general, control of this class of ac machines is complex if full performance potential is to be realized. In order to achieve optimal efficiency while permitting wide speed range operation, it is crucial to design controllers that are capable of delivering this high performance. Due to the nonlinearity of magnetic flux distribution during operation, the parameters of the PMSM may vary significantly. Thus, a high performance controller must be capable of optimizing efficiency while maintaining excellent response characteristics from set-point or loading variations.

As a result of the nonlinear flux distribution caused by rotor/stator magnetic field interactions, direct control of PMSM in the stator reference frame is not possible as the level of mathematical complexity renders it infeasible. Expression of the PMSM stator variables in the rotating rotor reference frame permits the effective decoupling of machine variables into velocity and torque control components[1]. This is roughly analogous to separately excited direct current (DC) motors, where control of the rotor speed (field magnetization) and shaft torque (armature current) are decoupled as a function of the design. Analysis of the PMSM model in the rotating reference frame shows that the "d" and "q" axis currents are principally responsible for indirect air gap flux control and developed shaft torque, respectively.

---

[1] Note that this is a generalization, only the surface permanent magnet synchronous machine (SPMSM) model in the "dq" reference frame perfectly decouples into mutually exclusive velocity and torque components.

Traditional linear type control techniques based on proportional-integral-derivative (PID) controllers are able to achieve moderate success in controlling the PMSM family. The performance achieved is however typically within a narrow operational band and without the ability to adapt to parametric variation or optimize efficiency. This restriction makes PID type controllers non-ideal for more demanding applications that require highly accurate control and high efficiency regardless of load, temperature, machine age or operating environment.

Therefore, this thesis presents a robust nonlinear control algorithm utilizing an adaptive back-stepping technique with flux control for optimizing developed torque and improved operational range. Further, global asymptotic stability of the proposed controller is assured through Lyapunov's stability criterion in conjuncture with criterion supported by Barbalat's lemma. The proposed control algorithm ensures that the machine operates at precise command speeds, coping with system uncertainties and disturbances, while reducing losses and enabling operation over a wide speed range.

Simulation of the proposed system is carried out in MATLAB/Simulink, as well as in a co-simulation environment utilizing MATLAB/Simulink and PSIM. The first scenario implements an ideal mathematical system model with the controller in Simulink; whereas the second scenario uses PSIM to host the dynamic system model, with MATLAB/Simulink hosting the controller. This co-simulation permits rapid, accurate system analysis, by employing more accurate software models for switching elements, synchronous machine and any reactive elements not reflected in the basic mathematical model. Simulation results from both methods indicate excellent performance and robust operation, with excellent disturbance rejection.

Real-time implementation of the system is realized utilizing the DS1104 digital signal processor (DSP) in conjuncture with an IPMSM commutated by a three-phase two-level insulated gate bipolar transistor (IGBT) inverter, with a direct current (DC) generator as dynamic load. Performance of the proposed controller have been verified through experimental implementation for a range of operating conditions.

Acknowledgements

I would like to acknowledge and extend thanks to Dr. M. N. Uddin for his valuable support during my time at Lakehead University and in particular during the preparation of this Master's thesis. His guidance has been key to the completion of this thesis as well as related works and publications.

Thanks are also extended to those members of the engineering department involved in this thesis seminar and defense for dedicating their time and affording valuable feedback.

Special thanks are extended to Dr. K. Natarajan for his advice and availability throughout the Master's program; his insight has been greatly appreciated and essential to the completion of this work.

Table of Contents

List of Figures

List of Tables

List of Symbols

Symbol	Meaning
ϕ_{m}	rotor magnetic flux
R_s	stator resistance
n_p	machine pole pair
B_m	viscous friction coefficient
J	moment of inertia of machine rotor
L_d, L_q	d-q axis inductances
τ_{f}	frictional torque
τ_{m}	mechanical shaft load
τ_{e}	electrically induced torque
ω_{r}	machine angular shaft velocity
θ_{r}	machine shaft position
i_d, i_q	d-q axis (rotating reference frame) currents
I_s	peak per phase stator current magnitude
v_d, v_q	d-q axis (rotating reference frame) voltages
V_m /V_m	peak per phase stator voltage magnitude (rated)
i_{a}, i_b, i_c	phase currents (stationary reference frame)
v_{a}, v_b, v_c	phase voltages (stationary reference frame)
V_{DC}	DC link voltage
e_ω, e_d, e_q, e_D, e_Q, e_β, e_λ	error terms
k_ω, k_d, k_q, n_D, n_Q, n_β, n_λ	design coefficients
	adaptive law
	estimated parameter
	derivative operation
*	command value
f_{rated}	rated frequency
T_s	sampling frequency in real-time
m_a	amplitude modulation index
m_f	frequency modulation index

List of Abbreviations

Abbreviation	Meaning
DAC	digital to analog converter
DSP	digital signal processor
EMF	electromotive force
FP	floating point
FLC	fuzzy logic controller
FW	flux/field weakening
IEEE	Institute of Electrical and Electronic Engineers
IGBT	insulated gate bipolar transistor
IPMSM	interior permanent magnet synchronous machine
LMA	loss minimization algorithm
LUT	look-up table
MCU	microcontroller
MRAS	model reference adaptive system
MTPA	maximum torque per ampere
PCI	peripheral component interface
PI(D)	proportional integral (derivative)
PMSM	permanent magnet synchronous machine
PWM	pulse width modulation
QEI	quadrature encoder interface
RTI	real time interface
SMPS	switch mode power supply
SV(PWM)	space vector (pulse width modulation)

Chapter 1

Introduction

1.1 Research Background and Motivation

Advances in the fields of power electronics and high density permanent magnets have enabled significant improvements in motor drives technologies. The class of ac drives which has seen a particular rise in popularity due to advances in rare-earth magnetic alloys are referred to as interior permanent magnet synchronous machines (IPMSM). IPMSM construction involves a rotor with buried permanent magnets, providing magnetic saliency, high power density, robust construction and a small effective air gap [1]. The construction of the IPMSM rotor results in an additional torque component due to the rotor magnetic saliency (i.e. sinusoidal variation of inductance). It is this supplementary torque, known as reluctance torque which facilitates greater potential for optimal control and higher power density. This thesis work exploits the benefits of magnetic saliency of the IPMSM through adaptive nonlinear model based control, in order to deliver reliable and effective control over a wide speed range.

Precise control of IPMSM is complicated due to the nonlinear coupling among stator windings, magnetic saturation and consideration of the additional reluctance torque. This additional complexity in control design has resulted in many works disregarding the contribution of reluctance torque as a method of simplifying the control design [1], [2]. By disregarding the reluctance torque, it is possible to set the d-axis current (i_d) reference trajectory to zero which effectively forfeits reluctance torque and the mathematical torque expression becomes a singular linear function of q-axis current (i_q). Thus, setting the i_d reference trajectory to zero also has the effect of limiting motor operation to within rated speed, as indirect control of the air-gap magnetic flux it is not possible.

Consequently, the objective of this thesis is to address the deficiencies noted in the entirety of reviewed papers on the subject of nonlinear model-based control of IPMSM's, specifically regarding the application of flux control techniques.

1.2 Literature Review: Existing Control Techniques

This section of the thesis provides an overview of pertinent control techniques applicable to IPMSM drives and key aspects of each method. Significant research has been performed in the field of PMSM drives. As this thesis pertains specifically to IPMSM drives, research dedicated to this specific class of PMSM will be focused on. Major types of IPMSM drive controllers may be classed into the following categories, with each offering unique features and capabilities.

1. Fixed gain controllers
2. Model based controllers
3. Intelligent controllers

Typical motor drive systems employ a 2-level three phase voltage source inverter (VSI) for commutation of the motor stator phases, and thus a simplified diagram of this configuration is shown below in Figure. 1-1.

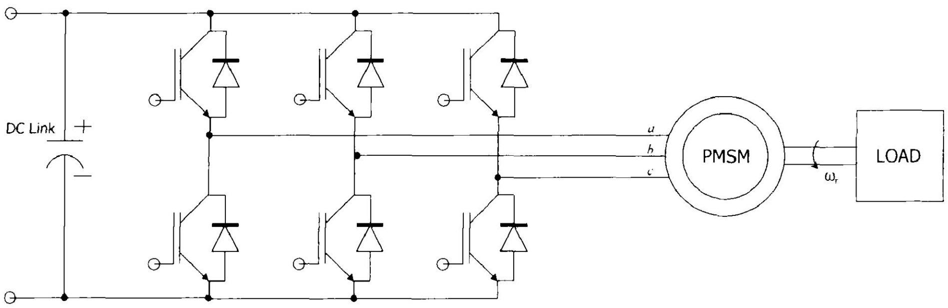

Figure 1-1: Typical 3-phase, 2-level inverter

1.2.1 Fixed Gain Controllers

Fixed gain controllers provide very simple control algorithms for IPMSM that are capable of providing accurate speed (or position) tracking given proper tuning. Proportional-integral-derivative (PID) type fixed gain controllers are among the most common, primarily due to ease of implementation and relative simplicity of tuning. However, in the role of forcing speed error convergence to zero (the most common use of PID control); fixed gain controllers based on PID control can entail significant tuning to achieve desired performance for each unique system, and within a defined operational band. If features such as efficiency optimization or loss minimization are required, additional algorithms are required and may be integrated in conjuncture with the PID control loop.

In [3] proportional-integral (PI) control is applied in the context of a model reference adaptive system (MRAS) for "sensorless" control of IPMSM, with multiple PI controllers for forcing the convergence of speed, and d-q axis current error dynamics. Similarly, in [4] a PI controller is used for forcing the speed error to zero in conjuncture with a MRAS for rotor speed estimation. In [5], the authors have proposed a PI stabilized controller based on maximum torque per ampere (MTPA) algorithm. Results shown indicate a significant improvement in efficiency relative to zero d-axis reference current. In [6], a PI speed controller is used in conjuncture with MTPA and flux weakening (FW) control algorithms to achieve improved performance both within and above rated speed. Similarly, in [7], [8] the authors have achieved wide speed range operation using PI controllers to force convergence of speed and quadrature currents error to zero, with flux control techniques to achieve improved operational range. Results shown indicate an improvement in efficiency through MTPA implementation, compared to zero reference d-axis current. In [9] the authors have implemented a PI speed controller with input-output feedback linearization to provide command voltages, simulation results are shown, however, with no comparison to other methods of control. The authors in [10] have proposed a loss minimization type controller which uses power loss models as a basis to define the d-axis current within rated conditions. A PI controller is used for speed reference tracking. Excellent efficiency results are reported in comparison to i_d =0 control, with an important factor being the saliency ratio (ratio of q/d axis inductances) of the subject machine, which was reported to be 2.61. Use of a PI controller greatly simplifies complexity, but the controller is not capable of parameter estimation, and stability is not mathematically demonstrated. In [11] fuzzy logic based online adaptation is performed to tune the fixed PI controller gains to ensure optimal performance, along with MTPA and FW control to enhance the operational range of the machine. Results reported indicate a performance improvement over conventional PI control, however, the authors provide minimal detail of integration of d-axis current control algorithms in the control development. Further, minimal tuning effort is directed towards the conventional PI controller benchmark (as it was noted to be "time-consuming"). In [12], indirect torque control is applied with an MTPA algorithm to provide a reference d-axis current, and using multiple PI controllers to force convergence of the error variables (i_d, i_q, τ_e). The results reported are in the context of vehicle drives, with the subject machine model exhibiting a high degree of rotor saliency with the saliency ratio equal to 3.45.

All of the works reporting on the usage of PI type control have shown excellent results, with comparatively simple implementation and tuning. PI controllers in the previously cited works have been implemented in the context of speed control, current control as well as in conjuncture with loss minimization algorithms and fuzzy logic controllers (as a principle tuning method). As noted previously, PI controllers can be highly effective, computationally efficient and may be integrated and/or complemented by or with other control algorithms to achieve improved performance. However, they are system specific and can require considerable tuning to achieve desired operation.

1.2.2 Model Based Controllers

Model based control provides the foundation for developing highly accurate control algorithms, with the potential for involving further techniques like adaptive backstepping as part of the control model development. Given that machine parameters are subject to variation over time, temperature and operational environments, a key aspect of model based control is the reliance on accurate knowledge of model parameters.

In [13], model based control is used, with stability of state variables shown using Lyapunov criterion. MTPA and FW algorithms are inserted for the d-axis current reference, notably however, the control development is done with the assumption that the d-axis reference current is set to zero. In [14], MTPA is integrated into the controller development, ensuring controller bounded state variables, and improving on [13], but limiting the permissible motoring speed range. In [1], model based nonlinear control is implemented with estimation of load torque in real time experiments. The inductance parameters (L_d, L_q) are estimated in simulation only, and thus negate the potential for further performance gains. Further, motoring operation is limited to within rated, as the d-axis reference current is set to zero for the simplification of control design. Similarly to [1], the authors in [15] have designed a nonlinear model based controller employing adaptive backstepping with Lyapunov stability theory; however, the subject machine is a surface permanent magnet synchronous machine (SPMSM), lacking reluctance torque and again the d-axis reference current is fixed to zero. The work reports excellent performance in simulation results, with detailed responses of estimated parameters and error dynamics. However the work does not perform any real-time analysis and does not compare to common competing control techniques. In [16], the authors achieve position control through adaptive nonlinear control, with a parameter estimation scheme similar to [1], [15]. Again, in this work, i_d is set to zero resulting in forfeiture of reluctance torque and flux control. Further, there are no real-time results published as a function of this work, or indeed comparisons to other control methodologies.

Many of the cited works on model based control employ some type of parameter adaptation, a feature which is essential to the stability and optimal performance of this type of control. Due to the relative complexity of the developed control, estimation and/or adaptation algorithms, the computational requirements are greater than that for typical PI controllers. Regardless, given the capacity of existing embedded systems with integrated floating point (hard float) math modules this is not problematic. Model based nonlinear controller enable highly accurate control, fast responses with adaptive control and enable the use of efficiency optimization algorithms. Due to the inherent complexity of the controller development, this type of control requires significant system and mathematical knowledge for design, yet offers the capacity for superior disturbance rejection and long term performance.

1.2.3 Intelligent Controllers

Intelligent controllers may be developed on the basis of expert knowledge of a system, applied through fuzzy logic (FL), neural networks and hybrid forms like adaptive neuro-fuzzy inference systems (ANFIS). The principal benefit of intelligent type controllers is that they function without any model, and thus are insensitive to parametric variation. A further advantage is that fuzzy membership functions may be configured for the generation of both d and q-axis current references, fully utilizing features of the IPMSM and enabling accurate control without knowledge of system parameters.

In [11], a comparison of PI and FL controller performance is made to illustrate the performance differences. A fuzzy controller is employed to provide a reference for d-axis current enabling flux control, as well as for providing tuned/adaptive gain multipliers for the q-axis current PI controller gains. Improved response of the proposed controller is demonstrated experimentally over a conventional PI controller (with non-optimized gains), and demonstrates an example of hybrid control (i.e. combination of multiple control techniques). In [2] a fuzzy logic controller (FLC) in conjuncture with a loss minimization algorithm (LMA) is employed with a hysteresis current controller to achieve control. Performance and efficiency is compared to traditional PI control, and various simulation scenarios illustrate the benefits of the loss minimization algorithm (LMA). Real-time results confirm performance of the proposed controller, however do not make a comparison to other competing control methods. In [17] a simplified FLC is developed in conjuncture with an MTPA algorithm, simulation results presented compare a scenario with and without the MTPA algorithm, indicating the improved performance by using a nonzero d-axis current reference. Real-time results conclude the same, demonstrating the performance of the FLC, with results as expected for a d-axis current reference algorithm. In [18] a PI type FLC is implemented with the use of genetic tuning algorithms to achieve improved performance by optimizing the fuzzy rule base. Simulation results indicate a performance improvement over conventional (not optimized by genetic tuning) FLC, with speed response improving slightly. The control is achieved through the use of hysteresis current controller, real-time results are not presented. The authors in [19] implemented a Takagi-Sugeno (TS) type FLC speed controller, with results presented for both simulation and real-time. Speed responses illustrated excellent stability under parametric variation, with the FLC controller demonstrating superior performance to the conventional PI controller, in terms of speed overshoot. It should be noted however, that the subject machine in the experiment was a SPMSM, with the d-axis current reference current set to zero.

Intelligent controllers developed towards PMSM motor applications may also be applied with minimal modification to induction type ac machines, due to the inherent machine similarities. The notable difficulty with fuzzy logic type intelligent control is that detailed system performance knowledge is required; or in the case of neural network or neuro-fuzzy controllers, training data is required. Tuning of the controller exists in the form of membership gains (fuzzy logic), to achieve proper scaling of feedback and control output. The tuning is thus a factor common to virtually all control techniques detailed herein, with the exception of adaptive gain schemes. The principal disadvantage of the types of intelligent controllers cited previously, is that in order to execute code which evaluates a series of conditional statements, more clock cycles are required than that of mathematical expression evaluation (in the context of IPMSM control). The direct effect of this is that the number of execution steps required for fuzzy algorithms results in a reduced sampling frequency (2kHz compared to the NL controller presented in this thesis at 10kHz), which limits the accuracy/precision of the controller. Thus, in order to implement a basic fuzzy logic controller faster computational resources are required to achieve comparable loop execution speeds to fixed gain or model based controllers

1.3 Objectives

The objective of this thesis is to develop, test and implement a robust nonlinear adaptive controller directed towards systems using any type of PMSM. Specific thesis objectives are presented below:

a. To design and test a nonlinear controller that will permit accurate and generic control of PMSM.

b. To enable wider speed range operation of a class of PMSM motors compared to existing[2] control techniques.

c. To demonstrate the performance of the IPMSM through multiple simulation environments.

d. To demonstrate through simulation and experiment, the robust nature of the adaptive aspect of the proposed controller.

e. To conduct real time implementation and acquire data to firmly establish an empirical basis for the performance of the proposed adaptive controller.

1.4 Typical PMSM Drive System

To provide an overview of typical PMSM drive system topologies, the diagram in Figure 1-2 illustrates the major system functional blocks. The system is comprised of distinct major components; being the inverter, synchronous machine and control system. The inverter used is a three phase two level, six switch inverter and enables the synthesis and application of time varying currents to the three phase motor. Naturally, in the context of this thesis, the synchronous machine analysed is an IMPSM, with time varying sinusoidal air-gap flux due to a rotor defined by buried permanent magnets (saliency), as per Figure 2-1. Finally, control command voltages, reference frame transformation, and other relevant control parameters are

---

[2] Control techniques using d-axis command current set at zero.

calculated. Translation of the command voltages into pulse width modulated signals is achieved through carrier based sine-triangle modulation technique. The methods used for each system component specific to this thesis, as well as comprehensive derivations are provided in the following sections.

In general the typical inverter topology for variable speed 3-phase drives does not change much, and thus the same configuration can be applied to any class of PMSM, induction machine or line start type of PMSM, which is a synthesis of PMSM and induction machine design.

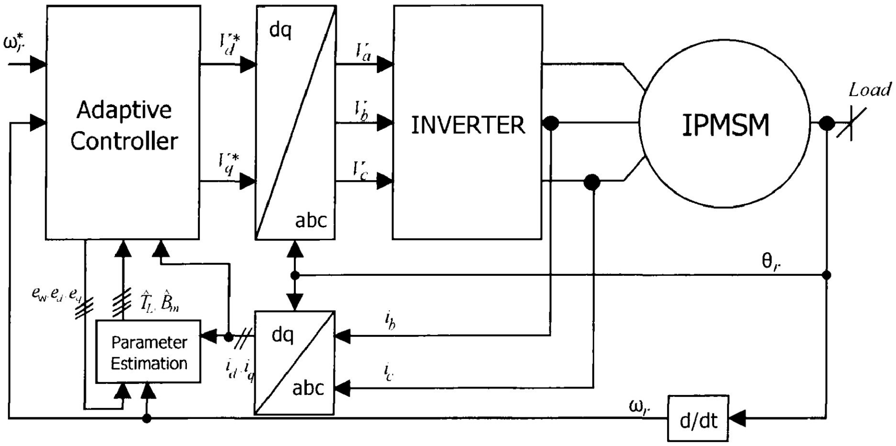

Figure 1-2: Typical 3-phase motor drive diagram

1.5 Thesis Organization

This thesis is arranged according to major section titles pertaining to the principle focus areas of the thesis. Subsections address specific detail, and contain pertinent figures, charts, or tables and/or appropriate references.

Chapter 1:

A review of literature of existing work on the control of PMSM is detailed, and a motivation for the following thesis work is provided. Figure 1-2 provides a comprehensive overview of the proposed motor drive system, including relevant switching devices and feedback devices.

Chapter 2:

Detailed derivations of all pertinent mathematical models used in the thesis, including reference frame conversion, and synchronous machine modelling are detailed herein.

Chapter 3:

This chapter details the development of the proposed adaptive nonlinear control algorithm for the IPMSM. Controller development is based on Lyapunov theory in conjuncture with adaptive back-stepping; global asymptotic stability is demonstrated using a trio of criterion supported by Barbalat's lemma.

Chapter 4:

Techniques are presented for extending the linear modulation range of naturally sampled pulse width modulation schemes. Supply transfer ratio, harmonic content and other common modulation techniques are also detailed in this chapter.

Chapter 5:

Results from multiple simulation environments are presented in this chapter. The performance of the proposed controller is established through a series of tests, including load variation, set-point changes and parametric variation.

Chapter 6:

In this chapter, the proposed controller is implemented using a real-time experimental set-up[3], with results demonstrating the robust performance through a series of tests similar to those performed in simulation.

Chapter 7:

This final chapter provides a summary of the thesis results and findings, the contributions made and future work potential in real time application and optimization.

---

[3] See Figure 6-2

Chapter 2

PMSM Mathematical Modeling

2.1 Introduction

This section of the thesis details development of the mathematical model of the PMSM. Model development begins with expressing stator reference equations reflecting the three phase configuration. Coordinate transformation permits the translation of complex nonlinear stator reference frame expressions into relatively simplified rotor reference frame expressions, thus simplifying model based control design.

To explain the choice of labelling that is to follow, it should be noted that the d-axis is chosen to align with the direction of magnetic flux (i.e. along north-south pole orientation), hence the label "direct" axis. As per an Institute of Electrical and Electronic Engineers (IEEE) convention, the q-axis is defined by a 90 electrical degree separation form the d-axis, and is thus labelled as "quadrature" axis [20]. These labels are used consistently across most relevant literature for variables written in the rotating rotor reference frame, and are illustrated in Figure 2-1 inspired in part from [21].

2.2 Coordinate Transformation

This thesis employs two variations of a reference frame conversion matrix, commonly called the "dq0" transform, these slight variants are known as the voltage and power invariant transforms. A proof of the latter transform is provided in this section, with detailed derivation steps provided for understanding the foundation of the transform. Use of either variant in implementation is permissible, given that the controller is designed correspondingly. A progressive illustration of the "dq0" coordinate transformation process is shown in Figure 2-2. Derivation is achieved in two steps; from stationary stator to stationary rotor and from stationary rotor to rotating rotor reference frames. The derivation details the "zero" axis component of the transforms, however, in Figure 2-2 & Figure 2-3 which visualize the transform, this component is omitted due to the assumption of balanced stator phase currents.

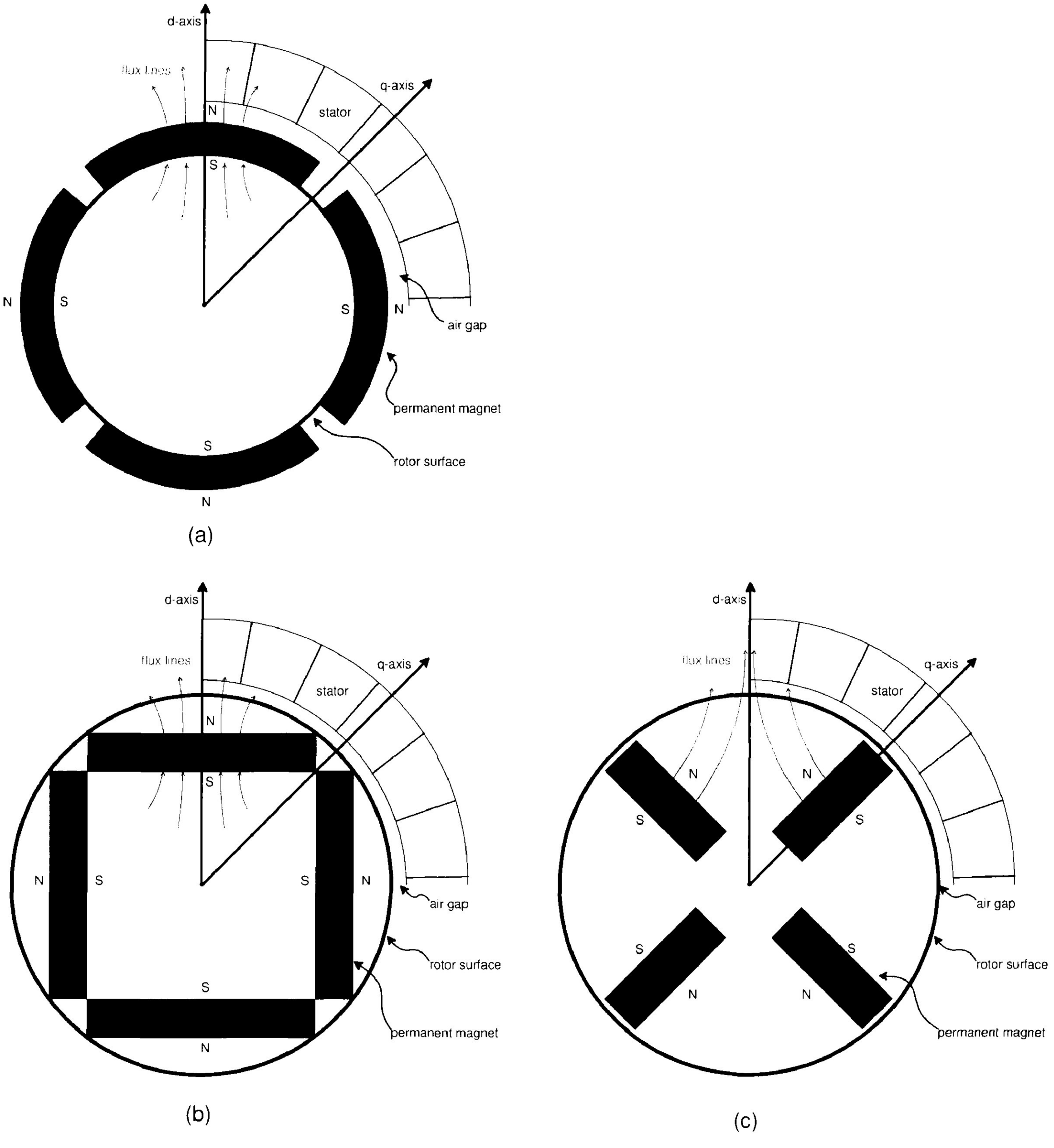

Figure 2-1: PMSM rotor cross section: a) surface mounted magnets b) interior radial magnets c) interior axial magnets

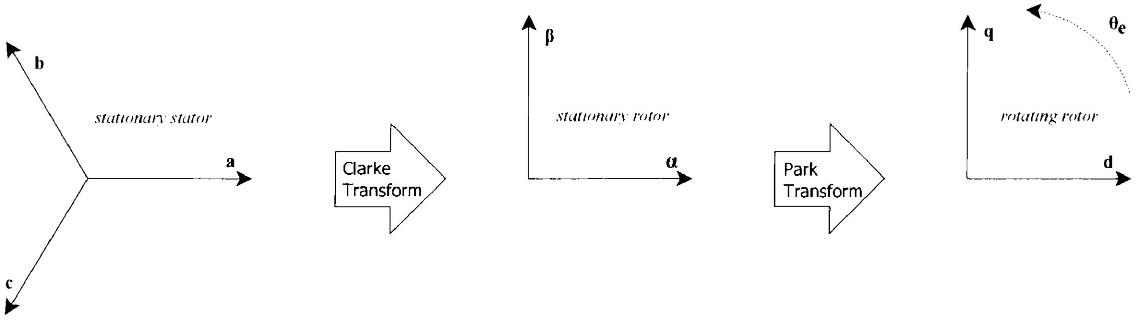

Figure 2-2: Forward reference frame conversion

The conversion matrix from stationary "abc" reference, to rotating (for a non-zero angular velocity) "dq0" can be found in a two-step procedure, first by converting to a fixed "$\alpha\beta 0$" reference frame, and then secondly from "$\alpha\beta 0$" to the rotating "dq0" reference frame [22], [23]. Please refer to Figure 2-3 for a graphical illustration as a guide during the derivation of the forward "dq0" transformation for balanced phases that follows.

To derive the transform matrix for stationary stator "abc" to stationary rotor transformation "$\alpha\beta 0$", the following vectors are defined as follows.

$$x_\alpha = k_1\left[x_a - x_b\cos(\tfrac{\pi}{3}) - x_c\cos(\tfrac{\pi}{3})\right] = k_1\left[x_a - \tfrac{1}{2}x_b - \tfrac{1}{2}x_c\right]$$

$$x_\beta = k_1\left[0x_a + x_b\cos(\tfrac{\pi}{6}) - x_c\cos(\tfrac{\pi}{6})\right] = k_1\left[0 + \tfrac{\sqrt{3}}{2}x_b - \tfrac{\sqrt{3}}{2}x_c\right]$$

$$x_0 = k_1 k_2\left[x_a + x_b + x_c\right]$$

where: k_1 = Proportionality constant that maintains power equivalency between the reference frames (to be determined)

k_2 = Additional proportionality constant for balancing the zero axis rotor current expression

$x_{()}$ = Relative vector magnitudes in each reference frame

The zero axis component (x_0) is defined as the sum of all stator vector quantities, which for balanced phases will be equal to zero. Thus it is not essential for this analysis, but is included to illustrative purposes only.

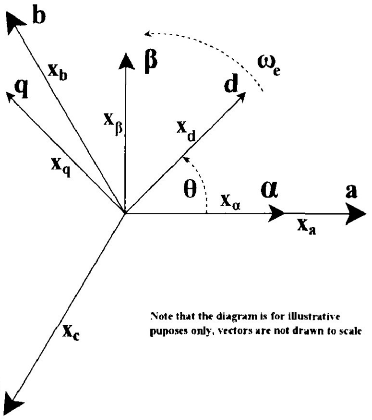

Note that the diagram is for illustrative puposes only, vectors are not drawn to scale

Figure 2-3: Reference frame vectors

Expressing the "$\alpha\beta 0$" quantities in a matrix form for convenience yields:

$$\begin{bmatrix} x_\alpha \\ x_\beta \\ x_0 \end{bmatrix} = k_1 \begin{bmatrix} 1 & -\frac{1}{2} & -\frac{1}{2} \\ 0 & \frac{\sqrt{3}}{2} & -\frac{\sqrt{3}}{2} \\ k_2 & k_2 & k_2 \end{bmatrix} \begin{bmatrix} x_a \\ x_b \\ x_c \end{bmatrix} = T_C x_{abc}$$

where the conversion matrix (Tc) is given by:

$$T_C = k_1 \begin{bmatrix} 1 & -\frac{1}{2} & -\frac{1}{2} \\ 0 & \frac{\sqrt{3}}{2} & -\frac{\sqrt{3}}{2} \\ k_2 & k_2 & k_2 \end{bmatrix}$$

In order to find the constants k_1 and k_2 a relationship for square matrixes is used that equates the multiplicity of a square matrix (T) and its inverse (T^{-1}) to the identity matrix (I). Expressed in matrix notation as $T_C \cdot T_C^{-1} = T_C^{-1} \cdot T_C = I$

$$k_1^2 \begin{bmatrix} 1 & 0 & k_2 \\ -\frac{1}{2} & \frac{\sqrt{3}}{2} & k_2 \\ -\frac{1}{2} & \frac{\sqrt{3}}{2} & k_2 \end{bmatrix} \begin{bmatrix} 1 & -\frac{1}{2} & -\frac{1}{2} \\ 0 & \frac{\sqrt{3}}{2} & -\frac{\sqrt{3}}{2} \\ k_2 & k_2 & k_2 \end{bmatrix} = \begin{bmatrix} 1 & 0 & 0 \\ 0 & 1 & 0 \\ 0 & 0 & 1 \end{bmatrix}$$

By extracting the following relationships from the matrix, using any two row-column combination:

$$k_1^2 + k_1^2 k_2^2 = 1$$

$$-\tfrac{1}{2} k_1^2 + k_1^2 k_2^2 = 0$$

Solving yields: $k_1 = \frac{\sqrt{2}}{\sqrt{3}}, k_2 = \frac{1}{\sqrt{2}}$

And thus the power invariant reference frame conversion matrix, known as the Clarke transform can be stated as:

$$T_C = \frac{\sqrt{2}}{\sqrt{3}} \begin{bmatrix} 1 & -\frac{1}{2} & -\frac{1}{2} \\ 0 & \frac{\sqrt{3}}{2} & -\frac{\sqrt{3}}{2} \\ \frac{1}{\sqrt{2}} & \frac{1}{\sqrt{2}} & \frac{1}{\sqrt{2}} \end{bmatrix}$$

To translate the stationary rotor ($\alpha\beta 0$) to the rotating rotor (dq0) reference frame, a coordinate mapping known as the Park transform is used. Further, with the assumption of balanced 3-phase currents, the zero axis component in the "dq0" reference frame will be zero. Thus, with reference to Figure 2-3, the following set of expressions may be defined in two dimensional Euclidean space.

$$x_d = x_\alpha \cos(-\theta) + x_\beta \cos(\theta - \tfrac{\pi}{2}) = x_\alpha \cos(\theta) + x_\beta \sin(\theta)$$

$$x_q = -x_\alpha \sin(\theta) - x_\beta \sin(\theta - \tfrac{\pi}{2}) = -x_\alpha \sin(\theta) + x_\beta \cos(\theta)$$

$$x_0^{rotating} = x_0^{stationary}$$

where: θ = angular position

Thus, from the equations above, the corresponding Park transform (T_P) matrix may be expressed as follows.

$$T_P = \begin{bmatrix} \cos(\theta) & \sin(\theta) & 0 \\ -\sin(\theta) & \cos(\theta) & 0 \\ 0 & 0 & 1 \end{bmatrix}$$

By combining both transforms (T_c & T_P) it is possible to achieve reference frame conversion directly from stator to rotor with a single conversion matrix (T_{dq0}).

$$\underbrace{T_{dq0} = \frac{\sqrt{2}}{\sqrt{3}} \begin{bmatrix} 1 & \frac{-1}{2} & \frac{-1}{2} \\ 0 & \frac{\sqrt{3}}{2} & \frac{-\sqrt{3}}{2} \\ \frac{1}{\sqrt{2}} & \frac{1}{\sqrt{2}} & \frac{1}{\sqrt{2}} \end{bmatrix} \begin{bmatrix} \cos(\theta) & \sin(\theta) & 0 \\ -\sin(\theta) & \cos(\theta) & 0 \\ 0 & 0 & 1 \end{bmatrix}}$$

$$\downarrow$$

$$T_{dq0} = \frac{\sqrt{2}}{\sqrt{3}} \begin{bmatrix} \cos(\theta) & -\frac{1}{2}\cos(\theta) + \frac{\sqrt{3}}{2}\sin(\theta) & -\frac{1}{2}\cos(\theta) - \frac{\sqrt{3}}{2}\sin(\theta) \\ -\sin(\theta) & \frac{1}{2}\sin(\theta) + \frac{\sqrt{3}}{2}\cos(\theta) & \frac{1}{2}\sin(\theta) - \frac{\sqrt{3}}{2}\cos(\theta) \\ \frac{1}{\sqrt{2}} & \frac{1}{\sqrt{2}} & \frac{1}{\sqrt{2}} \end{bmatrix}$$

Simplifying using the following trigonometric relationship[4]:

$$a\sin\theta \pm b\cos\theta = E\cos(\theta \mp \alpha)$$

This results in the final expression, which will be called the "dq0" transformation matrix.

$$T_{dq0} = \frac{\sqrt{2}}{\sqrt{3}} \begin{bmatrix} \cos(\theta) & \cos(\theta - \frac{2\pi}{3}) & \cos(\theta + \frac{2\pi}{3}) \\ -\sin(\theta) & -\sin(\theta - \frac{2\pi}{3}) & -\sin(\theta + \frac{2\pi}{3}) \\ \frac{1}{\sqrt{2}} & \frac{1}{\sqrt{2}} & \frac{1}{\sqrt{2}} \end{bmatrix} \tag{2.1}$$

In compact matrix notation, the transform may be applied as: $x_{dq0} = T_{dq0} x_{abc}$

where: x_{dq0} = Desired quantity in "dq" reference frame

x_{abc} = Quantity in stationary "abc" reference frame

To modify the "dq0" transform in (2.1) for a known initial position, the following relation between rotational angle and angular velocity is employed.

$$\theta = \theta_r = \int_0^t \omega(t)dt + \theta_0$$

where: ω = angular velocity

---

[4] This can also be shown for $E\sin(\theta \mp \alpha)$

Thus a slight variant of the dq0 transform for known initial angular position can be shown:

$$T_{dq} = \frac{\sqrt{2}}{\sqrt{3}} \begin{bmatrix} \cos(\omega t + \theta_0) & \cos(\omega t + \theta_0 - \frac{2\pi}{3}) & \cos(\omega t + \theta_0 + \frac{2\pi}{3}) \\ -\sin(\omega t + \theta_0) & -\sin(\omega t + \theta_0 - \frac{2\pi}{3}) & -\sin(\omega t + \theta_0 + \frac{2\pi}{3}) \\ \frac{1}{\sqrt{2}} & \frac{1}{\sqrt{2}} & \frac{1}{\sqrt{2}} \end{bmatrix}$$

This variant could be useful for position control scenarios and where the initial rotor position is known with a high degree of accuracy. Typically however, the initial position is not known, and the starting position is simply set as the zero reference, and the transform of the form seen in (2.1) is utilized. Conversely, the inverse transform (T_{dq0}^{-1}) is needed to translate variables from the rotating reference frame back to the stationary stator reference frame. The inverse of (2.1) may be expressed as follows:

$$T_{dq0}^{-1} = T_{abc} = \frac{\sqrt{2}}{\sqrt{3}} \begin{bmatrix} \cos(\theta) & -\sin(\theta) & \frac{1}{\sqrt{2}} \\ \cos(\theta - \frac{2\pi}{3}) & -\sin(\theta - \frac{2\pi}{3}) & \frac{1}{\sqrt{2}} \\ \cos(\theta + \frac{2\pi}{3}) & -\sin(\theta + \frac{2\pi}{3}) & \frac{1}{\sqrt{2}} \end{bmatrix} \qquad (2.1a)$$

where: T_{dq0}^{-1} = inverse “dq0” transform

However, depending on the application either the power or amplitude invariant versions of the transform may be employed. Since the power invariant version has been derived in detail, the amplitude invariant version will be directly expressed in (2.1b) & (2.1c), with the knowledge that derivation is of similar form.

$$T_{dq0} = \frac{2}{3} \begin{bmatrix} \cos(\theta) & \cos(\theta - \frac{2\pi}{3}) & \cos(\theta + \frac{2\pi}{3}) \\ -\sin(\theta) & -\sin(\theta - \frac{2\pi}{3}) & -\sin(\theta + \frac{2\pi}{3}) \\ \frac{1}{2} & \frac{1}{2} & \frac{1}{2} \end{bmatrix} \qquad (2.1b)$$

$$T_{dq0}^{-1} = T_{abc} = \begin{bmatrix} \cos(\theta) & -\sin(\theta) & 1 \\ \cos(\theta - \frac{2\pi}{3}) & -\sin(\theta - \frac{2\pi}{3}) & 1 \\ \cos(\theta + \frac{2\pi}{3}) & -\sin(\theta + \frac{2\pi}{3}) & 1 \end{bmatrix} \tag{2.1c}$$

Typically, the amplitude invariant form is utilized, potentially due to slightly lower computational complexity due to the absence of root terms. Further, with the assumption of balanced phase currents, it is possible to eliminate the third rows and columns of (2.1b) & (2.1c), as the zero axis component is zero. This greatly reduces the necessary computations required in each cycle of the control algorithm.

2.3 Synchronous Machine Modelling

In order to proceed with any nonlinear control design, an appropriate mathematical model is required. Based on the reference frame conversion derived in the previous section, and beginning with a stationary stator model not including core hysteresis and eddy current losses, a rotating "dq" reference frame model may be realized. With the "dq" mathematical model representing the machine variables in a rotating reference frame, a model of sufficient simplicity is achieved, where time varying periodic variables become virtual constants[5].

2.3.1 Machine Model Development

The control model is derived from first principles based on motor convention, where phase current flow is regarded as flowing into the terminals (conventional current flow model). An accurate mathematical model is key for successful implementation of a model based nonlinear controller. Model development is made based on the following assumptions:

1) Balanced stator phase resistance and by extension the phase currents
2) The effects of hysteresis and eddy currents are disregarded

---

[5] As a function of rotor position

Thus, for any Wye or Delta connected machine in a motor configuration, a three phase mathematical model using Kirchhoff's voltage law may be developed as follows.

$$\begin{bmatrix} v_a \\ v_b \\ v_c \end{bmatrix} = R_s \begin{bmatrix} i_a \\ i_b \\ i_c \end{bmatrix} + \frac{d}{dt} \begin{bmatrix} \phi_a \\ \phi_b \\ \phi_c \end{bmatrix} \tag{2.2}$$

where: v_a, v_b, v_c = stator phase voltages

R_s = stator phase resistance

i_a, i_b, i_c = stator phase current

ϕ_a, ϕ_b, ϕ_c = per-phase magnetic flux

The per-phase magnetic flux in the stator reference frame and is defined as follows with the last term contributed by the rotor permanent magnets.

$$\begin{bmatrix} \phi_a \\ \phi_b \\ \phi_c \end{bmatrix} = \begin{bmatrix} L_{aa} & L_{ab} & L_{ac} \\ L_{ab} & L_{bb} & L_{bc} \\ L_{ac} & L_{bc} & L_{cc} \end{bmatrix} \begin{bmatrix} i_a \\ i_b \\ i_c \end{bmatrix} + \begin{bmatrix} \phi_{ma} \\ \phi_{mb} \\ \phi_{mc} \end{bmatrix} \tag{2.3}$$

where: L_{aa}, L_{bb}, L_{cc} = per phase self-inductance

L_{ab}, L_{ac}, L_{bc} = per phase mutual-inductance

$\phi_{ma}, \phi_{mb}, \phi_{mc}$ = per phase flux due to permanent magnets

The rotor magnet flux contribution comprising the last matrix term in (2.3) is defined as:

$$\begin{bmatrix} \phi_{ma} \\ \phi_{mb} \\ \phi_{mc} \end{bmatrix} = \phi_m \begin{bmatrix} \cos(\theta - 0) \\ \cos(\theta - \frac{2\pi}{3}) \\ \cos(\theta + \frac{2\pi}{3}) \end{bmatrix} \tag{2.4}$$

where: ϕ_m = rotor induced magnetic flux in stator due to permanent magnets

Thus, the net synchronous motor mathematical model in the "abc" reference frame can be re-written as:

$$\begin{bmatrix} v_a \\ v_b \\ v_c \end{bmatrix} = R_s \begin{bmatrix} i_a \\ i_b \\ i_c \end{bmatrix} + \frac{d}{dt}\left\{ \begin{bmatrix} L_{aa} & L_{ab} & L_{ac} \\ L_{ab} & L_{bb} & L_{bc} \\ L_{ac} & L_{bc} & L_{cc} \end{bmatrix} \begin{bmatrix} i_a \\ i_b \\ i_c \end{bmatrix} + \phi_m \begin{bmatrix} \cos\theta \\ \cos(\theta + \frac{2\pi}{3}) \\ \cos(\theta - \frac{2\pi}{3}) \end{bmatrix} \right\} \qquad (2.5)$$

Due to sinusoidal flux distribution, model based control design from a stationary stator reference frame would be extremely difficult and computationally infeasible. Thus it is necessary to apply reference frame conversion to achieve a simplified model, this machine model representation must be transformed into the "dq" rotating reference frame.

2.3.2 Transformation Application

In the previous section, a synchronous machine model in the stator reference frame was developed. Using the reference frame transform in (2.1), the model of (2.2) may be expressed in the rotating rotor reference frame. The version of the "dq0" transform applied here is the power invariant transform (2.1), and is chosen principally for its orthogonality. This property translates as equivalency between the transforms transpose ($T_{dq0}^{'}$) and inverse (T_{dq0}^{-1}), and is further expressed in compact matrix notation below.

$$T_{dq0}^{'} = T_{dq0}^{-1}$$

where: $T_{dq0}^{'}$ = transpose of the "dq0" transform

An alternate expression of the above equivalency for the orthogonal transform matrix is shown for additional convenience.

$$T_{dq0} \cdot T_{dq0}^{-1} = T_{dq0} \cdot T_{dq0}^{'} = I$$

For convenience in the transformation process, the following equivalency is made and must be noted.

$$T_{dq0} = T$$

Note that the solution demonstrated is a symbolic solution, and the choice of transform type is arbitrary in the context of non-comparative system electrical equations. If comparison between quantities in differing reference frames is attempted, the type of transform becomes critical. Further, in the context of the system electromechanical equations, it is essential that the appropriate transform be utilized, as the developed electrical power term will differ depending on the transform used. Since the transform applies to voltages, currents, and flux linkages, it is easier to apply the transform to each component of the desired model in the "dq" reference frame and manipulate each term separately to achieve the transformed model. Due to the convenient properties of the power invariant transform seen in (2.1) & (2.1a), manipulation of the system matrices is less complex, and the transform process is simplified.

Expressing the vector quantities of (2.2) in a compact form as:

$$V_{abc} = R_s i_{abc} + \tfrac{d}{dt}\phi_{abc}$$

Applying the inverse transform equivalency to each "abc" matrix term of the model as:

$$X_{dq0} = T^{-1} X_{abc}$$

Results in the following expression:

$$(T^{-1} V_{dq0}) = R_s (T^{-1} i_{dq0}) + \tfrac{d}{dt}(T^{-1}\phi_{dq0})$$

Transforming both sides of the expression:

$$TT^{-1} V_{dq0} = TR_s T^{-1} i_{dq0} + T\tfrac{d}{dt}(T^{-1}\phi_{dq0})$$

Differentiation yields:

$$\begin{aligned} V_{dq0} &= TT^{-1}R_s i_{dq0} + T\left[\tfrac{d}{dt}(T^{-1})\phi_{dq0} + \tfrac{d}{dt}(\phi_{dq0})T^{-1}\right] \\ &= R_s i_{dq0} + T\left[\tfrac{d}{dt}(T^{-1})\phi_{dq0} + \tfrac{d}{dt}(\phi_{dq0})T^{-1}\right] \end{aligned}$$

Expanding and simplifying the factored components:

$$\begin{aligned} V_{dq0} &= R_s i_{dq0} + T\tfrac{d}{dt}(T^{-1})\phi_{dq0} + TT^{-1}\tfrac{d}{dt}(\phi_{dq0}) \\ &= R_s i_{dq0} + \underbrace{T\tfrac{d}{dt}(T^{-1})}_{\downarrow}\phi_{dq0} + \tfrac{d}{dt}(\phi_{dq0}) \end{aligned}$$

Continuing simplification of the above equation with the indicated segment "$T\frac{d}{dt}(T^{-1})$" as follows:

$$T\tfrac{d}{dt}(T^{-1}) = \underbrace{T\tfrac{d}{dt}\left(T^{'}\right)}_{\downarrow}$$

$$= \sqrt{\tfrac{2}{3}}\begin{bmatrix} \cos(\omega t+\theta_0) & \cos(\omega t+\theta_0-\frac{2\pi}{3}) & \cos(\omega t+\theta_0+\frac{2\pi}{3}) \\ -\sin(\omega t+\theta_0) & -\sin(\omega t+\theta_0-\frac{2\pi}{3}) & -\sin(\omega t+\theta_0+\frac{2\pi}{3}) \\ \frac{1}{\sqrt{2}} & \frac{1}{\sqrt{2}} & \frac{1}{\sqrt{2}} \end{bmatrix} * \frac{d}{dt}\sqrt{\tfrac{2}{3}}\begin{bmatrix} \cos(\omega t+\theta_0) & -\sin(\omega t+\theta_0) & \frac{1}{\sqrt{2}} \\ \cos(\omega t+\theta_0-\frac{2\pi}{3}) & -\sin(\omega t+\theta_0-\frac{2\pi}{3}) & \frac{1}{\sqrt{2}} \\ \cos(\omega t+\theta_0+\frac{2\pi}{3}) & -\sin(\omega t+\theta_0+\frac{2\pi}{3}) & \frac{1}{\sqrt{2}} \end{bmatrix}$$

$$= \tfrac{2}{3}\omega\begin{bmatrix} \cos(\omega t+\theta_0) & \cos(\omega t+\theta_0-\frac{2\pi}{3}) & \cos(\omega t+\theta_0+\frac{2\pi}{3}) \\ -\sin(\omega t+\theta_0) & -\sin(\omega t+\theta_0-\frac{2\pi}{3}) & -\sin(\omega t+\theta_0+\frac{2\pi}{3}) \\ \frac{1}{\sqrt{2}} & \frac{1}{\sqrt{2}} & \frac{1}{\sqrt{2}} \end{bmatrix}\begin{bmatrix} -\sin(\omega t+\theta_0) & -\cos(\omega t+\theta_0) & 0 \\ -\sin(\omega t+\theta_0-\frac{2\pi}{3}) & -\cos(\omega t+\theta_0-\frac{2\pi}{3}) & 0 \\ -\sin(\omega t+\theta_0+\frac{2\pi}{3}) & -\cos(\omega t+\theta_0+\frac{2\pi}{3}) & 0 \end{bmatrix}$$

In order to simplify the above expression, let:

$$A = (\omega t+\theta_0-\tfrac{2\pi}{3})$$

$$B = (\omega t+\theta_0+\tfrac{2\pi}{3})$$

$$\theta = (\omega t+\theta_0)$$

Permitting the re-expression of the previous as follows.

$$T\tfrac{d}{dt}\left(T^{'}\right)=\tfrac{2}{3}\omega\begin{bmatrix}\cos(\theta) & \cos(A) & \cos(B)\\ -\sin(\theta) & -\sin(A) & -\sin(B)\\ \tfrac{1}{\sqrt{2}} & \tfrac{1}{\sqrt{2}} & \tfrac{1}{\sqrt{2}}\end{bmatrix}\begin{bmatrix}-\sin(\theta) & -\cos(\theta) & 0\\ -\sin(A) & -\cos(A) & 0\\ -\sin(B) & -\cos(B) & 0\end{bmatrix}$$

Performing matrix multiplication provides the single matrix transform derivative expression.

$$T\tfrac{d}{dt}\left(T^{'}\right)=\tfrac{2}{3}\omega\begin{bmatrix}-(\sin\theta\cos\theta+\sin A\cos A+\sin B\cos B) & -(\cos^2\theta+\cos^2 A+\cos^2 B) & 0\\ (\sin^2\theta+\sin^2 A+\sin^2 B) & -(\sin\theta\cos\theta+\sin A\cos A+\sin B\cos B) & 0\\ -\tfrac{1}{\sqrt{2}}(\sin\theta+\sin A+\sin B) & -\tfrac{1}{\sqrt{2}}(\cos\theta+\cos A+\cos B) & 0\end{bmatrix}$$

Applying trigonometric identities defined in [23] and simplifying yields:

$$T\tfrac{d}{dt}\left(T^{'}\right)=\tfrac{2}{3}\omega\begin{bmatrix}0 & -\tfrac{3}{2} & 0\\ \tfrac{3}{2} & 0 & 0\\ 0 & 0 & 0\end{bmatrix}=\omega\begin{bmatrix}0 & -1 & 0\\ 1 & 0 & 0\\ 0 & 0 & 0\end{bmatrix}$$

Thus, a complete equation set in the d-q reference frame may be expressed, with all transform terms simplified.

$$\begin{bmatrix}v_d\\ v_q\\ v_0\end{bmatrix}=R_s\begin{bmatrix}i_d\\ i_q\\ i_0\end{bmatrix}+\begin{bmatrix}0 & -\omega_r & 0\\ \omega_r & 0 & 0\\ 0 & 0 & 0\end{bmatrix}\begin{bmatrix}\phi_d\\ \phi_q\\ \phi_0\end{bmatrix}+\tfrac{d}{dt}\begin{bmatrix}\phi_d\\ \phi_q\\ \phi_0\end{bmatrix}$$

Individually each of the transformed phases will be as follows:

$$v_d=R_s i_d-\omega\phi_q+\tfrac{d}{dt}\phi_d$$

$$v_q=R_s i_q+\omega\phi_d+\tfrac{d}{dt}\phi_q$$

$$v_0=R_s i_0+\tfrac{d}{dt}\phi_0$$

where: v_d, v_q = d-q axis voltages

i_d, i_q = d-q axis currents

ϕ_d, ϕ_q = d-q axis flux quantities

At this point, it is necessary to determine the expression for the d-q axis magnetic flux variables. To achieve this, the equation reflecting stator reference frame flux linkages (2.3) is revisited, and re-expressed in compact matrix form.

$$\underbrace{\begin{bmatrix} \phi_a \\ \phi_b \\ \phi_c \end{bmatrix} = \begin{bmatrix} L_{aa} & L_{ab} & L_{ac} \\ L_{ab} & L_{bb} & L_{bc} \\ L_{ac} & L_{bc} & L_{cc} \end{bmatrix} \begin{bmatrix} i_a \\ i_b \\ i_c \end{bmatrix} + \begin{bmatrix} \phi_{ma} \\ \phi_{mb} \\ \phi_{mc} \end{bmatrix}}$$

$$\downarrow$$

$$\phi_{abc} = L_s i_{abc} + \phi_m \begin{bmatrix} \cos\theta \\ \cos(\theta + \frac{2\pi}{3}) \\ \cos(\theta - \frac{2\pi}{3}) \end{bmatrix} = L_s i_{abc} + \phi_m C$$

where: ϕ_{abc} = flux linkage in the "abc" reference frame

L_s = stator reference frame inductance matrix

C = 120 degree phase shifted vector multiplier

Through strategic substitution, it is possible to reflect the stator variables to the rotor reference frame.

$$(T^{-1}\phi_{dq0}) = L_s(T^{-1}i_{dq0}) + \phi_m C$$

$$T(T^{-1}\phi_{dq0}) = TL_s(T^{-1}i_{dq0}) + \phi_m C$$

Simplifying yields:

$$\phi_{dq0} = \underbrace{(TL_sT^{-1})}_{\downarrow} i_{dq0} + \phi_m C$$

By simplifying $"TL_sT^{-1}"$ it is possible to express the flux quantities in the d-q reference frame as [24]:

$$\phi_d = L_d i_d + \phi_m \tag{2.6}$$

$$\phi_q = L_q i_q \tag{2.7}$$

where: L_d = d-axis inductance

L_q = q-axis inductance

For a balanced three-phase system[6], the zero axis component is zero, and thus the resultant "rotating" d-q reference frame expressions can be re-written as:

$$v_d = R_s i_d - n_p \omega_r \phi_q + \dot{\phi}_d \tag{2.8}$$

$$v_q = R_s i_q + n_p \omega_r \phi_d + \dot{\phi}_q \tag{2.9}$$

These results are as expected for the motor convention approach, and can be corroborated in mathematical principle by system equations in, [5], [6], [8], [9]. By applying the d-q axis flux quantities expressed in (2.6) & (2.7) to (2.8) & (2.9) it is possible to arrive at a suitable set of expressions.

$$v_d = R_s i_d - \omega L_q i_q + \tfrac{d}{dt} L_d i_d \tag{2.8a}$$

$$v_q = R_s i_q + \omega L_d i_d + \omega \phi_m + \tfrac{d}{dt} L_q i_q \tag{2.9a}$$

---

[6] Assumed, with validation shown for simulation and real-time

From (2.8a) & (2.9a), the generated counter electromotive force (EMF) may be expressed as follows.

$$E_d = -\omega L_q i_q + \tfrac{d}{dt} L_d i_d$$

$$E_q = \omega_r L_d i_d + \omega_r \phi_m + \tfrac{d}{dt} L_q i_q$$

$$E_m = \sqrt{E_d^2 + E_q^2}$$

where: E_d = d-axis generated EMF due to i_q

E_q = q-axis generated EMF due to rotor permanent magnet flux and i_d

E_m = peak phase generated EMF

In order to develop a machine mathematical model that can be readily used for nonlinear control design in a motor context, the model should be expressed in standard state space format.

$$\dot{i}_d = \tfrac{1}{L_d} v_d + \tfrac{n_p L_q}{L_d} \omega_r i_q - \tfrac{R_s}{L_d} i_d \tag{2.10}$$

$$\dot{i}_q = \tfrac{1}{L_q} v_q - \tfrac{n_p L_d}{L_q} \omega_r i_d - \tfrac{n_p \phi_m}{L_q} \omega_r - \tfrac{R_s}{L_q} i_q \tag{2.11}$$

To complete the state space model, the mechanical expression for the machine may be defined as:

$$\dot{\omega}_r = \tfrac{1}{J}\left(\tau_e - \tau_m - B_m \omega_r\right) \tag{2.12}$$

where: τ_e = developed electric torque

τ_m = motor shaft torque (output torque)

B_m = viscous coefficient of friction

J = motor inertia constant

It is necessary to express the developed electric torque expression, which can be expressed as follows:

$$\tau_e = \tfrac{3n_p}{2}\left[(L_d - L_q)i_d i_q + \phi_m i_q\right] \tag{2.13}$$

Then, by combining (2.12) and (2.13) a state equation that reflects known system parameters and variables may be shown as:

$$\dot{\omega}_r = \tfrac{1}{J}\left(\tau_e - \tau_m - B_m\omega_r\right) = \tfrac{1}{J}\left(\tfrac{3n_p}{2}\left[(L_d - L_q)i_d i_q + \phi_m i_q\right] - \tau_m - B_m\omega_r\right)$$

When re-expressed, the above velocity state equation becomes:

$$\dot{\omega}_r = \tfrac{3n_p(L_d - L_q)}{2J} i_d i_q + \tfrac{3n_p\phi_m}{2J} i_q - \tfrac{\tau_m}{J} - \tfrac{B_m}{J}\omega_r \tag{2.14}$$

For surface permanent magnet machines, the electric developed torque expression may be written as follows, with developed torque a direct linear function of i_q.

$$\tau_e = \tfrac{3n_p}{2}\phi_m i_q \tag{2.15}$$

Finally, the complete state space expression representing the machine may be expressed in a concise format as follows.

$$\text{System state equations:}\;\begin{cases} \dot{i}_d = \tfrac{1}{L_d}v_d + \tfrac{n_p L_q}{L_d}\omega_r i_q - \tfrac{R_s}{L_d} i_d \\ \dot{i}_q = \tfrac{1}{L_q}v_q - \tfrac{n_p L_d}{L_q}\omega_r i_d - \tfrac{n_p\phi_m}{L_q}\omega_r - \tfrac{R_s}{L_q} i_q \\ \dot{\omega}_r = \tfrac{3n_p(L_d - L_q)}{2J} i_d i_q + \tfrac{3n_p\phi_m}{2J} i_q - \tfrac{\tau_m}{J} - \tfrac{B_m}{J}\omega_r \end{cases}$$

The phase equivalent terminal voltages in the d-q reference frame may be used to visualize the rotor referred stator quantities in Figure 2-4. Note that the core loss equivalent resistance is omitted form the circuits, as the controller attempts to reduce losses indirectly through optimal torque current control and flux control methods.

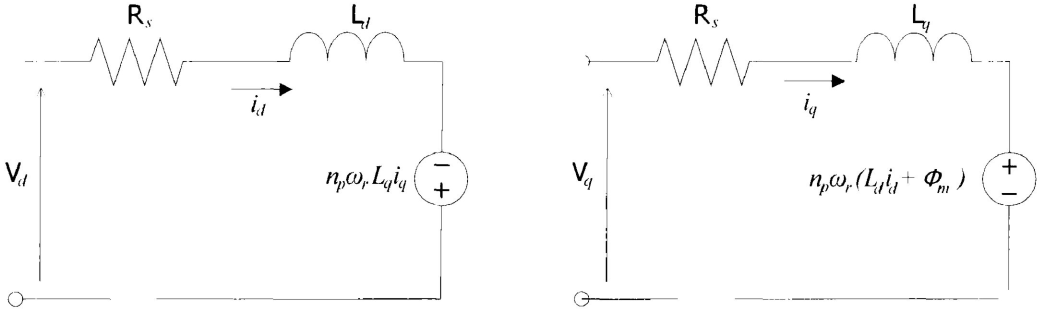

(a) (b)

Figure 2-4: Rotor referred stator equivalent circuit: a) d-axis b) q-axis

Further, the phasor diagram illustrating the current, voltage and magnetic flux vectors is shown in Figure 2-5, and provides a graphical illustration of some system equations from this section. This diagram will be of further relevance in the following Chapter 3, during development of the proposed controller. Notably, in the first quadrant of Figure 2-5, the air gap flux vectors Φ_{g1} and Φ_{g1} are shown to illustrate the relative resultant air gap flux magnitude when i_d is defined by a positive and negative trajectory respectively.

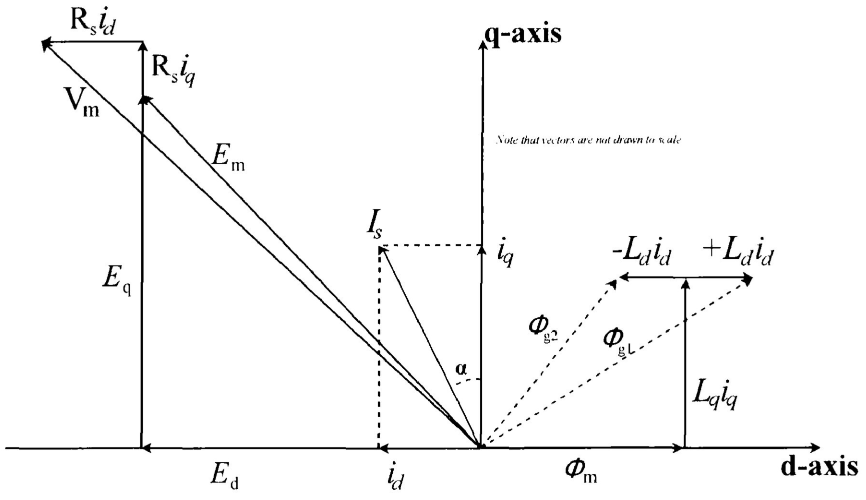

Figure 2-5: Phasor diagram

2.4 Conclusion

With the help of the detailed transformation theory, this section has developed a state space model for interior permanent magnet synchronous machines utilized as a motor. The developed model is translated to the rotating rotor reference frame for reduced computational complexity. It should also be noted that due to the computation of control variables in the rotating reference frame, translation back to the stator reference frame is required to apply the control. Further, as this thesis focuses on optimizing output torque and facilitating motor operation above rated speed, the core loss component of the machine model is disregarded. It should be noted that the method of control design presented in this thesis allows for the possibility of using any optimization algorithm for defining the d-axis current; and that a similar controller using some variation of core loss minimization algorithm could be developed in much the same manner. The following section details development of the proposed controller on the basis of the motor model established in this section.

Chapter 3

Proposed Motor Control Algorithm

3.1 Introduction

Accurate regulation of motor speed over a wide operational range is key to many applications, particularly electric vehicles, where operation may be required above the rated speed (constant power region). This thesis attempts to target the need for a wide operational range, by applying established flux control techniques in a comprehensive nonlinear controller with adaptive parameter estimation. Many existing control methods either ignore d-axis current and forfeit increased flux control, or utilize PI type controllers as a means of trajectory tracking. While simpler in implementation, performance may be limited, and operational range restricted.

To meet this control demand, the control algorithm proposed in this thesis incorporates maximum torque per ampere and flux weakening control to provide excellent performance, and an extended operational range. The diagram of the proposed control system is shown in Figure 3-1.

3.2 Control Techniques

Typical existing control methodologies have been rigorously detailed in the literature review section, and include linear, intelligent and model based control techniques. Among linear controllers, PI/PID type control is arguably most common. The PI controller may be used in a variety of contexts, anywhere error dynamics need to be forced to converge to some value (typically zero). The simplicity of PI controllers is a clear advantage and requires no special system knowledge with established tuning tools and techniques. Intelligent controllers may be designed to exhibit improved performance over PI controllers through the application of expert system knowledge [11]. Typically, however rule based intelligent controllers entail greater execution time due to conditional evaluations as opposed to mathematical operations for which there are typically dedicated hardware multipliers. As the model based control technique depends on the specific mathematical model of the system, it requires less computation than that of intelligent controllers. Additionally, a model based controller may be applied to an entire class of equivalent systems, with improved performance available given the system parameters. Model based control also enables the development of parameter estimation directly as part of controller design, which can help reduce reliance on system parameters.

Due to the prevalence of PI controllers, the comparison of the proposed controller will be made with respect to a PI controller employing flux control and hysteresis current controllers. By complementing the basic PI speed controller with d-axis command currents derived from the same MTPA and FW algorithms used in the proposed controller, it will be possible to achieve a direct performance comparison. Further comparison of the proposed controller will be made to the same type of nonlinear controller, however devoid of any indirect flux control methods. This comparison is key as well, due to the common practice of omitting flux control in many works [1], [15], [16], [25]. With the d-axis command current set to zero, the potential for reluctance torque (interior PM) and field weakening (surface & interior PM) is forfeit, ultimately limiting performance.

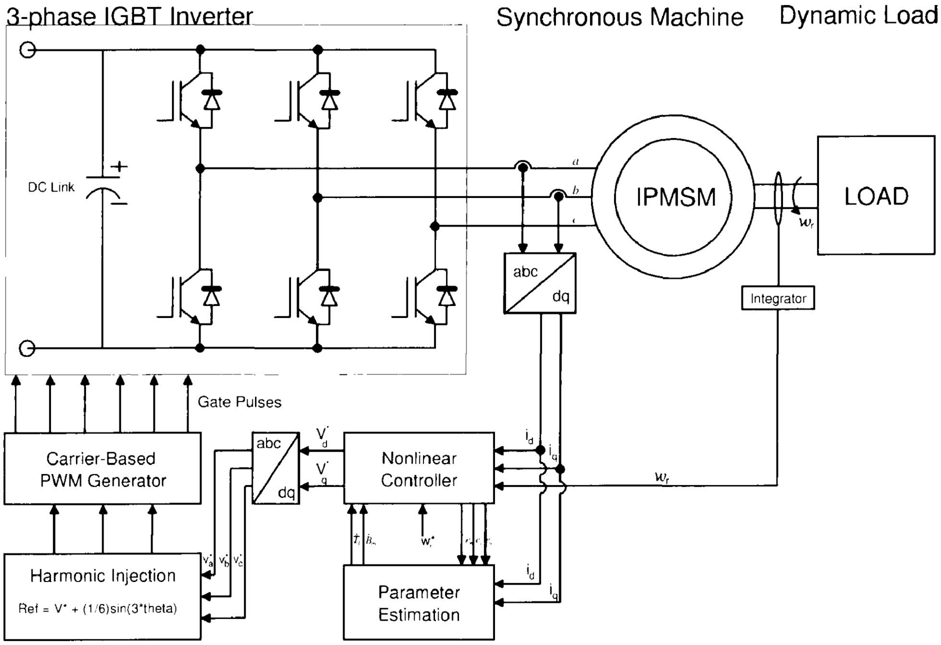

Figure 3-1: Proposed system overview

3.3 Command Current Derivations

For an IPMSM, the additional reluctance torque contributed by the d-axis current is a key advantage leading to increased operational range and efficiency. Many papers on IPMSM control disregard the d-axis current, including, [1], [2], [15], [16], [25], as it contributes to a more complicated control design. Thus, in order to achieve optimal motor control over a wide speed range, flux weakening control and maximum torque per ampere algorithms are incorporated into the control.

Flux control techniques function by using armature reaction to control the effective air gap flux and thus limit the induced counter-electromotive force to enable operation at higher speeds. Within the rated speed region, the flux control is achieved through MTPA, which seeks to define the d-axis current as a function of the q-axis current such that the rate of change of torque with respect to rotor angle approaches zero. In this region of operation, output torque is constant, as all quantities are within rated. The vector sum of the d-q axis currents are equivalent to the peak stator phase current, and may be expressed as follows:

$$i_d^2 + i_q^2 \le I_s^2 \tag{3.1}$$

In the flux weakening region above rated speed, the flux weakening d-axis current must be negative (commonly called demagnetizing) for motoring action, and the q-axis current should be limited as per (3.1a), such that neither voltage nor current ratings are exceeded. Ultimately this type of control will prevent the power rating from being exceeded, and thus avoiding damage to either the inverter or motor. Thus this region of operation may be commonly referred to as the constant power region, see Figure 3-2. As the output power of the motor in this region is constant, the developed shaft torque will be reduced proportionately with increasing angular speed, as per (3.2).

$$i_q^* = \sqrt{I_s^2 - (i_d^*)^2} \tag{3.1a}$$

$$P_{shaft} = \omega_r \tau_m \tag{3.2}$$

where: I_s = peak stator phase current

P_{shaft} = mechanical shaft power

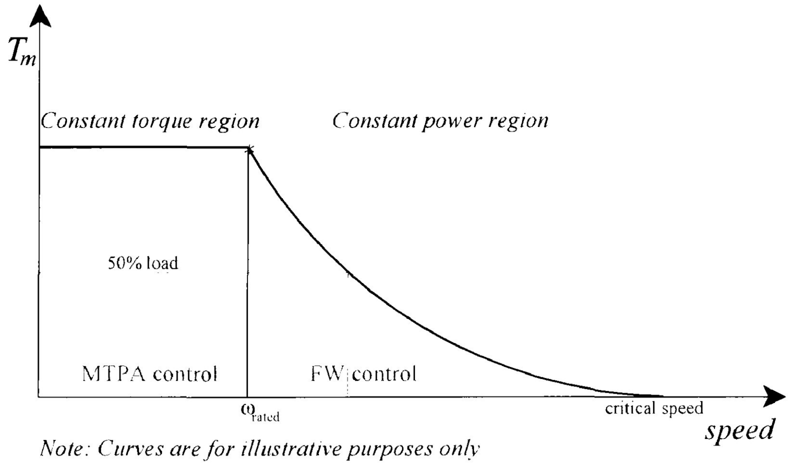

Figure 3-2: Motor torque-speed characteristics

It should be noted that, according to (2.6) & (2.12) respectively, a negative d-axis current will be responsible for not just increased reluctance torque, but also reduced/weakened d-axis flux. Conversely, if the d-axis current becomes positive (through use of FW control below rated speed), the effect will be that net shaft torque will be reduced, and the d-axis flux will be increased. Increased d-axis flux will have the effect that induced counter EMF will be greater as per (2.7a), which if near rated speed can result in voltage ratings being exceeded. Notably, this technique may be useful for situations that require higher speeds than would be possible with a fixed supply. Consequently, the FW algorithm would strengthen air-gap flux, increase speed and reduce the developed torque. In order to illustrate the operational regions of both MTPA and FW algorithms, Figure 3-3 is shown, conceptually inspired from [26] - [28].

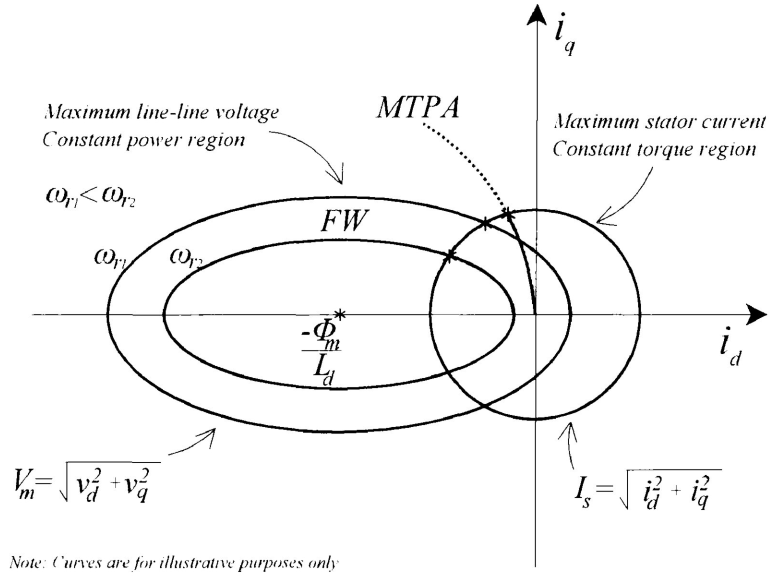

Note: Curves are for illustrative purposes only

Figure 3-3: Algorithm operational regions

The range of the MTPA algorithm trajectory is limited by the circle region of radius "I_s", which is the peak phase current, being equivalent to the vector sum of d and q-axis currents. By using the MTPA algorithm, an additional effect is the reduction of stator copper losses through optimization of i_d and thus the effective peak phase current.

In the FW region, the reference d-axis current is chosen such that the phase voltage does not exceed peak rated motor phase voltage "V_m". This control objective also has the effect of reducing core losses, as the air-gap flux is actively being weakened and thus results in reduced eddy currents. Depending on the angular velocity, the ellipse bounding permissible operation will vary, according to parametric expressions in (3.4) & (3.5). The center of the ellipse may be easily determined and exists at the point indicated below.

$$FW\ ellipse\ center\ coordinates = \left\{\frac{-\phi_m}{L_d},\ 0\right\}$$

The voltage limit ellipses (as a function of angular velocity) are described by the following elliptical equation, or equivalently, the set of following parametric expressions.

$$\frac{\left(i_d + \frac{\phi_m}{L_d}\right)^2}{\left(\frac{V_m}{n_p L_d \omega_r}\right)^2} + \frac{\left(i_q\right)^2}{\left(\frac{V_m}{n_p L_q \omega_r}\right)^2} \le 1 \tag{3.3}$$

$$i_d = \frac{-\phi_m}{L_d} + \frac{V_m}{n_p L_d \omega_r} \cos \omega_r \, \mathrm{t} \tag{3.4}$$

$$i_q = \frac{V_m}{n_p L_q \omega_r} \sin \omega_r \, \mathrm{t} \tag{3.5}$$

where: n_p = number of rotor pole pairs

V_m = peak terminal (phase-neutral) voltage

As the angular velocity of the drive increases above rated, reference current is derived from the FW algorithm, with the d-axis reference current defined to maintain terminal voltage to within the proportionately shrinking ellipse. Correspondingly, the maximum value of the q-axis current is limited in order to prevent exceeding the rated phase current, according to the vector sum of magnitudes expression in (3.1a).

3.3.1 Maximum Torque per Ampere Algorithm

A MTPA algorithm may be derived based on the following premise: that maximum torque for a given current value will exist when the time rate of change of torque with respect to current is zero. By redefining the d-q axis currents as vectors in quadrature as in Figure 2-5:

$$i_d = I_s \sin \alpha \tag{3.6}$$

$$i_q = I_s \cos \alpha \tag{3.7}$$

Thus if the command current is written as a function of alpha, the maximal instantaneous torque may be achieved when the derivative of electrical induced torque "with respect to alpha" is zero, i.e. electric torque is written as an indirect function of the angle [29]:

$$\underbrace{\tau_e = f(i_d, i_q) = f(g(\alpha))}$$

$$\Downarrow$$

$$\frac{d\tau_e}{d\alpha} = 0$$

Thus, if (2.12) is redefined in terms of the polar phasor quantities (3.6) & (3.7):

$$\begin{aligned}\tau_e &= \tfrac{3n_p}{2}\left[\phi_m i_q + (L_d - L_q) i_d i_q\right] \\ &= \tfrac{3n_p}{2}\left[\phi_m I_s \cos\alpha + (L_d - L_q) I_s^2 \sin\alpha \cos\alpha\right]\end{aligned}$$

Of which the derivative is:

$$\tfrac{d\tau_e}{d\alpha} = \tfrac{3n_p}{2}\left[-\phi_m I_s \sin\alpha + (L_d - L_q) I_s^2 (\cos^2\alpha - \sin^2\alpha)\right] = 0$$

Now, if the derivative expression is written in terms of the original d-q axis currents then:

$$\tfrac{d\tau_e}{d\theta} = \tfrac{3n_p}{2}\left[-\phi_m i_d + (L_d - L_q)(i_q^2 - i_d^2)\right] = 0$$

Then, the second order expression in "i_d" may be defined as:

$$\begin{aligned}0 &= -\phi_m i_d + (L_d - L_q)(i_q^2 - i_d^2) \\ &= i_d^2 + \tfrac{\phi_m}{(L_d - L_q)} i_d - i_q^2\end{aligned}$$

Thus the solution for 'i_d' in terms of 'i_q' is shown in sequence below:

$$\underbrace{i_d^2 + \frac{\phi_m}{(L_d - L_q)} i_d = i_q^2}$$

$$\downarrow$$

$$\underbrace{\left\{ i_d + \frac{\phi_m}{2(L_d - L_q)} \right\}^2 = i_q^2 + \frac{\phi_m^2}{4(L_d - L_q)^2}}$$

$$\downarrow$$

$$i_d^* = -\frac{\phi_m}{2(L_d - L_q)} \pm \sqrt{i_q^2 + \frac{\phi_m^2}{4(L_d - L_q)^2}} \tag{3.8}$$

However, since the d-axis command current must be negative[7] within the rated speed range, in order to contribute to the net developed toque; and the q-axis inductance is always equal or greater than the d-axis, the net positive result may be discarded and the final solution may be expressed as:

$$i_d^* = a - \sqrt{a^2 + i_q^2} \tag{3.9}$$

where: $a = \frac{\phi_m}{2(L_q - L_d)}$

The result in (3.9) can be improved upon by applying the Taylor series expansion about $i_q = 0$.

$$i_d^* = \sum_{n=0}^{\infty} \frac{f^{(n)}(0)}{n!} (i_q - 0)^n$$

Thus the partially expanded series for n = 0,,,4 is illustrated below:

$$i_d^* = -\left\{ \frac{(L_q - L_d)}{\phi_m} \right\} i_q^2 + \left\{ \frac{(L_q - L_d)}{\phi_m} \right\}^3 i_q^4 - \dots$$

---

[7] Note that it is also possible to use FW within rated speed, which results in a positive d-axis current

Use of the Taylor series expansion allows for the computational complexity to be reduced; hence, to achieve this, the series is truncated after the first term. This approximation is possible due to the fact that cube of the inductance differential is negligible.

$$i_d^* = \frac{(L_d - L_q)}{\phi_m} i_q^2 \tag{3.10}$$

In order to evaluate the validity of the simplification performed above, a plot of (3.9) and (3.10) is shown in Figure 3-4 with nominal machine parameters as a function of the q-axis current.

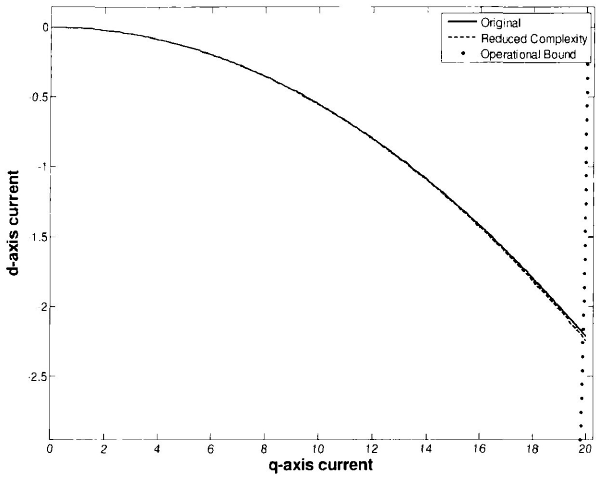

Figure 3-4: MTPA algorithm trajectory

As can be seen from the above plot, the approximated/truncated function using the Taylor series accurately follows the trajectory of the un-simplified function, only starting to slightly deviate for q-axis current above 15A. Note that the d-axis current limitation is shown with the circular trajectory specific to the Yaskawa 3.7kW IPMSM motor.

3.3.2 Flux Weakening Algorithm

For operational motoring speeds exceeding rated speed, the d-axis command current must be applied such that the effective air gap magnetic flux is controlled to limit the magnitude of the induced counter EMF. With the vector sum of d-q (quadrature) command voltages equal to or less than the maximum phase voltage, the basis for the flux control algorithm is established [26], [30].

$$v_q^2 + v_d^2 \leq V_m^2 \tag{3.11}$$

Note that the maximum line-to-line voltage may be expressed as per (3.12), for Wye connected machines.

$$V_m^{L\text{-}L} = \sqrt{3}V_m \tag{3.12}$$

where: V_m^{L-L} = peak line to line voltage

Further, it is assumed that at the operational point where the machine enters the FW region, the rate of change of quadrature currents is negligible. Applying this principle of steady state operation, the state equations may then be expressed without the derivative terms as:

$$v_d = -n_p L_q \omega_r i_q - R_s i_d \tag{3.13}$$

$$v_q = n_p L_d \omega_r i_d + n_p \phi_m \omega_r - R_s i_q \tag{3.14}$$

By further regarding the stator phase resistance as a negligible contributor at the speeds during which field weakening is used, (3.11) becomes:

$$(n_p L_d \omega_r i_d + n_p \phi_m \omega_r)^2 + (-n_p L_q \omega_r i_q)^2 \leq V_m^2 \tag{3.15}$$

Solving (3.15) by completion of squares:

$$\underbrace{\left[n^2{}_p L^2{}_d \omega^2{}_r\right] i^2{}_d + \left[2n^2{}_p \phi_m L_d \omega^2{}_r\right] i_d \leq -\left[n^2{}_p \phi^2{}_m \omega^2{}_r + n^2{}_p L^2{}_q \omega^2{}_r i_q{}^2 - V_m^2\right]}$$

$$\underbrace{i_d^2 + \left[\frac{2n^2{}_p\phi_m L_d \omega_r{}^2}{n^2{}_p L^2{}_d \omega^2{}_r}\right] i_d \leq -\left[\frac{n^2{}_p \phi^2{}_m \omega^2{}_r + n^2{}_p L^2{}_q \omega^2{}_r i_q{}^2 - V_m^2}{n^2{}_p L^2{}_d \omega^2{}_r}\right]}$$

$$\downarrow$$

$$\underbrace{\left\{i_d + \frac{\phi_m}{L_d}\right\}^2 - \left\{\frac{\phi_m}{L_d}\right\}^2 \leq \frac{V_m^2}{n_p^2 L_d^2 \omega_r^2} - \frac{\phi_m^2}{L_d^2} - \frac{L_q^2 i_q^2}{L_d^2}}$$

$$\downarrow$$

$$i_d^* \leq -\frac{\phi_m}{L_d} \pm \sqrt{\frac{V_m^2}{n_p^2 L_d^2 \omega_r^2} - \frac{L_q^2 i_q^2}{L_d^2}} \tag{3.16}$$

Since the result in (3.16) introduces a relative high degree of computational complexity, the Taylor series expansion is used as in the MTPA derivation, to achieve simplification. For additional convenience the FW expression is re-written as follows, with the inequality removed, such that the control will maintain a line-to-line voltage within the bounds of both the motor and inverter ratings. Additionally, the expression in (3.16) is characterized by two solutions, of which one results in excessive magnitude negative i_d values and is thus not an acceptable solution for field weakening control (or any control).

$$i_d^* = -\frac{\phi_m}{L_d} + \sqrt{\frac{V_m^2}{n_p^2 L_d^2 \omega_r^2} - \frac{L_q^2}{L_d^2} i_q^2} = b + \sqrt{c + d i_q^2} \tag{3.16a}$$

where: $b = -\frac{\phi_m}{L_d}$

$c = \frac{V_m^2}{n_p^2 L_d^2 \omega_r^2}$

$d = -\frac{L_q^2}{L_d^2}$

By expanding the Taylor series for the first four terms, a series sum may be expressed as:

$$i_d^* = b + c^{\frac{1}{2}} + \sum_{n=1}^{\infty} \frac{\mathrm{d}(-1)^{n+1}(3)^{n-1}(\mathrm{c})^{\frac{-2n+1}{2}} i_q^{2n}}{2\mathrm{n}!}$$

With the first three non-zero terms of the series:

$$i_d^* = \left\{ -\frac{\phi_m}{L_d} + \frac{V_m}{n_p L_d \omega_r} \right\} + \left\{ \frac{-n_p L_q^2 \omega_r}{2! V_m L_d} i_q^2 \right\} + \left\{ \frac{3 L_q^2 n_p^3 L_d \omega_r^3}{4! V_m^3} i_q^4 \right\} + \ldots$$

However, this is more complex than the original expression, thus, if the series is truncated appropriately, little error is introduced, and computational complexity is reduced. Following the second term in the expression, the numerical value of the numerator is of the 10^{-9} order, yielding a minimal contribution.

$$i_d^* = -\frac{1}{L_d} \left[\phi_m - \frac{V_m}{n_p \omega_r} + \frac{n_p L_q^2 \omega_r}{2 V_m} i_q^2 \right] \qquad (3.16b)$$

As can be seen from Figure 3-5, the truncated FW algorithm demonstrates minimal divergence from the exact expression in (3.16) up to the operating limit, while reducing the computational complexity significantly by eliminating the root and several second order operations. This figure is generated on the basis of maintaining rated phase voltage of the motor at speeds exceeding 183 rad/s. Notably, the load, rated motor voltage and operating speed all directly impact magnitude of i_d when using FW control as defined in (3.16b), and thus Figure 3-5 is illustrative of a specific speed operating point.

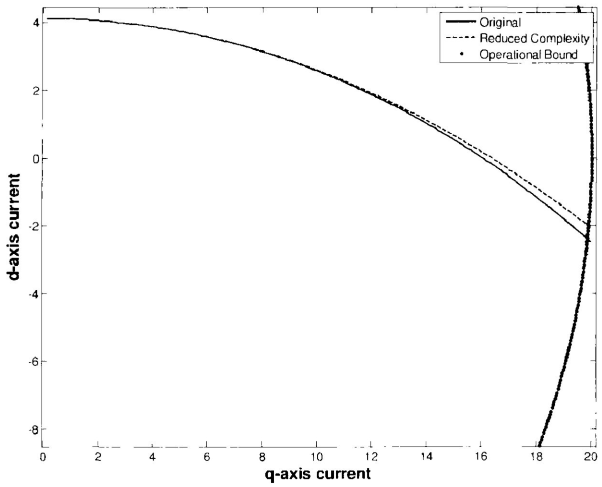

Figure 3-5: FW algorithm trajectory

Field weakening may also be employed below the rated speed, if required load is below rated. In this region of operation, the FW algorithm will generate a positive reference for i_d and will thus increase air-gap flux strength increasing angular speed, while marginally reducing the developed torque capacity. This situation may be useful when supply potential is limited, and additional speed operation is required at a reduced load.

3.4 Proposed Controller Design

Control design is based on Lyapunov theorem, with global stability ensured by criterion supported by Barbalat's theorem. Lyapunov theory can be phrased as follows [31]:

> *"... the origin is stable if there is a continuously differential positive definite function* $V(x)$ *so that* $\dot{V}(x)$ *is negative semi-definite, and it is asymptotically stable if* $\dot{V}(x)$ *is negative definite."*

The process of control design may be broken into the following major steps, starting with the defined reference variables and ending with the necessary adaptive parameter laws.

1) Definition of the reference variables, ω_r^*, i_d^*, i_q^*. The reference speed is defined by the operator, d-axis current reference defined in (3.23) and the q-axis current reference defined as in (3.21), such that the initial Lyapunov derivative is negative semi-definite.
2) Definition of a comprehensive Lyapunov function, including the estimated error terms (3.28), and the redefinition of pertinent relations in terms of estimated parameters.
3) Determination of the cancelling/stabilizing d-q axis command voltages, such that the Lyapunov derivative in (3.28) is comprised of only the error term pairs due to the estimated parameters.

4) Redefinition of the comprehensive Lyapunov function derivative in terms of only nominal parameters and insertion of the chosen d-q axis command voltages into that expression.

5) Grouping of all common error dynamic terms for each of the four estimated parameters.

6) Definition of update laws for each of the four estimated parameter groupings such that all grouped terms cancel and asymptotic stability of the Lyapunov derivative is ensured.

Starting with the basis of control, where the error between the optimal speed and the actual speed is forced to zero.

$$e_\omega = \omega_r^* - \omega_r \tag{3.17}$$

Differentiating and substituting state expression (2.14) yields:

$$\dot{e}_\omega = \dot{\omega}_r^* - \dot{\omega}_r = \dot{\omega}_r^* + \tfrac{1}{J}\tau_m - \tfrac{3n_p(L_d - L_q)}{2J} i_q i_d - \tfrac{3n_p\phi_m}{2J} i_q + \tfrac{B}{J}\omega_r \tag{3.18}$$

where: e_ω = speed error

$\dot{e}_\omega$ = rate of change of speed error (error dynamic)

ω_r^* = speed reference

Note that the reference speed derivative may be regarded as zero, except in instances of rapid change, and thus will be regarded as having an insignificant contribution to the error dynamic. Other derivative terms occurring and persisting during the control development are of significance, as these terms result in infinite discontinuities for instantaneous changes and thus preclude the use of step changes of reference values.

The Lyapunov stability criterion is modelled on the following candidate Lyapunov function as a starting point for controller design & stability analysis.

$$V = \tfrac{1}{2} e_\omega^2 \tag{3.19}$$

Differentiating and applying (3.19) yields:

$$\dot{V} = e_\omega \dot{e}_\omega = e_\omega \left[\dot{\omega}_r^* - \dot{\omega}_r \right] = e_\omega \left[\dot{\omega}_r^* + \tfrac{\tau_m}{J} + \tfrac{B_m}{J} \omega_r - \tfrac{3n_p(L_d - L_q)}{2J} i_d i_q - \tfrac{3n_p \phi_m}{2J} i_q \right] \tag{3.20}$$

Due to the high complexity of the nonlinear expression unless an approximation is made, the q-command current will be a function described by a 3rd order differential algebraic expression. Considering the inherent complexity of a third order expression, the number of possible solutions and the corresponding complexity of each solution renders that approach unfeasible. Thus, for the formation of the q-axis command current expression, the contribution of the reluctance torque is regarded as insignificant. Then, if the following expression is chosen for i_q, (3.20) becomes negative semi-definite.

$$i_q^* = \tfrac{2J}{3n_p \phi_m} \left[\dot{\omega}_r^* + \tfrac{\tau_m}{J} + \tfrac{B_m}{J} \omega_r + k_\omega e_\omega \right] \tag{3.21}$$

The stability criterion for the preliminary Lyapunov function is then validated, with the resultant Lyapunov derivative term negative semi-definite.

$$\dot{V} = -k_\omega e^2{}_\omega \tag{3.22}$$

Defining the d-axis current as a function of Maximum Torque per Ampere (MTPA) and Flux Weakening (FW) expressions.

$$\text{MTPA: } i_d^* = \tfrac{(L_d - L_q)}{\phi_m} i_q^2$$

$$\text{FW: } i_d^* = -\tfrac{1}{L_d} \left[\phi_m - \tfrac{V_m^{'}}{n_p \omega_r} + \tfrac{L_q^2 n_p \omega_r}{2V_m^{'}} i_q^2 \right]$$

For the purposes of control law derivation, the above MTPA and FW control algorithms are rolled into a single piecewise function in (3.23). In the final control laws, activation of either algorithm becomes trivial (manually or automatically), permitting seamless switching from MTPA to FW control and vice versa.

$$i_d^* = (1-n)\left[\frac{(L_d - L_q)}{\phi_m} i_q^2\right] - n\frac{1}{L_d}\left[\phi_m - \frac{V_m'}{n_p \omega_r} + \frac{L_q^2 n_p \omega_r}{2V_m'} i_q^2\right] \tag{3.23}$$

where: $n(\omega_r) = \begin{cases} 0, & \omega_r \le \omega_{rated} \\ 1, & \omega_r > \omega_{rated} \end{cases}$

Note that while the switching conditions above assume rated operation, the switching point may easily be made at a lower speed, convenient for achieving rated speeds with a supply voltage below rated.

With the speed error dynamics defined, and the d-q axis current reference expressions expressed, the current error terms may be expressed as follows.

$$e_d = i_d^* - i_d \tag{3.24}$$

$$e_q = i_q^* - i_q \tag{3.25}$$

Differentiating the d-q axis error terms gives the current error dynamics:

$$\dot{e}_d = \dot{i}_d^* - \dot{i}_d \tag{3.26}$$

$$\dot{e}_q = \dot{i}_q^* - \dot{i}_q \tag{3.27}$$

By differentiating the expressions in (3.24) and (3.25) and using the state equations (2.10) and (2.11), the error dynamics in (3.26) and (3.27) may be re-expressed in terms of known[8] quantities and variables.

The d-axis current error dynamic:

$$\dot{e}_d = \frac{2(1-n)(L_d-L_q)}{\varphi_m} i_q \dot{i}_q - \frac{n}{L_d}\left(\frac{V_m^{'}}{n_p \omega_r^2} + \frac{n_p L_q^2}{2V_m^{'}}(\dot{\omega}_r i_q^2 + 2\omega_r i_q \dot{i}_q)\right) - \frac{1}{L_d} v_d - \frac{n_p L_q}{L_d}\omega_r i_q + \frac{R_s}{L_d} i_d$$

The q-axis current error dynamic:

$$\underbrace{\dot{e}_q = \frac{2J}{3n_p\phi_m}\left[\ddot{\omega}_r^* + \frac{\dot{\tau}_m}{J} + \frac{B_m}{J}\dot{\omega}_r + k_\omega(\dot{\omega}_r^* - \dot{\omega}_r)\right] - \dot{i}_q}$$

$$\downarrow$$

$$\dot{e}_q = \frac{2J}{3n_p\phi_m}\left[\frac{\dot{\tau}_m}{J} + \frac{B_m}{J}\dot{\omega}_r + k_\omega\dot{\omega}_r^* + \left(\frac{B_m - k_\omega J}{J}\right)\left(\frac{3n_p(L_d-L_q)}{2J} i_d i_q + \frac{3n_p\phi_m}{2J} i_q - \frac{\tau_m}{J} - \frac{B_m}{J}\omega_r\right)\right]$$
$$- \frac{1}{L_q} v_q + \frac{n_p L_d}{L_q}\omega_r i_d + \frac{n_p \phi_m}{L_q}\omega_r + \frac{R_s}{L_q} i_q$$

By defining the following equivalencies, the speed error dynamic can be re-expressed as follows:

$\lambda = \frac{\tau_m}{J}$ = relative load torque

$\mu = \frac{B_m}{J}$ = relative mechanical frictional coefficient

Thus the speed error dynamic from (3.18) then becomes:

$$\dot{e}_\omega = \dot{\omega}_r^* + \lambda + \mu\omega_r - \frac{3n_p(L_d-L_q)}{2J} i_q i_d - \frac{3n_p\phi_m}{2J} i_q$$

---

[8] Note that some of these parameters are to be estimated

Due to parametric uncertainty and variation, estimation expressions for the following parameters are developed to enhance the robustness of the control. These estimated parameters represent virtual control variables, and effectively create error terms, which become stabilized by virtue of integration into the Lyapunov model function.

$\hat{L}_d$ = estimated d-axis inductance

$\hat{L}_q$ = estimated q-axis inductance

$\hat{\lambda}$ = estimated relative load torque

$\hat{\mu}$ = estimated relative mechanical frictional coefficient

The error terms may be defined as follows, notably, the initial load torque is an unknown quantity and is set to zero, with the adaptive algorithm providing convergence to a non-zero steady state value.

$$e_D = \hat{L}_d - L_d$$

$$e_Q = \hat{L}_q - L_q$$

$$e_\lambda = \hat{\lambda} - \lambda$$

$$e_\mu = \hat{\mu} - \mu$$

Differentiating the error terms yields the error dynamics, as follows:

$$\dot{e}_D = \dot{\hat{L}}_d$$

$$\dot{e}_Q = \dot{\hat{L}}_q$$

$$\dot{e}_\lambda = \dot{\hat{\lambda}} - \dot{\lambda}$$

$$\dot{e}_\mu = \dot{\hat{\mu}} - \dot{\mu}$$

With all the error terms and the corresponding error dynamics, it becomes possible to define a new and comprehensive stabilizing Lyapunov model function.

$$V_{system} = \tfrac{1}{2}(e_{\omega}^2 + e_d^2 + e_q^2 + \tfrac{1}{n_D} e_D^2 + \tfrac{1}{n_Q} e_Q^2 + \tfrac{1}{n_\lambda} e_\lambda^2 + \tfrac{1}{n_\beta} e_\beta^2) \tag{3.28}$$

The derivative of the comprehensive Lyapunov model function is as follows and includes the error and error dynamic term pairs previously defined.

$$\dot{V}_{system} = e_\omega \dot{e}_\omega + e_d \dot{e}_d + e_q \dot{e}_q + \tfrac{1}{n_D} e_D \dot{e}_D + \tfrac{1}{n_Q} e_Q \dot{e}_Q + \tfrac{1}{n_\lambda} e_\lambda \dot{e}_\lambda + \tfrac{1}{n_\mu} e_\beta \dot{e}_\beta \tag{3.29}$$

Because the d-q axis current reference expressions in (3.21) and (3.23) were defined based on nominal values, it is necessary to redefine these expressions as a function of the applicable estimated parameters.

$$i_q'^* = \tfrac{2J}{3n_p\phi_m}\left[\dot{\omega}_r^* + k_\omega e_\omega + \hat{\lambda} + \hat{\mu}\omega_r\right] \tag{3.30}$$

$$i_d'^* = \tfrac{(1-n)(\hat{L}_d - \hat{L}_q)}{\phi_m} i_q^2 - \tfrac{n}{\hat{L}_d}\left[\phi_m - \tfrac{V_m'}{n_p\omega_r} + \tfrac{\hat{L}_q^2 n_p \omega_r}{2V_m'} i_q^2\right] \tag{3.31}$$

Further, the speed error dynamic expression requires to be updated as a function of estimated parameters. Thus, the error terms for the d-q axis current are rearranged for direct substitution into the speed error dynamic expression of (3.18).

$$i_d = i_d'^* - e_d$$

$$i_q = i_q'^* - e_q$$

Defining the speed error dynamic in terms of estimated quantities:

$$\dot{e}_\omega = \dot{\omega}_r^* + \lambda + \mu\omega_r - \tfrac{3n_p\phi_m}{2J}\left(i_q'^* - e_q\right) - \tfrac{3n_p(L_d - L_q)}{2J}\left(i_d'^* - e_d\right) i_q$$

Substituting the expressions for estimated d-q axis command currents from (3.30) and (3.31) as follows:

$$\dot{e}_\omega = \left\{ \begin{array}{l} \dot{\omega}_r^* + \lambda + \mu\omega_r + \frac{3n_p\phi_m}{2J} e_q + \frac{3n_p(L_d - L_q)}{2J} e_d i_q \\ -\frac{3n_p\phi_m}{2J}\left(\frac{2J}{3n_p\phi_m}\left[\hat{\lambda} - \dot{\omega}_r^* - k_\omega e_\omega - \hat{\mu}\omega_r\right]\right) \\ -\frac{3n_p(L_d - L_q)}{2J}\left(\frac{(1-n)(\hat{L}_d - \hat{L}_q)}{\phi_m} i_q^2 - \frac{n}{\hat{L}_d}\left[\phi_m - \frac{V_m^{'}}{n_p\omega_r} + \frac{\hat{L}_q^2 n_p\omega_r}{2V_m^{'}} i_q^2\right]\right) i_q \end{array} \right\}$$

Simplifying the above speed error dynamic expression for easier manipulation later results in the following.

$$\dot{e}_\omega = \left\{ \begin{array}{l} \frac{3n_p\phi_m}{2J} e_q + \frac{3n_p(L_d - L_q)}{2J} e_d i_q - e_\lambda - e_\mu\omega_r - k_\omega e_\omega \\ -\frac{3n_p(L_d - L_q)}{2J}\left(\frac{(1-n)(\hat{L}_d - \hat{L}_q)}{\phi_m} i_q^2 - \frac{n}{\hat{L}_d}\left[\phi_m - \frac{V_m^{'}}{n_p\omega_r} + \frac{\hat{L}_q^2 n_p\omega_r}{2V_m^{'}} i_q^2\right]\right) i_q \end{array} \right\}$$

The d-q axis error dynamics may be re-expressed for greater clarity in the choice of command voltage expressions, i.e. that all terms are cancelled and the Lyapunov expression becomes equivalent to (3.34).

The d-axis current error dynamic is re-expressed as:

$$\dot{e}_d = \left\{ \begin{array}{l} \frac{2(1-n)(L_d - L_q)}{\phi_m} i_q \dot{i}_q - \frac{1}{L_d} v_d - \frac{n_p L_q}{L_d} \omega_r i_q + k_d e_d \\ + \frac{R_s}{L_d} i_d - \frac{n}{L_d}\left(\frac{V_m^{'}}{n_p\omega_r^2} + \frac{n_p L_q^2}{2V_m^{'}}(\dot{\omega}_r i_q^2 + 2\omega_r i_q \dot{i}_q)\right) \end{array} \right\}$$

The q-axis current error dynamic is re-expressed as:

$$\dot{e}_q = \left\{ \begin{array}{l} \frac{2J}{3n_p\phi_m}\left[\dot{\lambda} + \mu\dot{\omega}_r + k_\omega\dot{\omega}_r^* + \left(\frac{B_m - k_\omega J}{J}\right)\left(\frac{3n_p(L_d - L_q)}{2J} i_d i_q + \frac{3n_p\phi_m}{2J} i_q - \lambda - \mu\omega_r\right)\right] \\ -\frac{1}{L_q} v_q + \frac{n_p L_d}{L_q}\omega_r i_d + \frac{n_p\phi_m}{L_q}\omega_r + \frac{R_s}{L_q} i_q + k_q e_q \end{array} \right\}$$

The cancelling d-axis command voltage is then defined as:

$$v_d = \left\{ \begin{array}{l} R_s i_d + k_d e_d \hat{L}_d - n_p \omega_r \hat{L}_q i_q + \frac{2(1-n)(\hat{L}_d - \hat{L}_q)\hat{L}_d}{\phi_m} i_q \dot{i}_q \\ -n\left(\frac{V_m'}{n_p\omega_r^2} + \frac{n_p\hat{L}_q^2}{2V_m'}(\dot{\omega}_r i_q^2 + 2\omega_r i_q \dot{i}_q)\right) + \frac{3n_p(\hat{L}_d - \hat{L}_q)\hat{L}_d e_\omega i_q}{2J} \\ -\frac{3n_p(\hat{L}_d - \hat{L}_q)\hat{L}_d e_\omega i_q}{2Je_d}\left(\frac{(1-n)(\hat{L}_d - \hat{L}_q)i_q^2}{\phi_m} - \frac{n}{\hat{L}_d}\left[\phi_m - \frac{V_m'}{n_p\omega_r} + \frac{\hat{L}_q^2 n_p\omega_r}{2V_m'} i_q^2\right]\right) \end{array} \right\} \qquad (3.32)$$

The cancelling q-axis command voltage is defined as:

$$v_q = \left\{ \begin{array}{l} R_s i_q + k_q e_q \hat{L}_q + n_p\phi_m\omega_r + n_p\hat{L}_d\omega_r i_d + \frac{3n_p\phi_m\hat{L}_q e_\omega}{2J} \\ + \frac{2J\hat{L}_q}{3n_p\phi_m}\left[\dot{\hat{\lambda}} + \hat{\mu}\dot{\omega}_r + k_\omega\dot{\omega}_r^* + \left(\frac{B_m - k_\omega J}{J}\right)\left(\frac{3n_p(\hat{L}_d - \hat{L}_q)}{2J} i_d i_q + \frac{3n_p\phi_m}{2J} i_q - \hat{\lambda} - \hat{\mu}\omega_r\right)\right] \end{array} \right\} \qquad (3.33)$$

Thus the new Lyapunov derivative is:

$$\dot{V}_{system} = \left\{ -k_d e_d^2 - k_q e_q^2 \right\} + e_d\dot{e}_d + e_q\dot{e}_q + e_\omega\dot{e}_\omega + \frac{1}{n_D} e_D\dot{e}_D + \frac{1}{n_Q} e_Q\dot{e}_Q + \frac{1}{n_\lambda} e_\lambda\dot{e}_\lambda + \frac{1}{n_\mu} e_\mu\dot{e}_\mu \qquad (3.34)$$

Note that the bracketed terms at the front of (3.34) exist due to deliberate insertion of complementary error term pairs into the error dynamic expressions, so that the necessary gain terms appear in the command voltage expressions. The next section details the determination of adaptive laws that ensure a negative semi definite Lyapunov derivative, by redefining the nominal error dynamics (e_w, e_d, e_q) in terms of the command voltages using estimated parameters. The error terms for the estimated parameters are then extracted and grouped.

3.4.1 Parameter Adaptation

Having derived the command expressions for the d-q axis voltages involving MTPA and flux weakening algorithms, it is now possible to proceed with derivation of the parameter adaptation laws. Adaptive back-stepping technique is utilized to determine the parameter estimation expressions for the relative mechanical coefficient (μ), relative load (λ), d-axis inductance (L_d), q-axis inductance (L_q). The solution process begins with redefining the error dynamic expressions with the chosen command voltage expressions, which include the estimated parameters. The error dynamics are expressed in a manner that correlates to the Lyapunov derivative in (3.34).

$$e_\omega \dot{e}_\omega = e_\omega \left\{ \begin{array}{l} \frac{3n_p\phi_m e_q}{2J} + \frac{3n_p(L_d-L_q)e_d i_q}{2J} - e_\lambda - e_\mu \omega_r - k_\omega e_\omega \\ -\frac{3(1-n)n_p(L_d-L_q)(\hat{L}_d-\hat{L}_q)i_q^3}{2J\phi_m} + \frac{3nn_p(L_d-L_q)i_q}{2\hat{L}_d}\left[\phi_m - \frac{V_m^{'}}{n_p\omega_r} + \frac{\hat{L}_q^2 n_p\omega_r}{2V_m^{'}} i_q^2\right] \end{array} \right\} \tag{3.35}$$

$$e_d \dot{e}_d = e_d \left\{ \begin{array}{l} \frac{nn_p}{2\hat{L}_d V_m^{'}}(\dot{\omega}_r i_q^2 + 2\omega_r i_q \dot{i}_q)\left[e_Q^2 + 2L_q\hat{L}_q\right] \\ + \frac{n_p\omega_r i_q e_Q}{\hat{L}_d} - \frac{2(1-n)i_q\dot{i}_q e_Q}{\phi_m} - \frac{2(1-n)i_q\dot{i}_q e_D}{\phi_m} - \frac{3n_p(\hat{L}_d-\hat{L}_q)e_\omega i_q}{2J} \\ + \frac{3(1-n)n_p(\hat{L}_d-\hat{L}_q)(\hat{L}_d-\hat{L}_q)i_q^3 e_\omega}{2J\phi_m e_d} - \frac{3nn_p(\hat{L}_d-\hat{L}_q)e_\omega i_q}{2J\hat{L}_d e_d}\left[\phi_m - \frac{V_m^{'}}{n_p\omega_r} + \frac{\hat{L}_q^2 n_p\omega_r}{2V_m^{'}} i_q^2\right] \end{array} \right\} \tag{3.36}$$

$$e_q \dot{e}_q = e_q \left\{ \begin{array}{l} \frac{2J}{3n_p\phi_m}\left[-\dot{e}_\lambda + \dot{\omega}_r e_\mu + \left(\frac{B_m-k_\omega J}{J}\right)\left(e_\lambda - \frac{3n_p(e_D-e_Q)}{2J} i_d i_q + \omega_r e_\mu\right)\right] \\ -\frac{n_p\omega_r i_d e_D}{\hat{L}_q} - \frac{3n_p\phi_m e_\omega}{2J} \end{array} \right\} \tag{3.37}$$

Thus, having the simplified error dynamic expressions, the Lyapunov derivative in (3.34) may be re-expressed as a function of the expanded and simplified error dynamic terms, with the following result.

$$\dot{V}_{system}=\left\{\begin{array}{l} -k_\omega e_\omega^2-k_d e_d^2-k_q e_q^2 \\ +\left[\begin{array}{l} \frac{9(1-n)n_p(L_d-L_q)i_q^3 e_\omega}{2J\phi_m}-\frac{i_d i_q e_q}{\phi_m}\left(\frac{B_m-k_\omega J}{J}\right)-\frac{n_p\omega_r i_d e_q}{L_q}-\frac{3n_p i_q e_\omega e_d}{2J} \\ -\frac{3nn_p e_\omega i_q}{2JL_d}\left(\phi_m-\frac{V_m'}{n_p\omega_r}+\frac{L_q^2 n_p\omega_r i_q^2}{2V_m'}\right)-\frac{2(1-n)i_q\dot{i}_q e_d}{\phi_m}+\frac{1}{n_D}\dot{e}_D \end{array}\right]e_D \\ +\left[\begin{array}{l} \frac{n_p\omega_r i_q e_d}{L_d}-\frac{2(1-n)i_q\dot{i}_q e_d}{\phi_m}+\frac{3n_p i_q e_\omega e_d}{2J}-\frac{9(1-n)n_p(L_d-L_q)i_q^3 e_\omega}{2J\phi_m} \\ +\frac{3nn_p e_\omega i_q}{2JL_d}\left(\phi_m-\frac{V_m'}{n_p\omega_r}+\frac{L_q^2 n_p\omega_r i_q^2}{2V_m'}\right)+\frac{i_d i_q e_q}{\phi_m}\left(\frac{B_m-k_\omega J}{J}\right) \\ +\frac{nn_p(\dot{\omega}_r i_q^2+2\omega_r i_q\dot{i}_q)L_q e_d}{L_d V_m'}+\frac{1}{n_Q}\dot{e}_Q \end{array}\right]\mathrm{e}_Q \\ +\left[\frac{2\omega_r e_q(B_m-k_\omega J)}{3n_p\phi_m}-\omega_r e_\omega+\frac{1}{n_\mu}\dot{e}_\mu\right]e_\mu \\ +\left[\frac{2e_q(B_m-k_\omega J)}{3n_p\phi_m}-e_\omega+\frac{1}{n_\lambda}\dot{e}_\lambda\right]e_\lambda \end{array}\right\} \tag{3.38}$$

Based on the final expression for the Lyapunov derivative in (3.38), if the cancelling error terms "$\dot{e}_D,\dot{e}_Q,\dot{e}_\lambda,\dot{e}_\mu$" are chosen as follows, then the Lyapunov expression becomes negative semi-definite as in (3.43).

$$\dot{e}_D=-n_D\left[\begin{array}{l} \frac{3(1-n)n_p(L_d-L_q)i_q^3 e_\omega}{2J\phi_m}-\frac{3n_p i_q e_\omega e_d}{2J}-\frac{2(1-n)i_q\dot{i}_q e_d}{\phi_m}-\frac{n_p\omega_r i_d e_q}{L_q} \\ -\frac{3nn_p e_\omega i_q}{2JL_d}\left(\phi_m-\frac{V_m'}{n_p\omega_r}+\frac{L_q^2 n_p\omega_r i_q^2}{2V_m'}\right)-\frac{i_d i_q e_q}{\phi_m}\left(\frac{B_m-k_\omega J}{J}\right) \end{array}\right] \tag{3.39}$$

$$\dot{e}_Q=-n_Q\left[\begin{array}{l} \frac{3nn_p e_\omega i_q}{2JL_d}\left(\phi_m-\frac{V_m'}{n_p\omega_r}+\frac{L_q^2 n_p\omega_r i_q^2}{2V_m'}\right)-\frac{2(1-n)i_q\dot{i}_q e_d}{\phi_m} \\ +\frac{3n_p i_q e_\omega e_d}{2J}+\frac{n_p\omega_r i_q e_d}{L_d}-\frac{9(1-n)n_p(L_d-L_q)i_q^3 e_\omega}{2J\phi_m} \\ +\frac{nn_p(\dot{\omega}_r i_q^2+2\omega_r i_q\dot{i}_q)L_q e_d}{L_d V_m'}+\frac{i_d i_q e_q}{\phi_m}\left(\frac{B_m-k_\omega J}{J}\right) \end{array}\right] \tag{3.40}$$

$$\dot{e}_\lambda=n_\lambda\left[-\frac{2(B_m-k_\omega J)e_q}{3n_p\phi_m}+e_\omega\right] \tag{3.41}$$

$$\dot{e}_{\mu} = n_{\mu}\left[-\frac{2(B_m - k_{\omega}J)\omega_r e_q}{3n_p\phi_m} + \omega_r e_{\omega}\right] \tag{3.42}$$

Thus by applying the adaptive laws in (3.39) - (3.42), the Lyapunov derivative may be defined as negative semi definite.

$$\dot{V}_{system} = -k_{\omega}e_{\omega}^2 - k_d e_d^2 - k_q e_q^2 \leq 0 \tag{3.43}$$

In order to better clarify the implementation of the parameter adaptation laws, the expressions in (3.39) - (3.42) are integrated and expressed in the simplest form, as follows.

$$\hat{L}_d = -n_D\int\left[\begin{array}{l} \frac{3(1-n)n_p(L_d-L_q)i_q^3e_{\omega}}{2J\phi_m} - \frac{3n_pi_qe_{\omega}e_d}{2J} - \frac{2(1-n)i_q\dot{i}_qe_d}{\phi_m} - \frac{n_p\omega_ri_de_q}{L_q} \\ -\frac{3nn_pe_{\omega}i_q}{2JL_d}\left(\phi_m - \frac{V_m^{'}}{n_p\omega_r} + \frac{L_q^2n_p\omega_ri_q^2}{2V_m^{'}}\right) - \frac{i_di_qe_q}{\phi_m}\left(\frac{B_m-k_{\omega}J}{J}\right) \end{array}\right]dt \tag{3.44}$$

$$\hat{L}_q = -n_Q\int\left[\begin{array}{l} \frac{3nn_pe_{\omega}i_q}{2JL_d}\left(\phi_m - \frac{V_m^{'}}{n_p\omega_r} + \frac{L_q^2n_p\omega_ri_q^2}{2V_m^{'}}\right) - \frac{2(1-n)i_q\dot{i}_qe_d}{\phi_m} \\ +\frac{3n_pi_qe_{\omega}e_d}{2J} + \frac{n_p\omega_ri_qe_d}{L_d} - \frac{9(1-n)n_p(L_d-L_q)i_q^3e_{\omega}}{2J\phi_m} \\ +\frac{nn_p(\dot{\omega}_ri_q^2+2\omega_ri_q\dot{i}_q)L_qe_d}{L_dV_m^{'}} + \frac{i_di_qe_q}{\phi_m}\left(\frac{B_m-k_{\omega}J}{J}\right) \end{array}\right]dt \tag{3.45}$$

$$\hat{\tau}_L = -n_{\lambda}J\int\left[\frac{(B_m-k_{\omega}J)e_q}{n_p\phi_m} - e_{\omega}\right]dt \tag{3.46}$$

$$\hat{B}_m = -n_{\beta}J\int\left[\frac{(B_m-k_{\omega}J)\omega_re_q}{n_p\phi_m} - \omega_re_{\omega}\right]dt \tag{3.47}$$

3.4.2 Global Stability

In the previous section, the stability of the origin and state variables was demonstrated by ensuring that the Lyapunov derivative in (3.34) became negative semi-definite [31]. This conclusion is essential to showing state and system stability, however, it does not prove system global asymptotic stability. Thus, it is necessary to involve further stability analysis in conjuncture with the Lyapunov stability criterion. To proceed with further stability analysis, the classification of the system must be determined. Since the system is inherently time variant, classification falls under non-autonomous systems. A non-autonomous or time variant system is characterized by being an explicit (as well as implicit) function of time. Consequently, LaSalle invariance theory may not be applied to the system to determine asymptotic stability, as that stability theory only applies to autonomous (time invariant) systems.

Thus, in order to demonstrate system error convergence, and hence global asymptotic stability, a set of criterion based on Barbalat's lemma is employed. The premise of the lemma known as Barbalat's lemma is proved through contradiction and is as follows [31]:

"Let $\phi : R \rightarrow R$ *be a uniformly continuous function on* $[0,\infty)$. *Suppose that* $\lim_{t\rightarrow\infty} \int^{t} \phi(\tau)d\tau$
$\int \phi(\tau)d\tau$
exists and is finite. Then $\phi(t) \rightarrow 0$ *as* $t \rightarrow \infty$*"* [31]

The stability criterion supported by Barbalat's lemma can be summarized concisely by the following conditions [32].

I. V_{system} is characterized by a lower bound (✓)

II. $\dot{V}_{system}$ is negative semi definite (✓)

III. $\dot{V}_{system}$ is a uniformly continuous function of time (✓)

If the system shares the above characteristics, then it may be said to be globally asymptotically stable. Validating the proposed system for conformance to the above convergence conditions yields the following:

I. With $V_{system} = \frac{1}{2}\left[e_d^2 + e_q^2 + e_\omega^2 + \frac{1}{n_D} e_D^2 + \frac{1}{n_Q} e_Q^2 + \frac{1}{n_\lambda} e_\lambda^2 + \frac{1}{n_\mu} e_\mu^2 \right]$, it is evident from observation that $V_{system} \geq 0$

II. Since $\dot{V}_{system} = -k_\omega e^2{}_\omega - k_d e^2{}_d - k_q e^2{}_q \leq 0$, the expression guarantees negative semi-definite status.

IV. If $\dot{V}_{system}$ is indeed a uniformly continuous function of time, then $\ddot{V}_{system}$ will be found to be a bounded function (i.e. it does not diverge at any point in its domain). Thus, the second derivative of the Lyapunov function is found as:

$$\begin{aligned}
\ddot{V}_{system} &= -2k_\omega e_\omega \dot{e}_\omega - 2k_d e_d \dot{e}_d - 2k_q e_q \dot{e}_q \\
&= -2k_\omega e_\omega \left\{ \dot{\omega}_r^* - \tfrac{1}{J}\tau_m + \tfrac{3n_p(L_d - L_q)}{2J} i_q i_d + \tfrac{3n_p\phi_m}{2J} i_q + \tfrac{B}{J}\omega_r \right\} \\
&\quad - 2k_d e_d \left\{ \dot{i}_d^* - \tfrac{1}{\alpha L_d} v_d - \tfrac{n_p L_q}{L_d}\omega_r i_q - \tfrac{R_s}{\alpha L_d} i_d \right\} \\
&\quad - 2k_q e_q \left\{ \dot{i}_q^* - \tfrac{1}{\alpha L_q} v_q + \tfrac{n_p L_d}{L_q}\omega_r i_d + \tfrac{n_p\phi_m}{L_q}\omega_r - \tfrac{R_s}{\alpha L_q} i_q \right\}
\end{aligned}$$

Thus, with known bounded machine parameters ($n_p, \phi_m, J, V_m, \ldots$), design coefficients ($k_\omega$, k_d, k_q), command variables (i_d^*, i_q^*, ω_r^*), machine variables ($i_d, i_q, v_d, v_q, \omega_r$) and bounded error terms (e_ω, e_d, e_q); the time domain continuity of the Lyapunov derivative is ensured

With the three stability criterion validated, and thus having satisfied Barbalat's lemma, it can be concluded that:

$$\dot{V}_2 \to 0 \ as\ t \to \infty \text{ and } \left.\begin{matrix} e_\omega \\ e_d \\ e_q \end{matrix}\right\} \to 0 \ as\ t \to \infty$$

Accordingly, by extension it can be concluded that the Lyapunov derivative ($\dot{V}_{system}$) will approach zero as the three error terms approach zero, stated mathematically as follows.

$$\dot{V}_2 \to 0 \; as \left\{ \begin{matrix} e_\omega \\ e_d \\ e_q \end{matrix} \right\} \to 0$$

Thus, the system is found to be convergent over the entire domain, and demonstrates global asymptotic stability. Notably, in order for the stability analysis to remain valid, there may not be any instantaneous changes of any reference values. Instantaneous changes to reference values such as the speed set-point and load torque invalidate the basis of the stability theory, as derivatives of these parameters exist in the control design potentially causing infinite discontinuities. By ensuring that none of the key reference terms undergo instantaneous transitions, the stability theorem remains valid, and $\ddot{V}_{system}$ may be said to be bounded, and thus $\dot{V}_{system}$ is uniformly continuous over its entire domain.

3.5 Conclusion

Having necessarily determined the global stability of the proposed model based controller, it is essential to state the limitations of the system. Firstly, due to the reliance of the controller on machine parameters, it is essential for optimal performance that both design and adaptive coefficients are tuned appropriately. Secondly, due the presence of differential terms in the control expression, instantaneous change of the speed reference value must be avoided to prevent invalidation of the stability analysis. Realistically, instantaneous speed set-point changes are not used as they risk potentially damaging the motor (overcurrent transient) and connected machinery (mechanical stress). Consequently, the speed reference is applied as a step only for small changes, with a ramp change for large variations. Thus, infinite discontinuities are avoided and global stability of the system is preserved.

The following chapter details the principle techniques for the generation of pulse width modulated signals for the inverter.

Chapter 4

Modulation Techniques and Harmonic Analysis

4.1 Introduction

Regardless of the control method employed, command variables are either voltages or currents in the rotating rotor reference frame. In order for those control values to be translated to pulse width modulation (PWM) signals, it is necessary to detail some of the applicable techniques for providing switch gate commutation signals. In this thesis the inverter topology is two level 3-phase comprised of six insulated gate bipolar transistors (IGBT), each of the inverter legs (top and bottom switch for each phase) is gated with complementary PWM signals from the controller.

There are effectively three techniques commonly used in the context of 3-phase commutation (switch signal generation). Notably, some of the detailed techniques have slight variants utilizing the same general principle, and are not detailed in this this thesis. Only a brief overview of each major technique is provided, with further investigation left to the reader.

4.1.1 Hysteresis Current Control

Effective and simple, hysteresis current control is employed through direct comparison of the reference "abc" current waveforms with the actual phase currents. The benefit of this technique, is that direct current control may be applied with very little computation, and directly applied via hysteresis current control. Due to the nature of comparison between signals having the same envelope, full (100%) modulation results in pure rectangular generated gating signals. This result is comparable to natural sampling in the overmodulation region, and is generally responsible for the generation of increased harmonic distortion [33].

The following code snippet illustrates the simplicity of the hysteresis current control method, and the ease of implementation in a real time application using even basic 8-bit microcontroller (MCU).

```
volatile float ia=ib=ic= 0;              // initialize feedback current variables
volatile float ia_c=ib_c=ic_c=0;         // initialize command current variables
int high = 1;                            // define logic levels
int low = 0;

if (ia_c >= ia)
        PWM_a = high;
else
        PWM_a = low;
if (ib_c >= ib)
        PWM_b = high;
else
        PWM_b = low;
if (ic_c >= ic)
        PWM_c = high;
else
        PWM_c = low;
```

4.1.2 Space Vector Modulation

Space vector modulation functions on the basis of stationary rotor reference frame signals and rotor position, and thus requires a less mathematically intensive reference frame conversion. The alpha and beta signals activate the corresponding sector in the two dimensional Euclidean space, hence the title "space vector control" and thus activate the proper combination of switches for a given sector as illustrated in Figure 4-1. As a function of the way space vector PWM (SVPWM) functions, full utilization of the available supply potential is made, i.e. maximum transfer ratio [33]. Thus the maximum line to line potential possible with SVPWM is equivalent to the applied DC voltage, that is, the same as for natural sampling with triplen harmonic injection [33], [34]. This method is ideal for embedded systems, as the requisite function(s) may be expressed in look-up-tables (LUT), reducing computational burden and providing quick access.

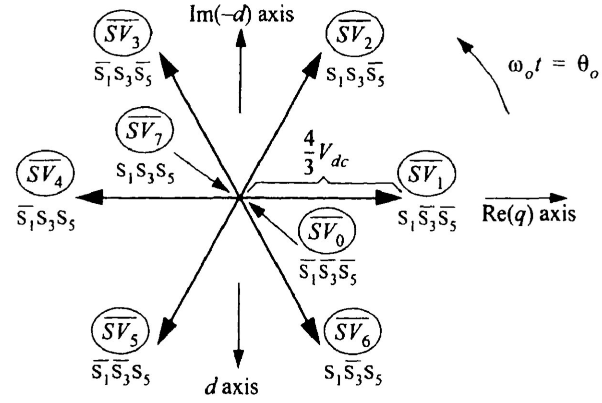

Figure 4-1: SVM illustration [33]

4.1.3 Naturally Sampled Modulation

Natural sampling may be employed when the reference trajectories are in the form of command d-q axis voltages, and hysteresis current control is not possible. A periodic carrier (triangular/sawtooth) signal is generated and compared to the reference signal, as in Figure 4-2. A pulse train of varying width is then generated as a result of the comparison. Either a triangular or sawtooth carrier may be used, however, the triangular carrier (known as double edged sampling) is more typically used, as it exhibits lower harmonic distortion due to the fact that it enables modulation of both sides of each phase leg pulse [33]. It should be noted that SVM and naturally sampled techniques with triplen injection achieve effectively the same result in terms of transfer ratio, with SVPWM providing flexibility with the positioning of the zero space vector, and thus enabling the potential for harmonic reduction [33], [34].

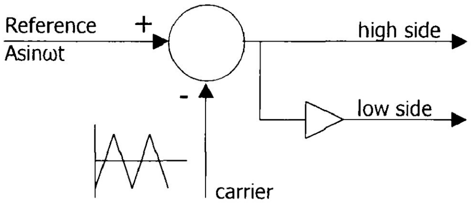

Figure 4-2: Double edged natural sampling

4.2 Harmonic Injection

For the real-time work performed for the proposed controller, the natural sampling technique was employed, due to relative ease of implementation and the fact that controller reference output exists in terms of d-q axis voltages. Further, since the controller provides reference values for v_d and v_q, it is not possible to directly utilize hysteresis current control, which requires references to be in terms of i_d and i_q. Direct synthesis of the PWM signals through mathematical definitions is also faster than using SVPWM on the master processor. To provide comparable or faster execution speeds, SVPWM would need to be implemented on the slave processor using a LUT.

In order to achieve optimal supply transfer ratio and minimize harmonic distortion for natural sampling, it is necessary to inject a third harmonic multiple into the reference sinusoids. Due to the 3-phase configuration, there is 120 degrees of separation between reference signals, this means that the third harmonic will exist in phase for each phase leg. Consequently, there is no net effect on line to line voltages[9]. The result is the reduction of peak phase reference voltages, permitting an increase in linear modulation index above that possible without triplen injection.

In scenarios where the inverter is driven from a front end uncontrolled rectifier fed by an alternating current (AC) source with peak voltage equal to that of the rated motor voltage, triplen injection is necessary for naturally sampled modulation. If triplen injection is not used, the controller will drive the system outside the linear modulation region, with the effect that control saturates during part of all of each PWM cycle[10] and harmonic content is increased. The implementation of triplen injection is relative simple, however, if extensive proof of the theoretical harmonic distortion reduction is required, refer to [33].

For natural sampling PWM techniques without any harmonic injection, the maximum linear modulation index is $m_a = 1$. Consequently, the maximum line-line potential achievable with natural sampling is defined in (4.1) as a function of the maximum linear amplitude modulation index [33].

---

[9] The net line-line potential differential of same phase signals is zero.

[10] Also known as square wave modulation

$$V_{L-L}^{\max} = \frac{\sqrt{3}}{2} m_a V_{DC} \simeq 0.866 V_{DC} \tag{4.1}$$

By injecting a third harmonic (triplen) of appropriate amplitude into the reference signals, it is possible to effectively "clip" the reference sinusoid peaks through constructive & destructive interference. The triplen (3N) signal is of the following form:

$$v_{3n} = \frac{1}{6}\sqrt{v_d^2 + v_q^2}\sin(3\theta) \tag{4.2}$$

Thus, with the triplen injected and the reference signal peak magnitude reduced, an increase in the linear modulation range of ~15.5% is realized [33], with the new amplitude modulation index designated with a "prime" notation, as follows.

$$m_a^{'} = \frac{2}{\sqrt{3}}$$

Thus, as a result the peak line-line voltage is now equal to the dc supply voltage.

$$V_{L-L}^{\max} = \tfrac{\sqrt{3}}{2} m_a^{'} V_{DC} = \tfrac{\sqrt{3}}{2}\left(\tfrac{2}{\sqrt{3}}\right) V_{DC} = V_{DC}$$

Theoretical harmonic content reduction of line-line voltage with one sixth magnitude third harmonic injection is approximately 0.27% (from 2.04 to 1.77%). The harmonic distortion value is the result of analysis normalized to the fundamental at a modulation index of unity and is reflective of harmonic content only due to switching strategy [33]. Further notable harmonic distortion may be contributed by other independent switching characteristics such as dead-time and also DC source noise level.

As previously stated, permitting the amplitude modulation index to surpass the linear region results in the loss of current control over part (overmodulation) or all (square-wave mode) of the modulating period. A potential effect of overmodulation is low frequency baseband harmonics which can have a significance negative effect on the developed torque (ripple). Figure 4-3 illustrates basic modulation scenarios respectively; linear modulation with m_a=0.9, over-modulation with m_a=1.08, and square wave mode operation with switches on during the entire active part of the switching cycle. For the proposed controller, the modulating signal is restricted from exceeding the linear modulation range by more than 30%, thus the modulating signal will never reach square wave mode. In the case of hysteresis current controllers, it is possible to reach square wave mode operation easily, as the comparison is between sinusoids[11] with directly comparable signal envelopes.

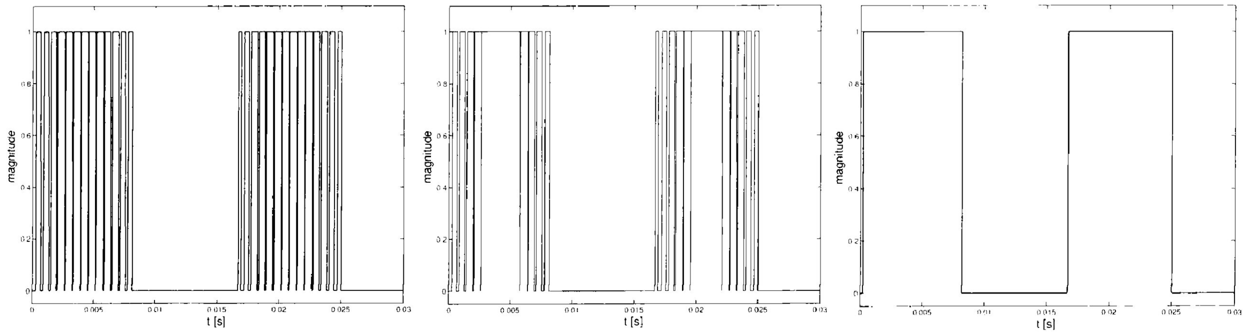

(a) (b) (c)

Figure 4-3: Modulated signal classes: a) linear b) overmodulation c) square-wave mode

4.3 Conclusion

This section has provided a brief overview of modulating techniques, and concludes the development of the proposed control system. At this point, the control and adaptive laws are established, stability is verified, the modulating technique is specified and harmonic injection is detailed. The next section details the development and testing of the proposed controller in simulation and lays the groundwork for real-time implementation.

---

[11] Sinusoid signal envelopes are directly comparable in magnitude over all points in a period

Chapter 5

System Simulation

5.1 Introduction

With the nonlinear controller derived and adaptive expressions formed in Chapter 3, the simulation of the proposed controller is performed in a simulation environment using both MATLAB/Simulink and PSIM.

Analysis of the proposed controller is performed for a diverse set of operating conditions to demonstrate the performance. Comparison is also made to typical PI controllers to further demonstrate the improvement in performance, operating speed range and robustness of the proposed nonlinear controller. Simulation of the proposed controller is performed with limitations accurately reflecting the real-time system, to attempt to emulate the actual system and provide consistent results. The proposed controller is tested in simulation for ramp and small step set-point changes over a wide speed range, with load disturbances applied during operation. The simulation tests are shown in the following sections, and are intended to reflect typical operational scenarios which include gradual starting with full load, or reduced start-up load which is gradually increased once the machine reaches steady state. Limited results will be shown for a step speed response, simply to illustrate the controller performance, as this operation can result in significant surge current. Simulation results shown are the function of all estimated parameters, including q axis inductance, load and mechanical coefficient. Tuning of the design coefficients may vary to achieve optimal performance for each respective simulation scenario, with this range of permissible values reflected in Table A-3. Comparative results are shown for a PI controller (hysteresis current & carrier based) using the same MTPA algorithm, to illustrate the differences in performance. To conclude the simulation results section, key results are illustrated for triplen harmonic injection with supply voltages fixed at typical values with frequency domain plots and THD[12] levels shown.

---

[12] Note that all simulation and experimental THD values are reflective of net system harmonic distortion.

5.2 Simulation Software

By designing a comprehensive system in MATLAB/Simulink using mathematical models of each stage (control, PWM generation, inverter, motor), it is possible to achieve a basic system model, which is capable of demonstrating the controller performance. Each stage of the system is expressed in Simulink as a function reflecting the mathematical model. The motor model has been developed and shown in (2.10)-(2.12), the PWM generation is expressed in visual block form based on if/else comparison statements and the inverter model expressed in basic form as a scaled summation of the three phase PWM signals over time.

In order to perform simulations on a software model more accurately representing a real system, PSIM was utilized to host the machine/motor model and 3-phase two level inverter, as seen in Appendix B. It should be noted that MATLAB/Simulink is also capable of modeling power electronics through the Simulink toolbox "SimPowerSystems", however, the configuration chosen permits simulation in the absence of any MATLAB/Simulink toolboxes.

5.3 Simulation Results

Simulation results are performed for a set of key environmental conditions, with results shown representing critical system dynamics. To illustrate the performance of the proposed controller, key system dynamics are shown for reference speed and loading variations for a 3.7kW IPMSM with parameters shown in Appendix A. Notably, major speed set-point and loading variations are achieved through ramp changes, this avoids any infinite discontinuities that might invalidate the stability analysis. Further, this is typical of reality, where reference values cannot undergo significant instantaneous variations, as surge current magnitudes can exceed ratings and excessive mechanical stress occurs. Secondly, the proposed controller is compared to traditional PI type controllers for key aspects including response time, overshoot/undershoot and current trajectories.

For phase current harmonic distortion analysis, PSIM hosts the machine model and triplen harmonics are injected through the controller run in MATLAB/Simulink. Results are shown for rated conditions, with comparison to the distortion levels seen without triplen[13] and to the same PI controller detailed previously.

5.3.1 Speed Reference Changes

This section demonstrates the performance of the proposed controller for a series of reference speed variations at a fixed load, including ramp and step command both increasing and decreasing the operational speed.

For the following results in Figure 5-1, the fixed load at which the motor operates is set at 50% rated load, such that rated power is not exceeded for the maximum reference speed. The reference speed is increased to 183 rad/s over a 500ms interval, ramped up to 300 rad/s from t=1.0s to t=1.5s and finally reduced to 100 rad/s from t=2.5s to t=3.0s. The corresponding speed response (left axis) of the system using the proposed speed controller is shown in Figure 5-1a, with the estimated load torque shown on the right axis. For clarity, the d-q axis currents are shown separately in Figure 5-1b, and demonstrate the additional flux control and reluctance torque possible with the proposed controller. The phase current is shown in Figure 5-1c to demonstrate that the maximum permissible phase current is never exceeded. Figure 5-1d shows the error dynamics through the speed step changes, due to the use of ramp speed changes, the speed error remains low and all error dynamics are observed to converge to near zero, despite the relative short duration of steady state of each reference speed.

---

[13] For the proposed controller

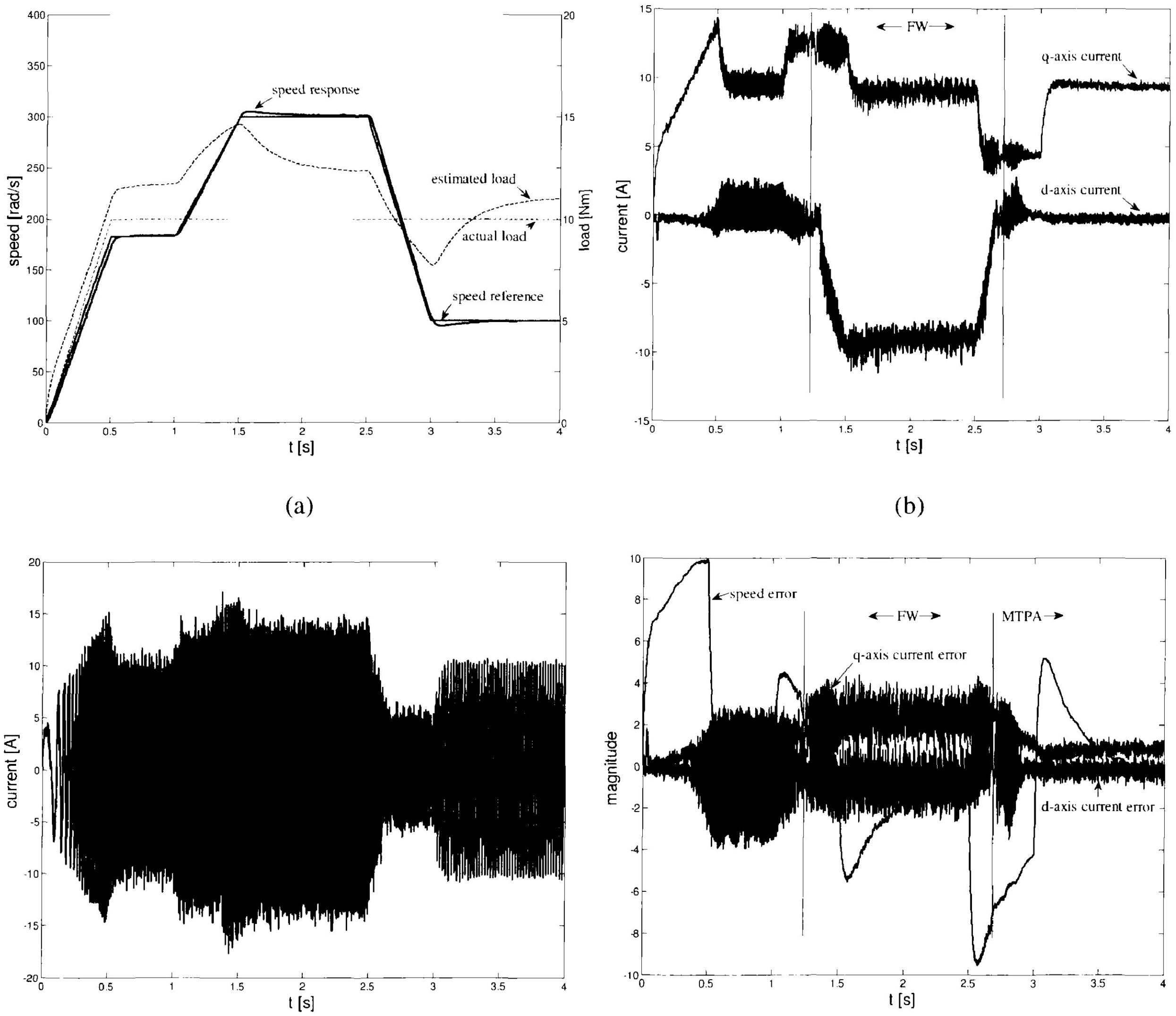

(a) (b)

(c) (d)

Figure 5-1: Speed Reference Change: a) Speed response b) d-q axis currents c) phase current d) error dynamics

Figure 5-2 shows the contribution of reluctance torque made possible through control of the d-axis current control. In field weakening mode of operation, above the rated speed, the d-axis current provides additional torque proportional to the saliency ratio of the subject motor. Additionally, the air gap flux is controlled and limited by the negative d-axis current, such that rated motor and inverter conditions are not exceeded.

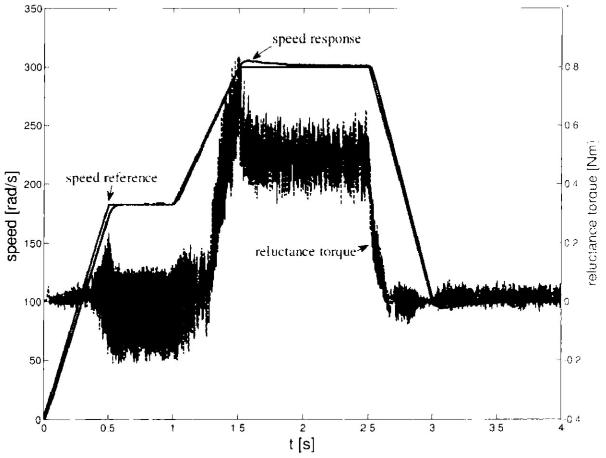

Figure 5-2: Reluctance torque

Thus far, reference speed has been applied only as a ramp, to avoid current transients and invalidation of the control stability theory. The following results are shown to demonstrate the step response of the proposed controller for relative small variations in the reference speed. Consequently, Figure 5-3 shows the proposed controller response for a step increment and decrement of 63 rad/s in the command speed. This is to establish the step response of the proposed controller, and compare to experimental results for a similar step change. Naturally, the current spike is significant, and in reality the response would be slower due to the limitation of the power supply. The controller exhibits an accurate response, despite having ramp and step changes applied over the lower speed range.

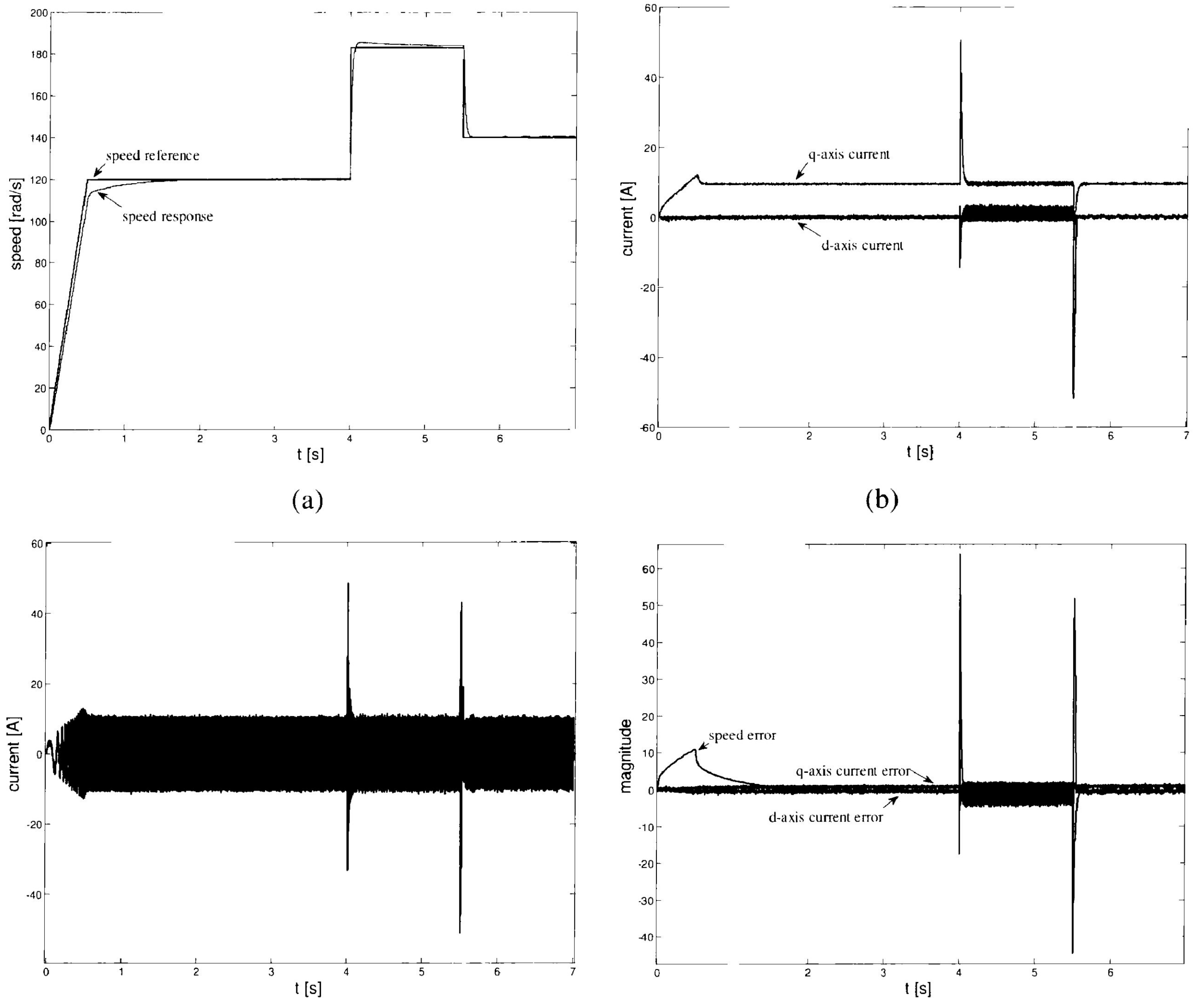

(a) (b)

(c) (d)

Figure 5-3: Step response: a) speed response b) i_d i_q c) i_a d) error dynamics

5.3.2 Applied Load Changes

This section demonstrates the performance of the proposed controller for a series of load variations. Load variation is applied in ramp changes to prevent instantaneous changes that could destabilize the controller. The same set of variables are plotted to provide consistency with the previous section on speed reference change.

With the reference speed set at rated (183.3 rad/s), the load is first changed from zero to 50% of rated from t=0s to t=0.5s. An increase in load to 100% of rated (3.7kW) is made from t=1s to t=1.5s, which brings the motor to rated operation. Finally, the load is reduced from 100% to

25% at t=2.5s. The speed response of the proposed controller for these load changes is shown in Figure 5-4a, with the estimated and actual load shown on the right axis of the figure. The controller is able to rapidly converge on the reference speed following each load disturbance, demonstrating excellent stability. The corresponding d-q axis currents are shown in Figure 5-4b, demonstrating the additional reluctance torque due to the negative d-axis current. Again, the phase current is shown in Figure 5-4c to demonstrate that the peak does not exceed the rated current at 100% load. The error dynamics are shown in Figure 5-4d, and demonstrate that in steady state the error terms converge to near zero, validating stability criterion.

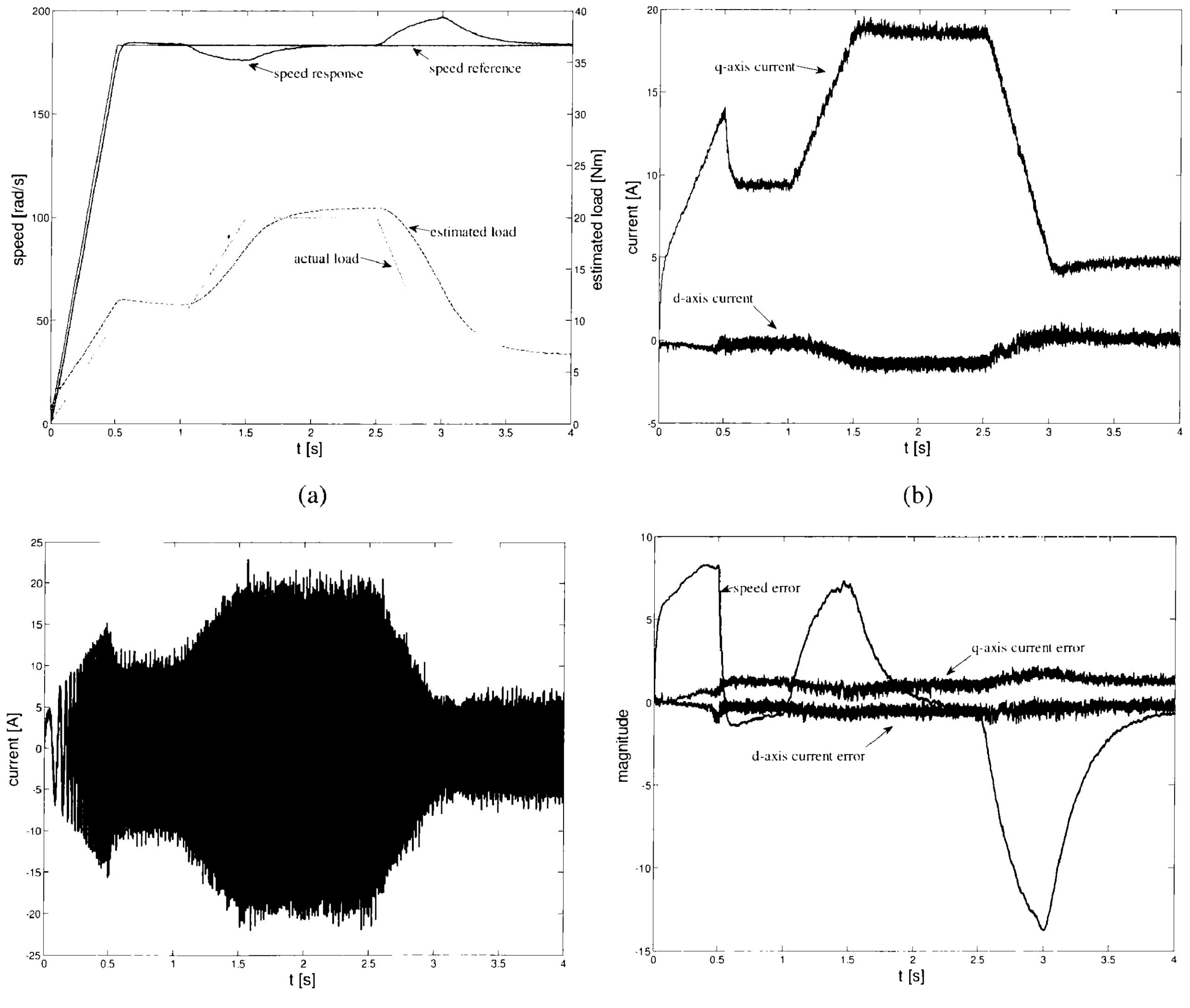

Figure 5-4: Load variation: a) Speed response b) d-q axis currents c) phase current d) error dynamics

To demonstrate the validity of the assumption of a negligible zero axis component necessary for control design, Figure 5-5 below shows the balanced phase currents at rated conditions. The carrier frequency is maintained at a value that accurately reflects the limitations of the experimental setup, which is limited to a 5 kHz carrier frequency at absolute maximum.

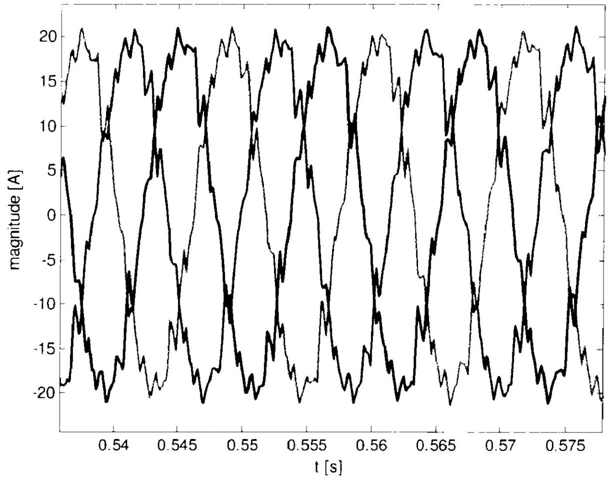

Figure 5-5: Balanced phase currents

5.3.3 Comparative Analysis

Performance of the proposed controller is compared to existing control methods, including PI controllers using hysteresis current and carrier based modulation schemes. Performance is contrasted for ramp changes in motor load at rated speed for the proposed and hysteresis PI controller in Figure 5-6. Load is initially 50% of rated and then increased to 100% from t=1.0s to t=1.5s, finally the load is reduced to 25 of rated from t=2.5s to t=3.0s. The proposed controller is able to recover from load disturbances more rapidly, and with less overshoot and undershoot than the PI hysteresis controller. Both controllers are using identical MTPA algorithms for d-axis current reference for directly comparable results.

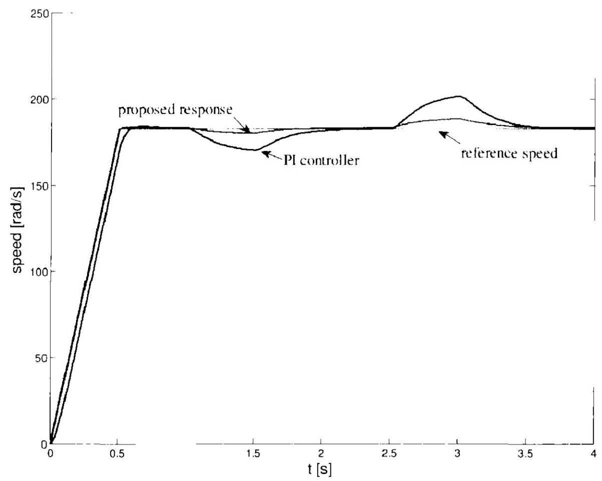

Figure 5-6: Controller speed response comparison of PI and proposed controller

Further comparisons are shown below in Figure 5-7 and Figure 5-8 with respect to a PI controller with carrier based modulation, which is the same modulation technique used by the proposed controller. This gives a more direct comparative analysis, as the modulation framework is the same. In Figure 5-7a, the responses of the proposed controller and PI controller are shown for ramp changes in load occurring over 0.5s intervals. First, increasing up to 50% rated load from t=0s to t=0.5s, to rated load at t=1.5s, and back to 25% rated load at t=2s. The proposed controller exhibits a faster response to variation in the load with less overshoot and quicker convergence to the set-point than the PI controller. In Figure 5-7b, the corresponding d-q axis currents are shown, which clearly demonstrate that even with the MTPA algorithm common to both controllers, the PI controller is mostly unable to force the trajectory below or near zero. Thus, the performance of the proposed controller is again demonstrated to be superior to the PI controller using the same modulation scheme.

Figure 5-8 shows the comparison of the proposed controller and PI controller for a series of speed changes, including ramp and relative small step changes. Again, Figure 5-8a shows the speed response, with the proposed controller demonstrating less over and under shoot than the PI controller. In Figure 5-8b, the d-q axis currents are compared, with the proposed controller exhibiting better control of the d-axis current during the speed reference changes.

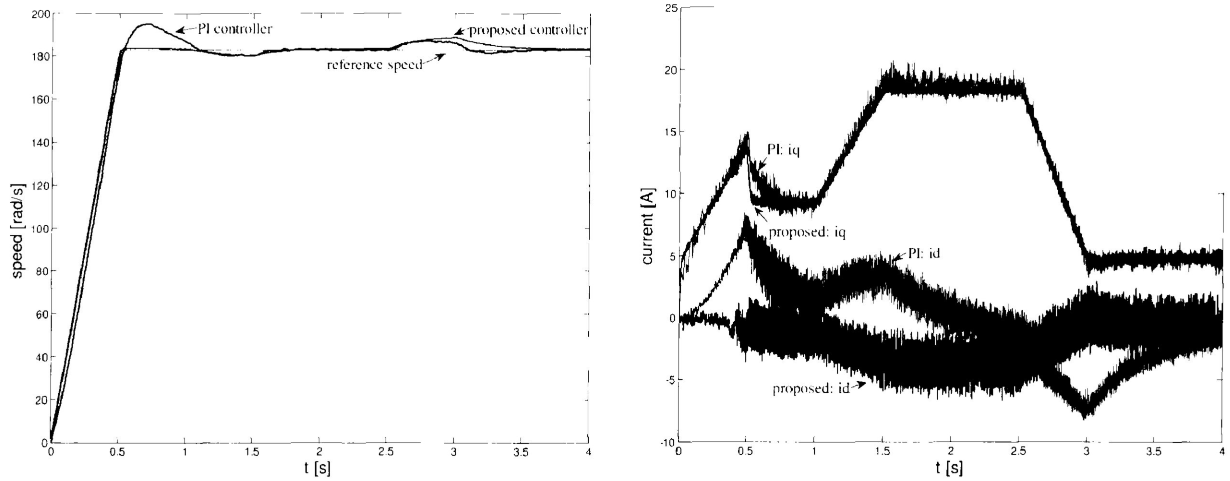

(a) (b)

Figure 5-7: Speed response comparison of PI and proposed controller a) speed response b) d-q axis currents

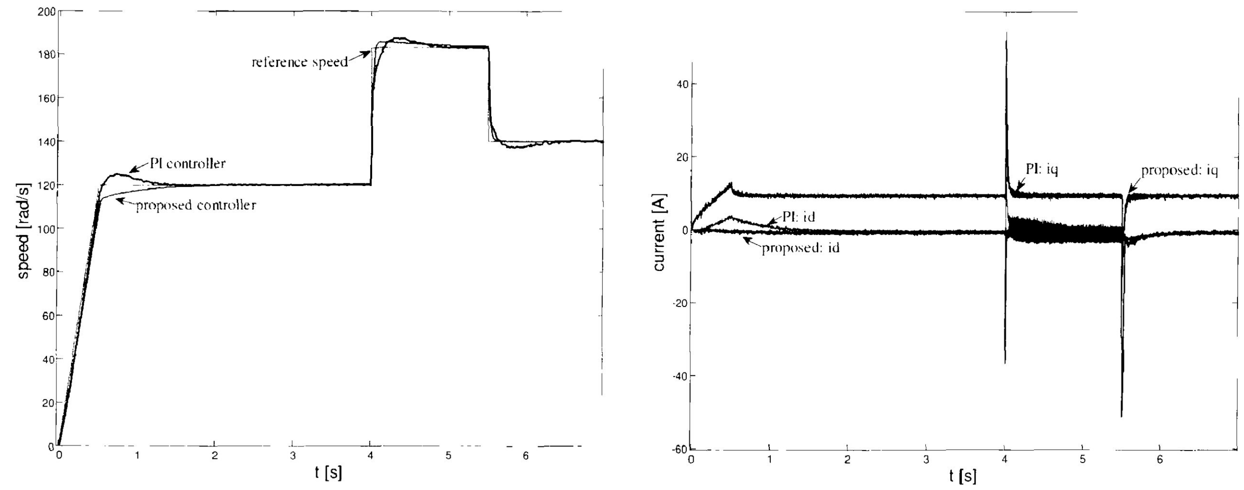

Figure 5-8: Speed response comparison of PI and proposed controller: Speed change a) speed response b) d-q axis currents

5.3.4 Harmonic Analysis

To demonstrate the additional performance possible with harmonic injection for naturally sampled modulation, the following results show phase current, frequency analysis and total harmonic distortion of the phase current with and without triplen injection. Several carrier frequencies are tested in simulation, a low frequency at 1.2 kHz to emulate the real-time experiment, and a higher carrier at 4.2 kHz to illustrate the significant improvement in harmonic distortion possible. Further details regarding experimental limitations are detailed in Chapter 6. The motor is run at rated speed and load, and for a fixed supply voltage is tested with triplen injection and without. The phase current is shown in Figure 5-9a, and demonstrates a reduction in peak phase current through the use of triplen. For the same phase current, a frequency domain analysis is performed, and shows a reduction in low frequency harmonics for the scenario using triplen injection.

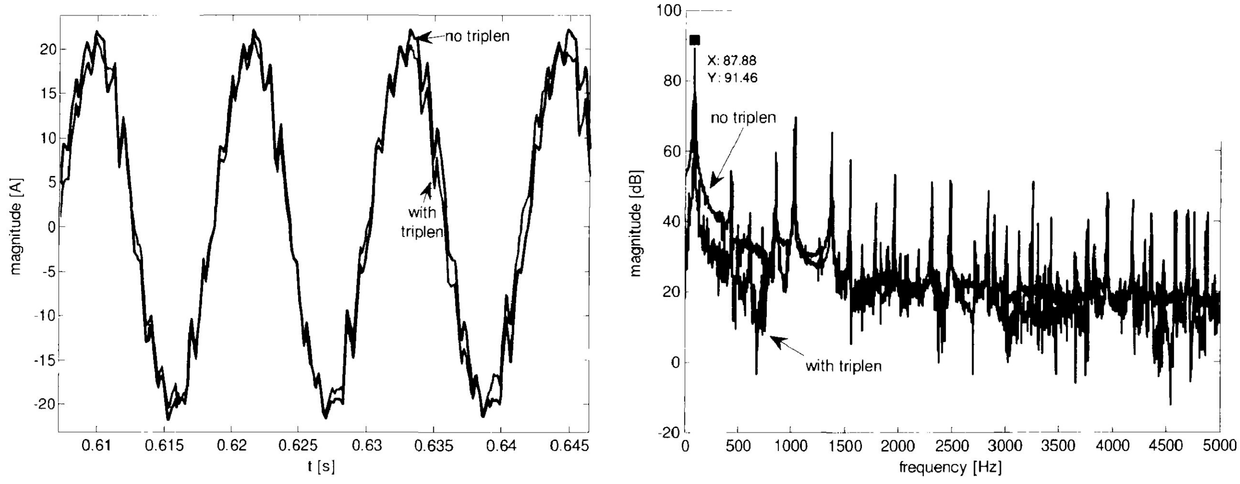

(a) (b)

Figure 5-9: Harmonic Analysis: a) Phase current b) Frequency spectra

To provide more detail on the relative total harmonic distortion (THD) and amplitude modulation index (m_a), the following table details the results for different carrier frequencies. Again results are tabulated for rated operating conditions, with a fixed voltage supply such that results are comparative. Table 5-1 demonstrates that with triplen harmonic injection, there is an effective reduction in THD corresponding to a lower amplitude modulation ratio, indicating operation remains within the linear modulation range.

Table 5-1: Harmonic Content

Triplen injection	Carrier frequency [kHz]	m_a [ratio]	THD [%]	Speed [rad/s]
$\frac{1}{6}\sin 3\theta$	4.2	0.976	2.749	183.3
none	4.2	1.156	3.122	183.3
$\frac{1}{6}\sin 3\theta$	1.2	0.96	9.914	183.3
none	1.2	1.116	10.85	183.3

5.4 Conclusion

The simulation results shown for the proposed controller have demonstrated excellent performance, including rapid convergence, accurate tracking and disturbance rejection. For clarity only the most pertinent results have been shown, with a focus on system dynamics, comparative analysis and harmonic distortion content. Harmonic analysis indicates the benefit of the triplen injection with lower THD corresponding to a linear amplitude modulation ratio and an improved supply transfer ratio. Results indicate the superiority of the proposed controller over conventional schemes using PI controllers in systems with both hysteresis current and carrier based modulation. The following chapter continues the testing of the proposed controller in real-time using the DS1104 embedded control and data acquisition platform.

Chapter 6

Real Time Implementation

Simulation results may be used as an indication of relative performance, however are insufficient and ultimately do not provide realistic enough results to make appropriate conclusions. Consequently, it is essential that validation of the proposed controller is achieved through performance testing in a real time environment. At the core any the real-time discrete control system is the digital signal processor (DSP) often referred to as the microcontroller (MCU) in embedded systems applications. The MCU computes the control outputs based on the control laws and delivers the pulse width modulated (PWM) signals to the inverter. In the context of this thesis, the discrete time system is comprised of a master and slave MCU, which collectively manage feedback, execute control laws and generate PWM outputs. Output of MCU is connected to the inverter, which commutates each phase of the connected 3-phase motor, as per Figure 6-1. Feedback from the motor exists in the form of measured shaft position and two of the phase currents (i_a, i_b), following the previously stated assumption of balanced phase currents. See Appendix D for details on the experimental interface circuit for the inverter level shifter and feedback buffers.

6.1 Hardware Overview & Experimental Configuration

Typically, most motor drive systems incorporate or are comprised of the same general functional components. Those major components are detailed below in Table 6-1, in conjuncture with the specific rating and manufacturer details that pertain to this thesis work. Notably, both an IPMSM and induction motor (Appendix F) have been tested in this thesis, such that the specifications are detailed for all hardware used, where applicable.

Table 6-1: System specifications & ratings

System Component	Manufacturer	Model	Characteristic(s)	Specification	Notes
Controller Board	dSPACE GmbH	DS1104	Clock frequency	250 MHz	
			ADC	16-bit	
			DAC	16-bit	
			Encoder	10-bit	
			PWM	12-bit	
Inverter	Semikron		DC supply	<750v	
			Phase current	<30A	
			Drive input	0/15v	
Motor	Yaskawa	686SS	see Table 1		IPMSM
	Baldor	CHM545A	Voltage	230v	Induction
			Current	3.2A	
			Torque	4.07Nm	
Current sensor		CS100A-P	Current rating	<100A	
Position sensor	Sumtak	LMA-102	Supply	12v	
			Resolution	10-bit	
Power Supply	Sorensen	SGA 200/25	Voltage	200v	SMPS
			Current	25A	
			Ripple	0.02%	

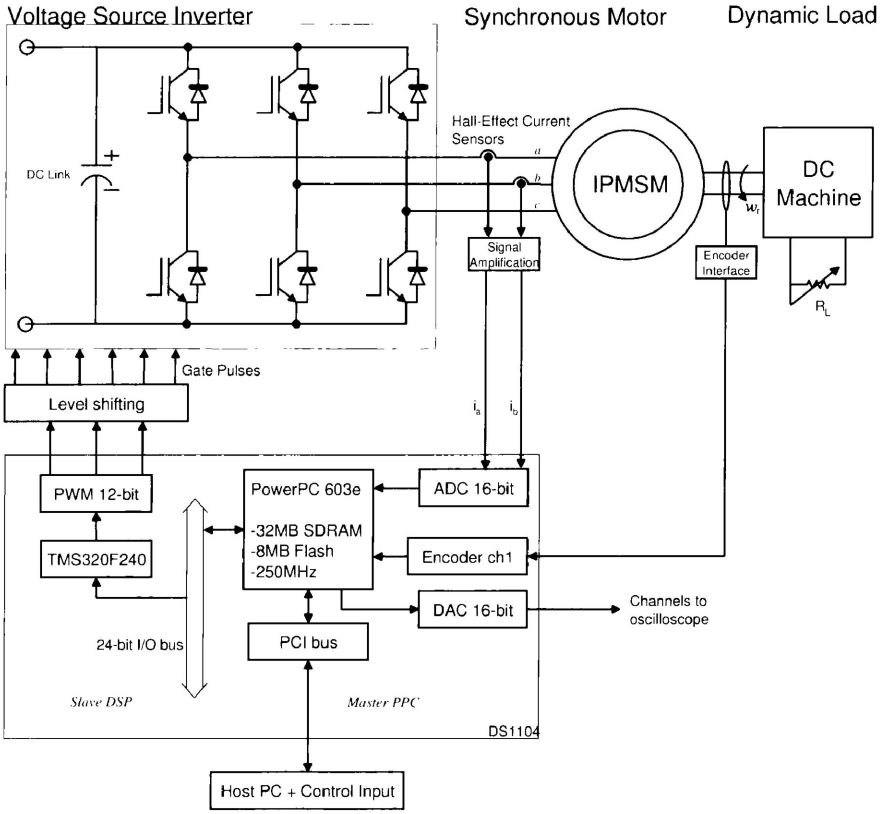

Figure 6-1: DS1104 based experimental system for the proposed controller

Each major aspect of the experiment is detailed in the following subsections, and for reference, the experimental environment is shown in Figure 6-2. Each major component of the experimental system is labelled in the figure, with the IPMSM depicted being the Yaskawa 3.7kW drive (for further details, see Appendix A). All connections on the DS1104 controller board are interfaced through the CP1104 connection panel which is referenced in Figure 6-2 and depicted in Figure 6-4. All oscilloscope images shown in this thesis are sourced from the Tektronix oscilloscope shown in Figure 6-2.

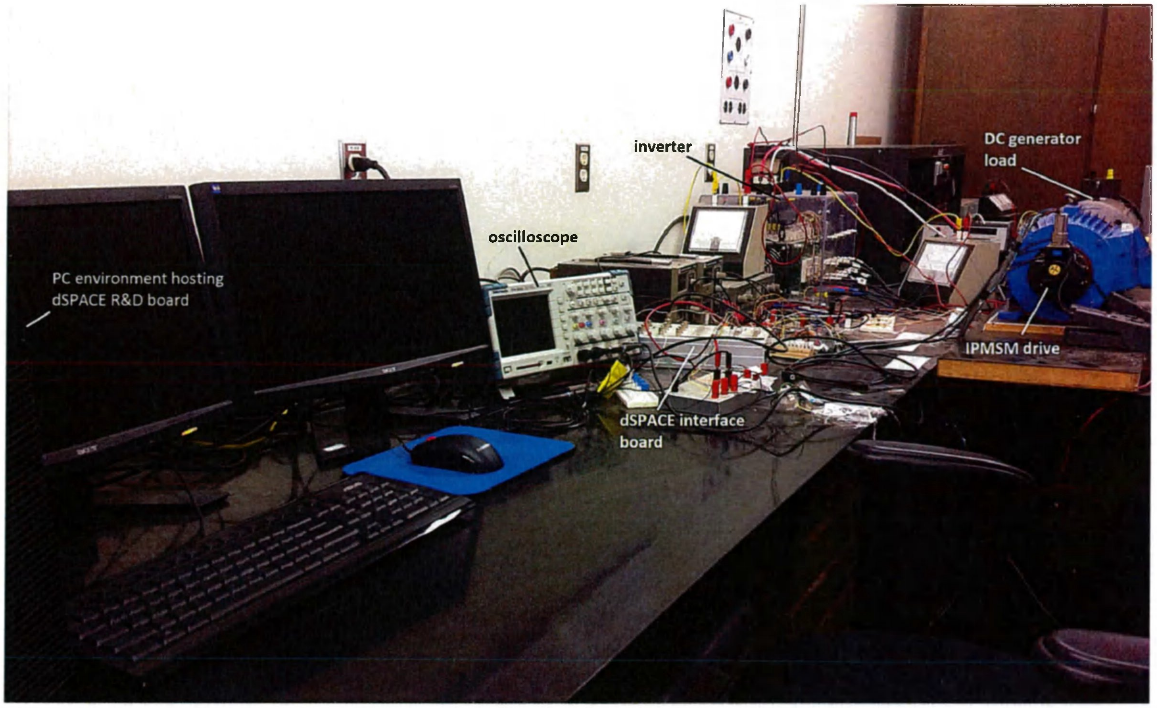

Figure 6-2: Experimental set-up

6.1.1 Embedded System

The DS1104 controller board is implemented on a peripheral component interface (PCI) bus on the host computer, and with the exception of power connections and communication (data, programming) with the host, all controller computations are performed on the DS1104. Data from the ControlDesk[14] user interface for command variables is sent to the DS1104, and data is returned to the user interface for monitoring system variables in real-time. The system may be controlled and monitored through the ControlDesk real time interface (RTI), as per Figure 6-3. This enables the user to create custom graphical interfaces, adding to the functionality of the DSP. For this thesis work, an interface was created to visualize the dynamic plots of command voltages, error dynamics, speed and load estimation; as well as view instantaneous values of key variables and send parameter/set-point variations to the DSP. Further implementation examples of the ControlDesk interface may be found in Appendix E.

---

[14] Trademark of dSPACE

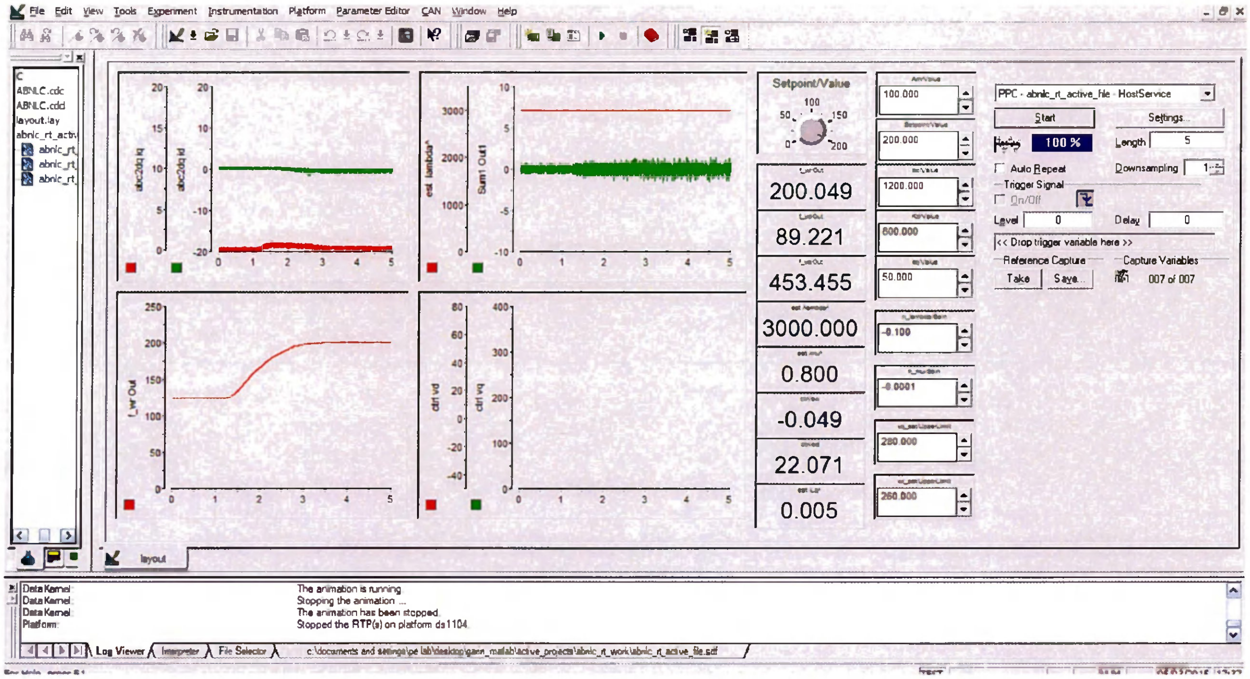

```
Data Kernel:    The animation is running.
Data Kernel:    Stopping the animation ...
Data Kernel:    The animation has been stopped.
Platform:       Stopped the RTP(s) on platform ds1104.
```

c:\documents and settings\pe lab\desktop\gann_matlab\active_projects\abnlc_rt_work\abnlc_rt_active_file.sdf

Figure 6-3: DSPACE ControlDesk Interface

The DS1104 I/O for both the master and slave processors is made available through a connector panel (CP1104), exterior to the computer host. This interface arranges the I/O as per the following diagram, inspired from [35].

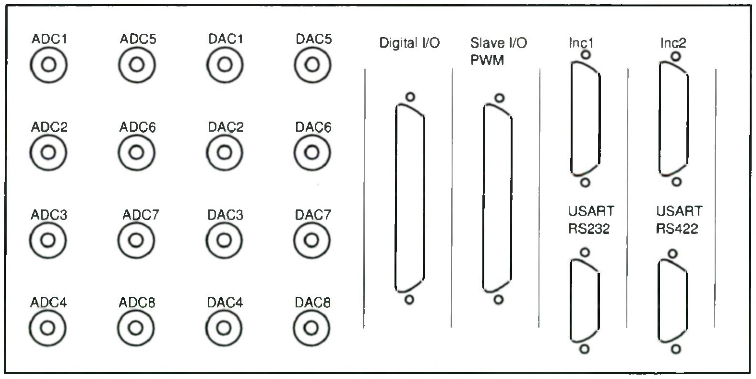

Figure 6-4: CP1104 connection panel

In brief, the slave I/O is used for PWM output to the inverter, encoder is connected to "*Inc1*", the current feedback is fed into "*ADC1/2*" and visualization of key system variables on an external oscilloscope may be achieved by using the 8 available digital to analog converter (DAC) channels.

6.1.2 Embedded Code Development

The runtime code that is loaded on the DSP board is compiled and assembled through Simulink using background referenced C compilers (see Appendix C for Simulink model). The real time model is constructed in Simulink using standard MATLAB computational mathematics features in conjuncture with I/O interface modules from the "rtilib1104" library, developed by dSPACE GmbH and integrated into MATLAB. The RT Simulink file is compiled using "*Microtec PowerPC C Compiler*", a compiler that is installed in parallel with the dSPACE software and may be found in the root system folder [36]. Executable files with extensions of "*.obj*" and "*.ppc*" are created during the compilation/linker process and are loaded onto the slave and master processors respectively. Due to the relative complexity of the control algorithm, and the limitations of the DSP board, the closed loop execution rate is 100us. This is the sample time (T_s), and is the delay between each feedback sample iteration and the application of the updated PWM output.

6.1.3 Feedback Systems

As part of closed loop control system, feedback is essential, and for the controller proposed in this thesis position and phase current are required variables. Position and indirectly angular velocity are measured using a 10-bit two quadrant indexed optical encoder with complementary outputs. The encoder is connected to "*Inc1*" on the connection panel, as seen in Figure 6-4, and the encoder configuration is set to TTL to match the complementary signals. The current feedback is acquired through dual hall-effect based sensors on phases "a" and "b", the sensor signals are conditioned and amplified to the 5V level before being fed into the "ADC1" and "ADC2" analog to digital channels on the CP1104 (Figure 6-4). Please refer to [35] - [37] for further details on the real-time usage and configuration of the DS1104 controller board and the appropriate pin connection on the CP1104.

6.1.4 Inverter Supply

The inverter is supplied from one of two alternate sources, a 200V switch mode power supply (SMPS) or through an uncontrolled rectifier fed by a variable ac transformer. The SMPS is characterized by low ripple output for more accurate characterization of the motor phase current distortion during operation. The SMPS, a Sorensen SGA-200/25 supply has a rated maximum output of 200V, 25A with 0.01% voltage line regulation[15] [38]. This ripple specification is considered as comparable to the lab implementation as the leads used are 8 foot 10 gauge copper strand with more than 1uF at the inverter end.

To drive the inverter for rated motor operation (260V line-line), a three phase variable transformer is used, capable of supplying up to 600V through an uncontrolled rectifier. Use of this power supply invariably results in greater phase current noise content, and as such is primarily used for higher speed operation of the IPMSM.

6.1.5 Dynamic Load

As per Figure 6-1, the dynamic load applied to the system is provided by a DC machine operating as a generator, with a variable resistive load connected to the terminals. For the "no-load" testing, the DC machine was disconnected from any resistive load such that the IPMSM under test only experiences additional inertial and frictional loading.

6.2 Experimental Results

All results detailed in this section are characterized by oscilloscope images with division markers for each channel active, these per division magnitudes may only be literally interpreted for measured voltages due to unit display limitations. In the caption of each oscilloscope image, the effective (actual) magnitude per division is noted, dependant on probe scaling, pre-scaling in the system or other factors. Time base is detailed within the oscilloscope image and is not further emphasized, design coefficients are fixed for each test scenario, as shown in Table A-3.

---

[15] Measured peak to peak output ripple of 175mV as measured at the end of a 6 foot cable across a 1uF capacitor [38]

Results are broken into two main following subsections; the first detailing dynamic performance and the second illustrating steady state performance and harmonic content. Dynamic performance includes the system response to reference speed step increases and decreases as well as an analysis of the transition between MTPA and FW modes and the effect on line-line voltages. The results detailed show the evolution of controller testing from low to high speed operation in order to establish performance over the full operating range. Subsequent steady state performance analysis demonstrates the proposed controllers stability, load disturbance rejection and harmonic content with and without triplen injection. Key comparisons of the proposed controller are made to a PI hysteresis current controller to demonstrate comparative performance advantages of the proposed controller for load disturbance rejection and utilization of i_d.

6.2.1 Dynamic Performance

This section explores the dynamic performance of the proposed nonlinear controller for step speed reference changes with inertial loading only. To provide an accurate picture of the motor variables during a reference speed change, motor speed, phase currents and d-q axis currents are typically shown on the same oscilloscope screen. The organization of this section is made such that results are ordered with increasing speed, starting with speed step changes below rated speed and proceeding to above rated speed operation. Results for a step decrease in speed are also shown, and compared to a PI hysteresis current controller. Finally, results including the motor terminal voltage are shown for a step increase in command speed to demonstrate that terminal voltages are maintained constant and within rated voltage. All results shown in this section are the subject of frictional and inertial loading due to the DC generator attached to the IPMSM shaft. Where relevant, the speed command has been indicated on the oscilloscope images with a black line, such that the motor speed reference is clear.

An initial low speed reference speed change is made from 0-70 rad/s in Figure 6-5, with the mechanical angular velocity shown in (a), the d-q axis currents in (b) and the error dynamics in (c). This step response occurs with an inertial/frictional load represented by the DC generator with no resistive load. The response demonstrates the controller's ability to converge rapidly to steady state command speed, with error dynamics decaying to zero in steady state.

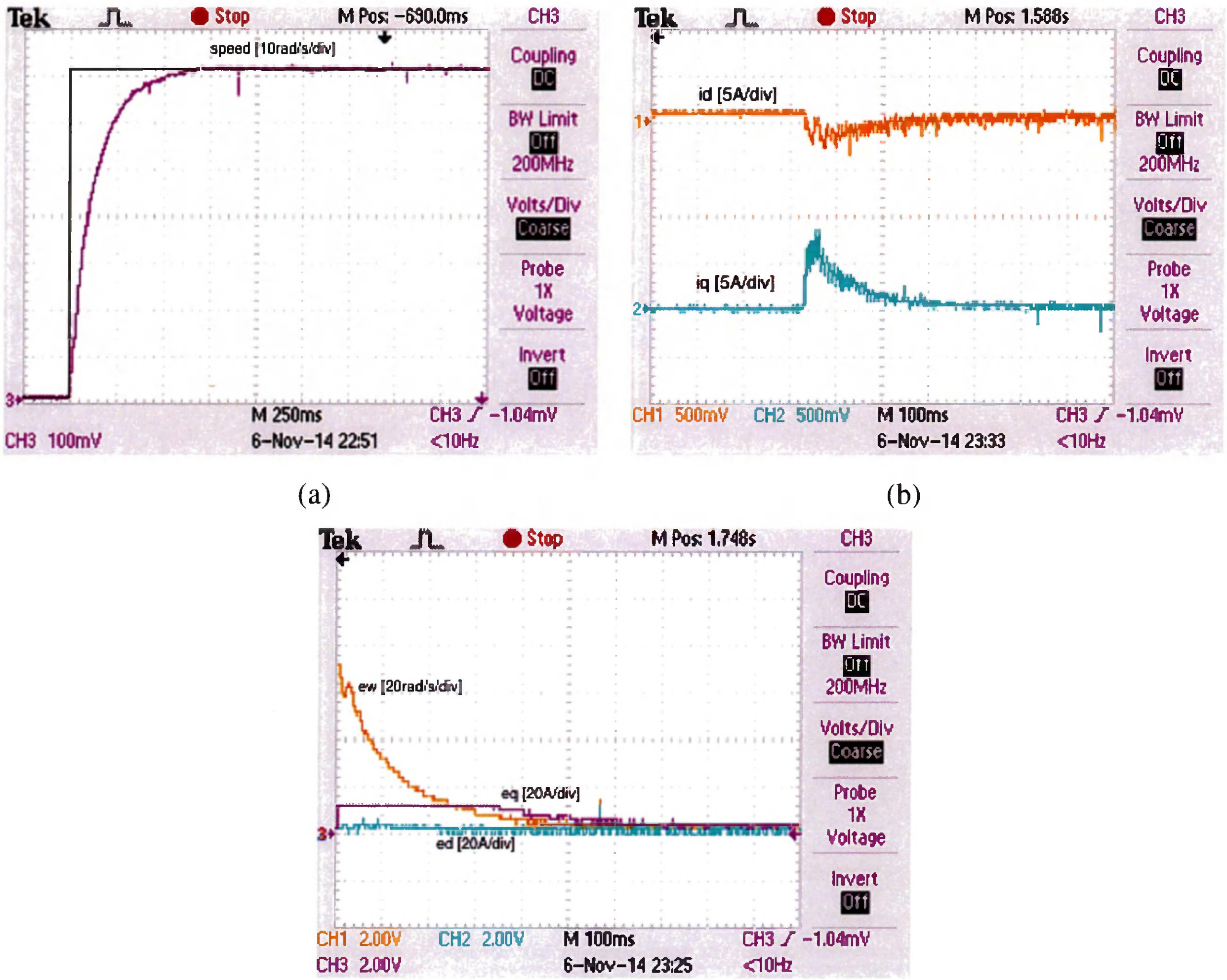

(a)

(b)

(c)

Figure 6-5: Speed step response of the proposed controller (0-70rad/s): a) speed b) d-q axis currents c) error dynamics

In Figure 6-6, a step command in reference speed is made from 20-100 rad/s and shows the response of the proposed controller. During the step command in speed, the proposed controller demonstrates a rapid convergence to the command speed, with excellent control of the d-axis for additional developed reluctance torque.

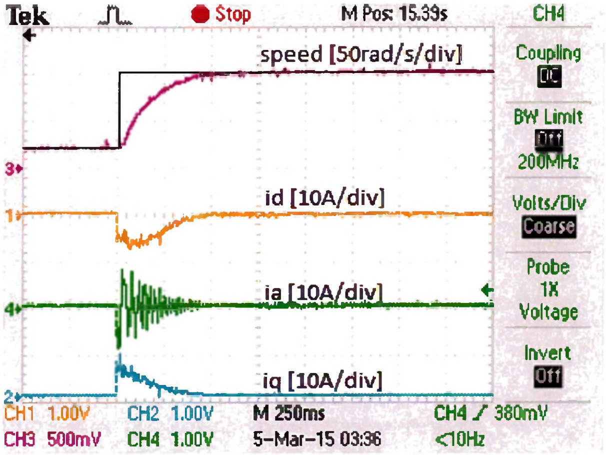

Figure 6-6: Speed step response (20-100rad/s) of the proposed controller

To better demonstrate the current dynamics during a speed step change, Figure 6-7 shows a speed change from 50-100 rad/s and reduces the magnitude per division on the oscilloscope for the phase and d-q axis currents. This closer view permits a closer view of i_d and i_q during the command speed step increase to 100 rad/s, and clearly demonstrates the contribution of the d-axis current during and after the speed change.

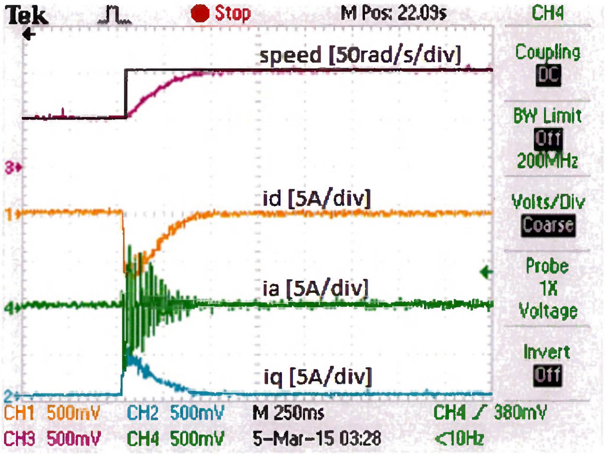

Figure 6-7: Speed step response of the proposed controller (50-100rad/s)

In order to demonstrate the operation of the proposed controller in the transition from MTPA to FW control, Figure 6-8a shows a step response from 50-120 rad/s with the switch between current control modes set to occur at 110 rad/s. The figure shows the switching point, indicated by a vertical line, where the proposed controller transitions from maximum torque per ampere to field weakening control. For illustrative purposes, the controller has been programmed to switch from MTPA to FW control at 110 rad/s and thus reaches 110 rad/s before switching to FW and increasing to the commanded speed of 120 rad/s. In Figure 6-8b, the proposed controller responds to a step command in speed from 100-200 rad/s with the controller switching from MTPA to FW control at rated speed. These results demonstrate the flexibility of the proposed control algorithm and how it can be adapted for different operating speed ranges and supply voltages depending on requirements.

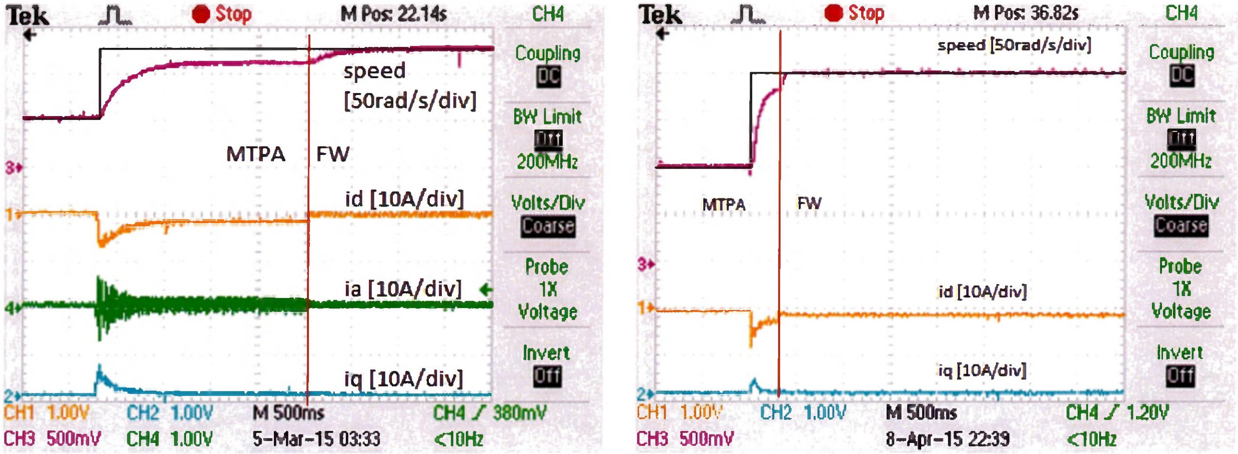

Figure 6-8: Speed step response, switch from MTPA to FW: a) 50-120rad/s inertial loading b) 100-200rad/s no load

The following results detail speed step changes at higher speeds than previously shown. At these higher speeds, the contribution of i_d is more significant, and can clearly be observed in the following figures. To show a more detailed view of the d-q axis currents during a step change from, Figure 6-9 shows operation of the proposed controller for a step change from 130-160 rad/s in (a) and a step change from 140-170 rad/s in (b). Both images demonstrate the contribution of the d-axis current for additional developed reluctance torque.

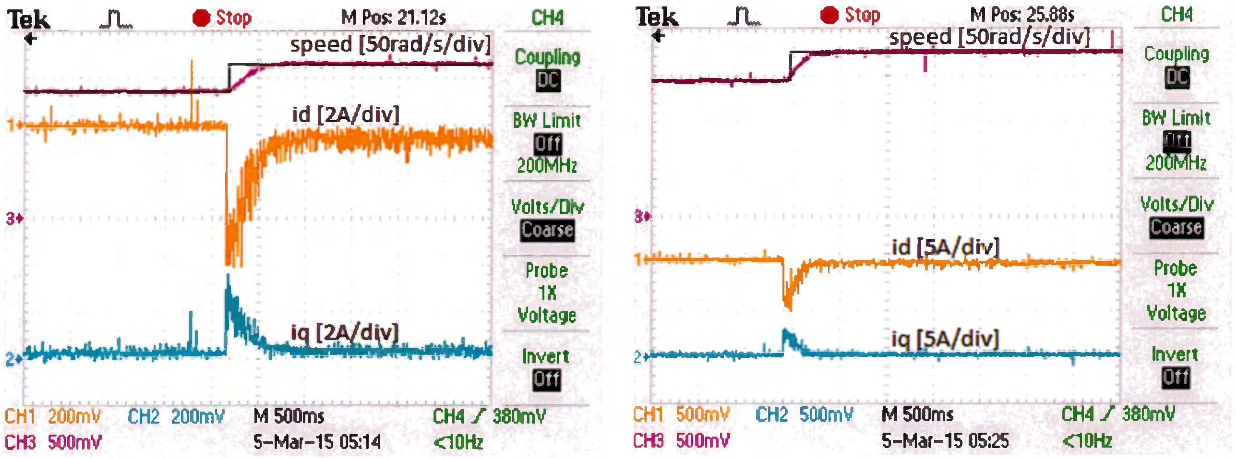

(a) (b)

Figure 6-9: Speed step response of the proposed controller: a) 130-160rad/s b) 140-170rad/s

The results in Figure 6-10 again demonstrate the comparative performance of the proposed controller to that of the PI hysteresis current controller. The proposed controller demonstrates rapid convergence to the command speed, with better control of the d-axis current than the PI controller, both during and after the speed step command. Further, the PI hysteresis current controller exhibits slight overshoot for the speed step command.

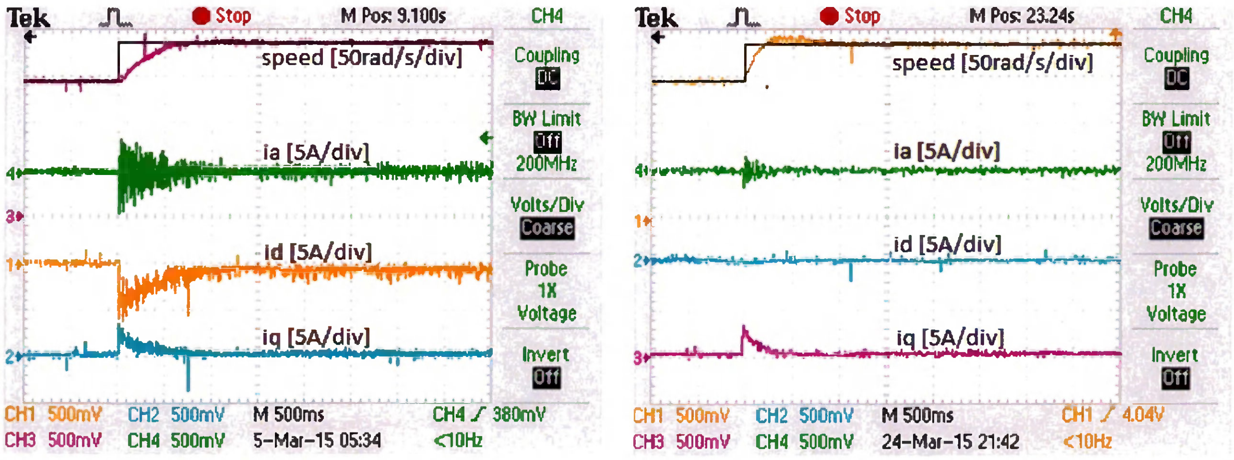

(a) (b)

Figure 6-10: Speed step response (140-180rad/s): a) proposed controller b) PI hysteresis current controller

In Figure 6-11, the step command is from 150-183 rad/s and is intended to illustrate controller operation for a more extended time interval than previously shown. The time base of the oscilloscope is increased to show the stability of the controller over a 22s interval following the step change in command speed. This result demonstrates operation of the proposed nonlinear controller at rated speed following a step change in command speed.

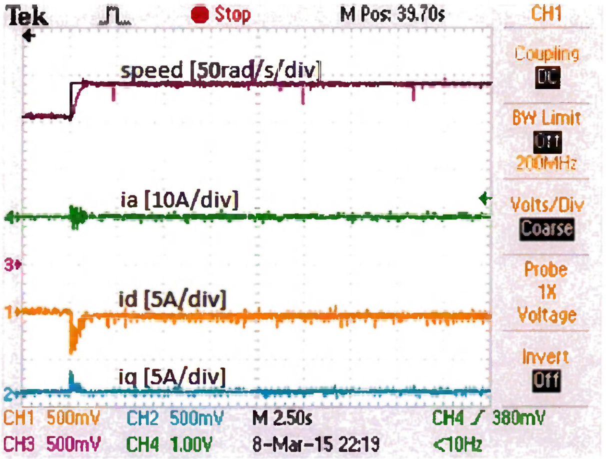

Figure 6-11: Speed step increase of the proposed controller (150-183rad/s)

To demonstrate the operation of the proposed controller above rated speed, the following Figure 6-12 shows two scenarios; in Figure 6-12a the command speed is stepped from 160 rad/s to 200 rad/s, and in Figure 6-12b the speed is commanded from rated to 210 rad/s. The controller is operating in the FW region and as a result d-axis current contribution is more significant than below rated speed.

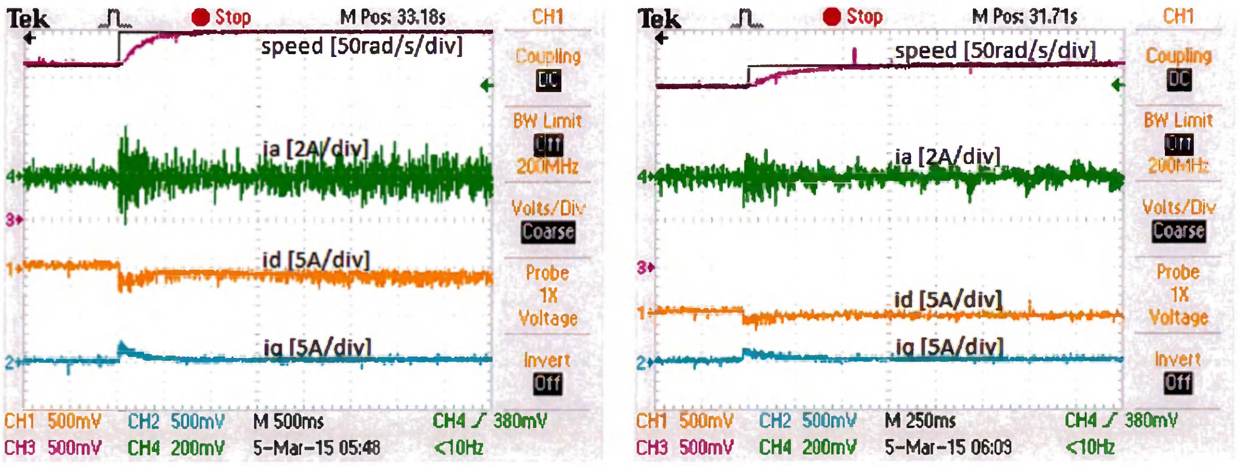

(a) (b)

Figure 6-12: Speed step response of the proposed controller: a) 160-200 rad/s b) 183-210 rad/s

Significant results have been shown for speed step changes involving an increase in speed. In order to demonstrate the proposed controller performance for a step decrease in speed, several results are shown in the following diagrams, for different step speed reductions and in comparison to a PI controller using hysteresis current modulating technique.

In Figure 6-13, the command speed is stepped down from 100 rad/s to 50 rad/s for both the proposed controller and the PI hysteresis current controller. The only load applied to the motor is inertial load, which is consistent throughout this section. The proposed controller is able to track command speed without any undershoot (no braking action) and more rapidly than the PI controller which exhibits slight undershoot before converging to the command speed.

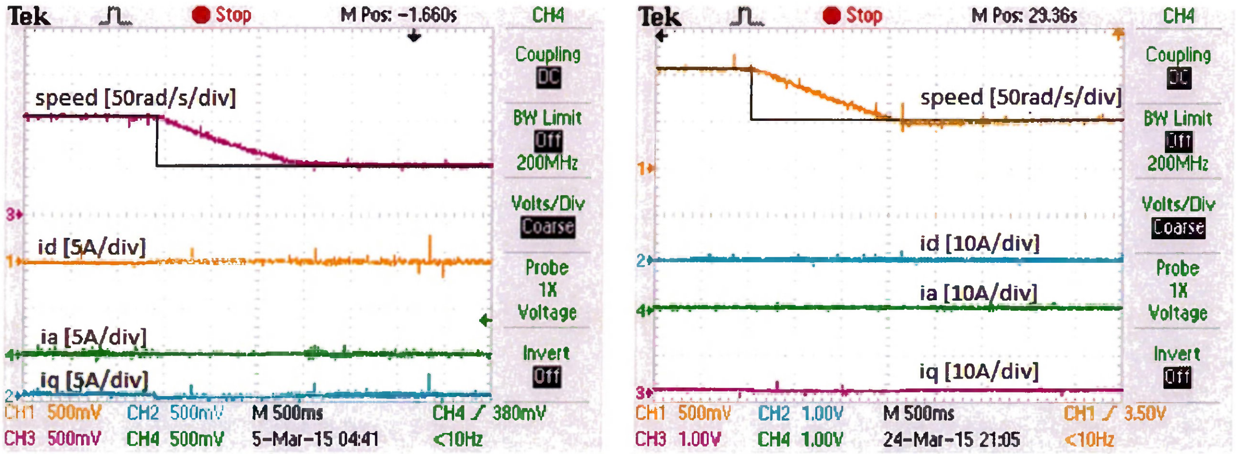

(a) (b)

Figure 6-13: Speed step decrease (100-50rad/s): a) proposed controller b) PI hysteresis current controller

To further demonstrate the proposed controller's ability to follow a step reduction in command speed, Figure 6-14 shows a step speed from above rated speed (200 rad/s) to rated speed (183 rad/s). This step reduction in command speed proves proposed controller performance above rated speed, in the FW region of operation. The d-axis current can clearly be seen returning to near zero from a negative state when the speed command is made, and the controller converges to the command speed without any undershoot.

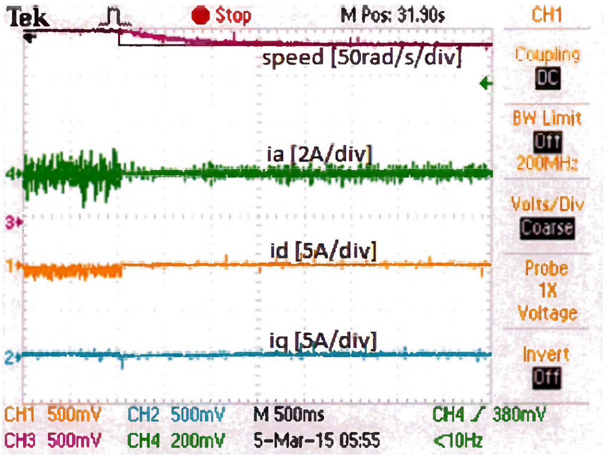

Figure 6-14: Speed step decrease of the proposed controller (200-183rad/s)

To verify that the proposed adaptive controller is successful in maintaining the terminal voltage of the motor at a specified level, the following result details a step responses of the proposed controller above rated speed to 200 rad/s. Figure 6-15 shows the line-line (terminal) voltage of the motor for a step change from 183-200 rad/s with inertial loading. The terminal voltage can be seen at a consistent level during the speed change transition, with the d-axis current responsible for maintaining air gap flux levels for a constant terminal voltage. This result clearly demonstrate that the controller is able to accurately control the motor terminal voltage above and below the rated speed during and after a speed command step change.

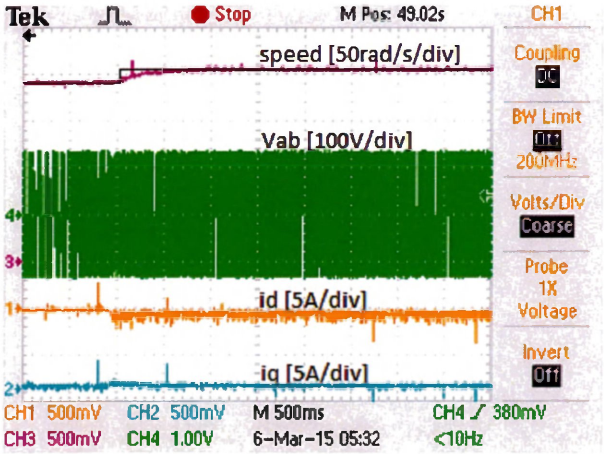

Figure 6-15: Line voltage for the proposed controller for a step command of 183-200rad/s

To demonstrate the performance of the adaptive aspect of the proposed nonlinear controller, the following results show system dynamics with and without the adaptive laws engaged. Without the adaptive laws, the mechanical coefficient was set at nominal and the load set at a value reflective of the frictional load seen by the IPMSM (due to the DC generator). In Figure 6-16, two parameter adaptation scenarios are shown, where the adaptive laws are activated during operation. In Figure 6-16a, parameter adaptation is initially off, then during steady state operation the adaptive laws are activated. The motor speed can be seen to converge to the command value of 100 rad/s only when the adaptive laws are active (indicated by the vertical line), and demonstrates the necessity of the adaptive component of the proposed controller for operation at any different operating point. In Figure 6-16b, the command speed is set at 150 rad/s and the load is increased from 20-27% of rated load, with the adaptive laws deactivated. It can be clearly seen that without the adaptive laws engaged the motor speed drops below the command speed when the load is changed. This demonstrates that operation at a specific operating point is possible without adaptive laws, however any deviation from that point results in slight divergence from the command speed. Following the load change without parameter adaptation, the adaptive laws are activated, and the motor converges quickly to the command speed of 150 rad/s. These results clearly establish both the necessity and the additional performance benefit possible with adaptive control laws as part of the nonlinear controller.

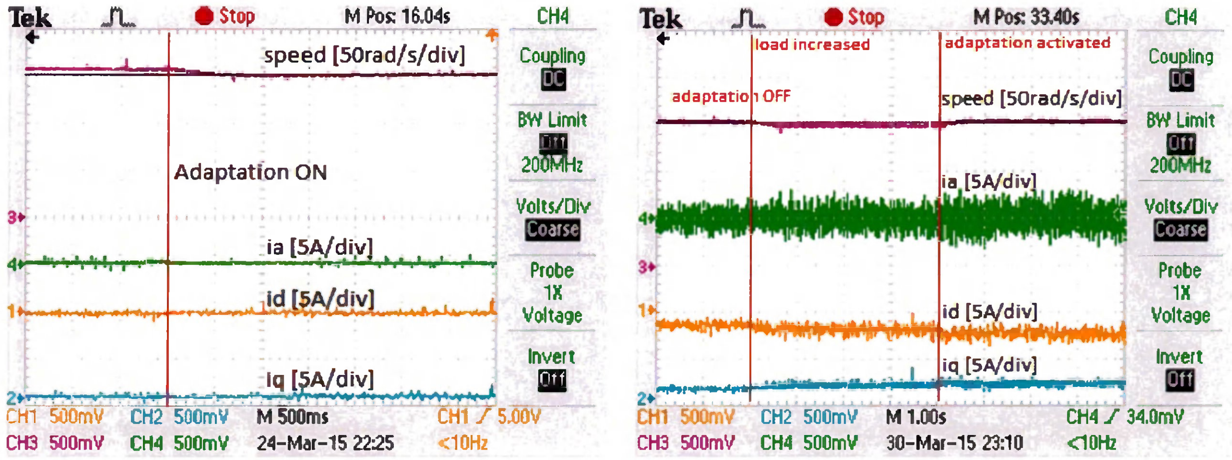

(a) (b)

Figure 6-16: Parameter adaptation of the proposed controller, 150 rad/s: a) parameter adaptation activated, inertial load b) parameter adaptation activated during load change (20-27%)

6.2.2 Steady-State Analysis

The results in this section illustrate the steady state operation of the proposed controller at different loads and speeds. Results are shown for several speeds at different loading points as well as with triplen injection to illustrate the difference in distortion of the d-q axis currents. In order to establish the performance of the proposed controller, comparison is made to a PI hysteresis current controller for load disturbance rejection. Additionally, the balanced three phase currents are shown in steady state operation, as a necessary validation of the assumption made for control and reference frame development.

Figure 6-17 shows the steady state operation of the proposed controller at low speed with only inertial loading, phase current and d-q axis currents are shown to demonstrate basic steady state operation of the controller. Again, all traces are labelled on the oscilloscope image and magnitude per division is also indicated for each relevant channel.

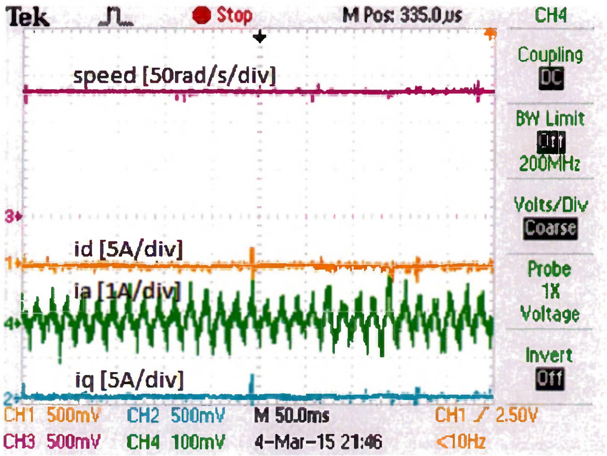

Figure 6-17: Steady state operation of the proposed controller at 130 rad/s

The results in Figure 6-18a & Figure 6-18b show the proposed controller operating at 100 rad/s with 20% rated load without and with triplen injection respectively. Without triplen, in Figure 6-18a, the ripple in i_d and i_q is significant. With the triplen injection, it can be seen by both the ‘a’ phase current & d-q axis current traces that there is a reduction in distortion.

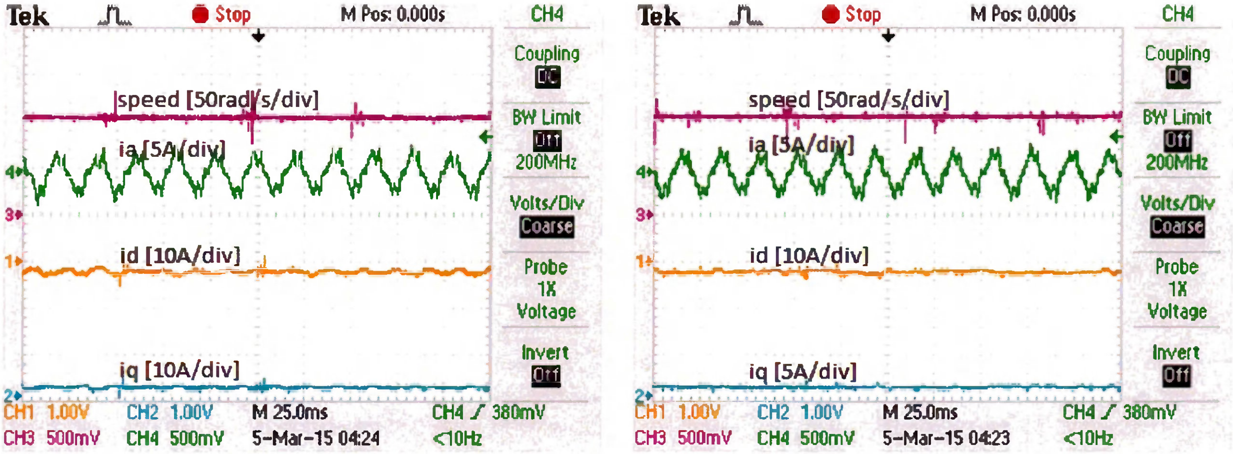

(a) (b)

Figure 6-18: Steady state operation of the proposed controller 100 rad/s, 14% rated load: a) without triplen injection b) with triplen injection

To demonstrate the ability of the proposed controller to reject load disturbances, the following results show the speed response and current magnitudes during loading variations, again all traces are labelled on the oscilloscope capture along with magnitudes/division. The proposed controller in Figure 6-19a is able to maintain command speed with negligible variation, compared to the PI controller in Figure 6-19b, which exhibits a slightly more protracted convergence back to set-point. The proposed controller also utilizes the negative d-axis current to contribute to developed torque, compared to the PI controller, which uses the same MTPA algorithm and demonstrates negligible variation in i_d.

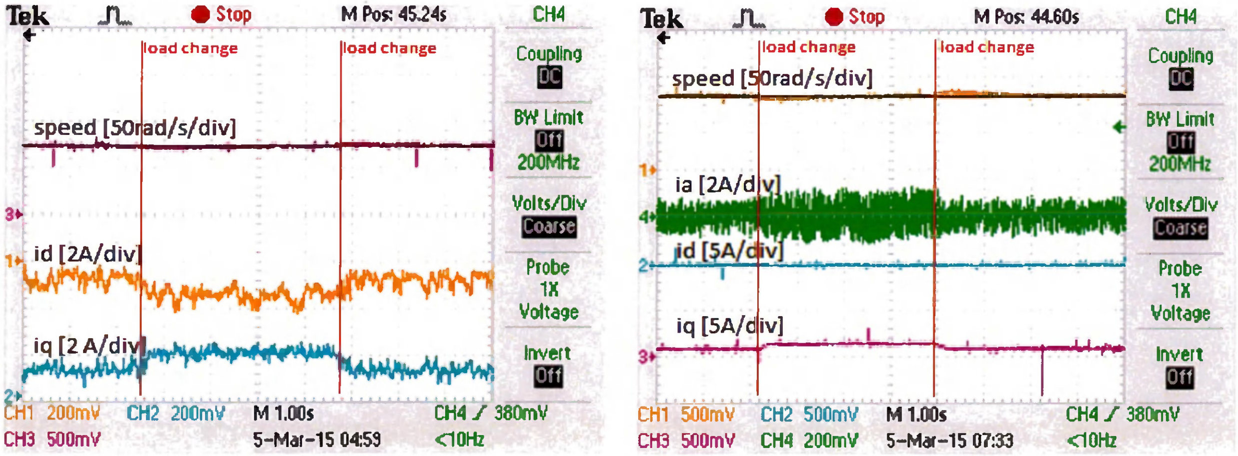

(a) (b)

Figure 6-19: Load step change from 10-17% at 70 rad/s: a) proposed controller b) PI hysteresis current controller

To further demonstrate the performance of the proposed controller for step changes in load, Figure 6-20 shows the speed response for a load step change from 0-10% rated load. The controller is able to maintain commanded speed without any noticeable deviation, and i_d is controlled such that a fraction of the developed shaft torque is due to reluctance torque.

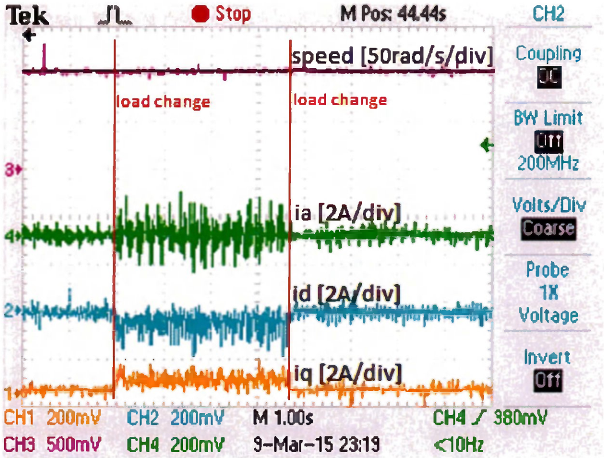

Figure 6-20: Load step change of 0-10% at 100 rad/s for the proposed controller

Two more sets of load disturbance tests are performed for the proposed controller and PI hysteresis current controller comparison, at higher speed and with greater applied load variation. In Figure 6-21 a two-step load change cycle is applied, starting at no load, increased to 10% and 20% rated respectively, and then cycled back through to no load, indicated by the numbered vertical lines 1-4. The response of the proposed controller in Figure 6-21a demonstrates an excellent response, with negligible over/undershoot and rapid convergence. The PI controller speed response in Figure 6-21b is slightly more delayed, with slower convergence to command speed; additionally, the d-axis current is not controlled ideally despite the use of the MTPA algorithm during the test.

At a higher speed the load test is performed again, this time with a step from 0-25% rated load at 165 rad/s. Figure 6-22a shows the response of the proposed controller, which demonstrates minimal over/undershoot and rapid convergence during the load transitions. The PI controller demonstrates greater over/undershoot with a slower rate of convergence to the command speed than the proposed controller.

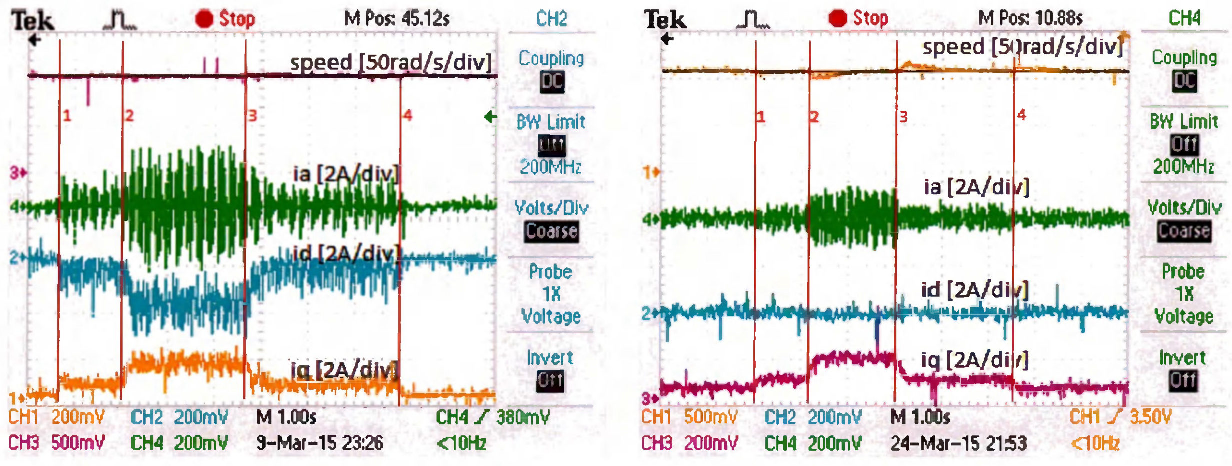

(a) (b)

Figure 6-21: Load step change of 0-10-20% at 100rad/s: a) proposed controller b) PI hysteresis current controller

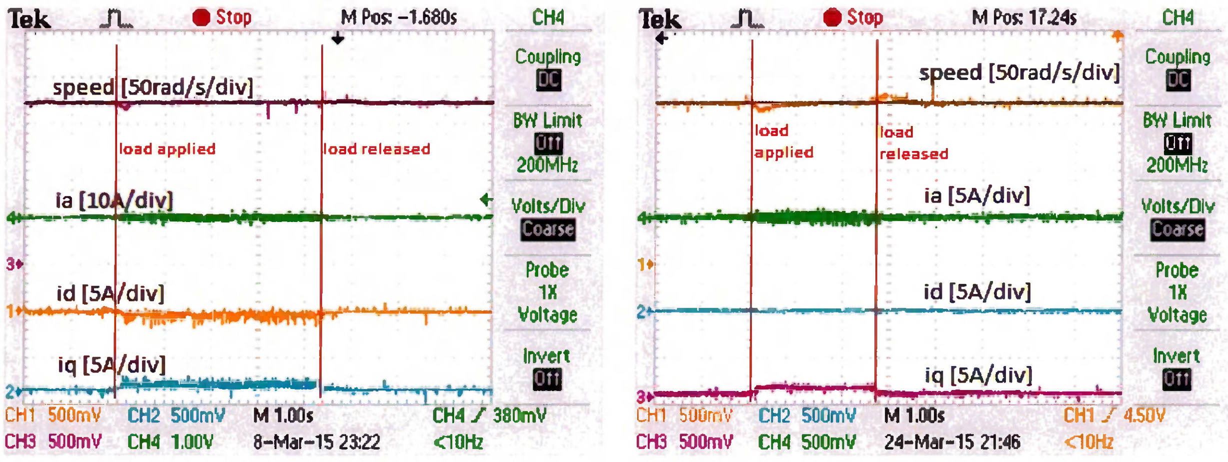

(a) (b)

Figure 6-22: Load step change of 0-25% at 165rad/s: a) proposed controller b) PI hysteresis current controller

Finally, to verify that the phase currents are balanced, the Figure 6-23 below shows the phase currents under load at a low speed to validate the assumption made for controller design. This validation is essential to confirm that the phase currents are indeed separated by ~120 degrees with closely matching magnitudes. In summary, the phase currents shown in Figure 6-23 provide confirmation of this balanced status, and thus ensure that all assumptions made for reference frame transformation are corroborated experimentally.

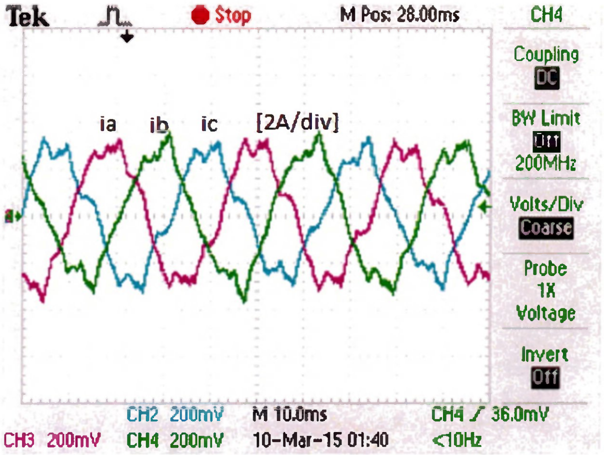

Figure 6-23: Balanced phase currents of the proposed controller

6.3 Conclusions

The proposed nonlinear controller has been thoroughly tested in a real-time experimental environment to validate its performance with a series of tests similar to that performed in simulation. A series of step speed responses have been documented in this section, rigorously demonstrating the dynamic performance of the controller. Steady state analysis of the d-q axis currents has indicated reduced harmonic content of the phase current through triplen injection. Loading tests have shown the proposed controllers ability to reject disturbances and take advantage of the d-axis current for additional reluctance torque. Performance has been compared to a conventional PI controller, with the proposed controller demonstrating faster convergence and better control of i_d during step changes and loading transitions.

Overall, the proposed controller demonstrates excellent dynamic performance and robust operation over an extended speed operating range, with rapid load disturbance rejection and improved control of the d-axis current throughout the operating range.

Chapter 7

Conclusion

The work presented in this thesis was initiated on the basis of identified need for improvement and further analysis of past work performed in the area of permanent magnet synchronous machine (PMSM) controllers. Significant research has been invested in the field of PMSM drives and applied control, with results documented for such major classes of control, including linear, nonlinear and intelligent as well as combinations thereof. Results have been reported in various works for PI type linear controllers [4], [7], [9] - [12] fuzzy logic, neuro-fuzzy and other combinations of intelligent controllers [2], [17] - [19], [25] and for model based nonlinear control [1], [13] - [16] each highlighting the benefits of that particular method.

The target of any of these various control methodologies is the same, to achieve optimal performance with maximal efficiency. The difference is in the control design approach, with each major control technique offering some kind of advantage alongside the limitations associated with the given method.

For PI type linear controllers, the advantage is simplicity of implementation and the broad knowledge base associated with years of work. Real-time implementation of PI controllers involves simple routines, permitting rapid loop execution, the key to a fast response. The minimalism of PI control comes at the cost of performance, with typical response times slower than comparable intelligent or model based controllers[16].

Intelligent controllers can provide highly accurate responses and adaptation to system dynamics as a function of their design, and if training data is available integration of neural networks can provide excellent optimization. Development requires detailed machine knowledge and/or performance data, as well as expert control theory knowledge to develop the algorithm for optimal control. Additionally, loop execution of many intelligent controllers

---

[16] Based on the DS1104 R&D environment, with a 64-bit floating point (FP) 250MHz processor

involves greater time delays than PI controllers, due to the fact that control is primarily conditional evaluations. Most MCU have dedicated math modules for rapid multiplication, however conditional statement evaluation requires multiples clock cycles to achieve, and results in extended control loop execution. Consequently, a significantly faster processor is required to provide comparable closed loop execution rates to PI controller.

Nonlinear model based control is capable of excellent performance for that class of machines, with the possibility of integrated efficiency optimization algorithms and robust stability analysis. Development of model based controllers is contingent with having an accurate mathematical model for the subject system, and requires that the model be sufficiently simple that mathematical solutions are reasonable for implementation. This class of controller requires tuning of design parameters (much like PI controllers) to achieve optimal performance, this being a principle disadvantage relative to intelligent algorithms. Notably, as model based algorithms are purely math based, the dedicated MCU math module may be employed allowing faster loop execution than intelligent controllers.

This thesis proposes a model based controller in conjuncture with parameter estimation and supplemented with optimal torque and flux weakening algorithms to achieve optimal control of the class of ac machines known as IPMSM. The basis of the controller is developed with Lyapunov model functions, and global system stability demonstrated mathematically with criterion based on Barbalat's Lemma. Load and key parameter estimation is achieved through adaptive backstepping, applied through the course of the controller development; this ensures robust operation in a dynamic operating environment. Within the rated speed range, the d-axis current is defined by MTPA algorithm, maintaining optimal torque while reducing the stator copper losses indirectly. Above rated speed[17], a field weakening is activated, effectively controlling air gap flux to maintain rated terminal voltages and indirectly reducing the core magnetic losses.

The proposed controller has been implemented in two distinct simulation environments for initial testing, indicating excellent performance for set-point and loading changes and parametric variations. Comparison of the proposed nonlinear controller has been made with PI

---

[17] The speed which corresponds to the counter EMF exceeding the rated stator winding voltages

controllers using both hysteresis current and carrier based modulation in conjuncture with the same MTPA algorithm. Results for the proposed controller indicate better load disturbance recovery than the PI controllers[18], with steady state performance comparable in terms of speed variation.

Real-time implementation has been achieved using a DS1104 embedded controller board, applied to a Yaskawa 3.7kW IPMSM motors as well as a 0.745kW induction machine (see Appendix F). Results of the proposed controller indicate excellent performance characteristics, as well as the potential for extension to the induction machine class of ac motors. Comparative results with a PI hysteresis current controller have demonstrated a clear performance advantage of the proposed controller, with improved load disturbance rejection and control of i_d over the PI current controller.

In summary, all the stated objectives have been fulfilled and demonstrated in detail through simulation and real-time testing. All mathematical models and algorithms employed in this thesis are derived from first principles, with succinct but detailed derivations provided. Full control design is demonstrated in detail, with robust stability analysis and operational limits defined in the context of the subject hardware.

7.1 Contributions

The principal contributions of this thesis work are detailed below.

> The robust stability analysis of a new nonlinear model based controller on the basis of Lyapunov stability criterion and model functions with global asymptotic stability ensured through the application of conditions supported by Barbalat's lemma.
>
> A new nonlinear controller that incorporates flux control algorithms which enable both a wide speed range of operation and facilitate improved efficiency through optimal control of the d-axis current.

---

[18] All controllers compared use MTPA

Adaptive control of the class of PMSM through the use of an adaptive backstepping technique for more robust operation and the ability to contend with machine parameter variation as a function of time, temperature and/or magnetic saturation effects.

The improvement of harmonic performance of naturally sampled modulation through triplen injection, enabling reduced torque ripple and improved supply transfer ratio.

The proposed nonlinear model based controller has been implemented in a real-time environment using the DS1104 research and development board. The steady state and dynamic performance of the proposed controller has been rigorously tested in this experimental environment with a 3.7kW IPMSM. Comparative results to a PI hysteresis current controller have demonstrated the superior performance of the proposed controller for load disturbance rejection and response to command speeds.

Several papers have been published as a function of this thesis work, and are detailed in Appendix H.

7.2 Future Work

The findings of this work have not only established the performance of the proposed controller, but through the detailed theoretical analysis and extensive real time design and troubleshooting processes many subjects for further investigation have been observed. Though the following details are far from exhaustive, principal areas for potential further work have been identified from experimental experience.

In terms of control development and potential for improvement of control algorithms, the following observations have been made.

R_s should be included in adaptive estimation, due to its significant effect on control, and the potential for age/temperature variation.

L_d may be omitted from adaptive estimation, due to the relative static nature of the parameter, see (2.6) for rationale

B_m may be omitted from adaptive estimation, as the mechanical frictional coefficient does not have a significant effect, other than boosting the response to load variation in conjuncture with load estimation.

In terms of experimental implementation, the following are observations of note.

Improve the current sensors. While the effect on control is less significant than might be thought, using a compact linear hall sensor array like the ACS715 from Allegro Microsystems is space efficient, more reliable and accurate, with factory calibration.

Compile the code from manual written C++ files, this will result in less overhead and greater run-time optimization.

Implement a torque sensor, the current lack of direct shaft torque measurement limits potential comparison and analysis, and forces approximation of loading using other techniques with high error margins.

Reduction of noise on the control and feedback pathways has been a frequent problem, better routing and shielding can help improve results.

In terms of the broad application area of the proposed work, there are several areas for further consideration.

Continue the real-time work as originally proposed for wind energy systems utilizing either surface or interior type permanent magnet synchronous machines, applied through a controlled converter (Appendix G). The key limitation is that of the converter, with the knowledge that any IGBT based inverter topology will not function in this context, as the freewheeling diodes will act uncontrolled. This means that a converter must be constructed, potentially from discrete switching components, possibly with switches not characterized by integrated body diodes[19]

---

[19] Use caution, lack of body diodes can result in switch element damage due to inductive effects.

Derive the similar controller pertinent to induction machines, there may be areas in the literature that have not yet addressed this potential. The mathematical model for induction machines is similar in many ways, with the exception of a slip torque component, and slightly varied expressions for mutual inductances and loss expressions.

References

[1] M. A. Rahman, M. Vilathgamuwa, M. Uddin and K.-J. Tseng, "Nonlinear Control of Interior Permanent-Magnet Synchronous Motor," *IEEE Transactions on Industry Applications,* vol. 39, no. 2, pp. 408-416, 2003.

[2] M. N. Uddin and R. .. Rebeiro, "Online Efficiency Optimization of a Fuzzy-Logic-Controller-Based IPMSM Drive," *IEEE Transactions on Industry Applications,* vol. 47, no. 2, pp. 1043-1050, 2011.

[3] X. Zhuang, X. Wen, F. Zhao, X. Guo and P. Zhang, "Wide-Speed-Range Sensorless Control of Interior PMSM Based on MRAS," in *ICEMS*, Incheon, 2010.

[4] H. Kajabadi and M. Ghribi, "MRAS-based Adaptive Speed Estimator in PMSM Drives," in *IEEE Advanced Motion Control*, Istanbul, 2006.

[5] J.-i. Itoh, Y. Nakajima and M. Kato, "Maximum Torque per Ampere Control Method for IPM Synchonous Motor base on V/f Control," in *IEEE PEDS*, Kitakyushu, 2013.

[6] M. N. Uddin, T. S. Radwan and M. A. Rahman, "Performance of Interior Permanent Magnet Motor Drive Over Wide Speed Range," *IEEE Transactions on Energy Conversion,* vol. 17, no. 1, pp. 79-84, 2002.

[7] Y. Shi, K. Sun, L. Huang and Y. Li, "Control Strategy of High Performance IPMSM Drive in Wide Speed Range," in *IEEE IECON*, Melbourne, 2011.

[8] G. Wang, R. Yang and D. Xu, "DSP-Based Control of Sensorless IPMSM Drives for Wide Speed Range Operation," *IEEE Transactions on Industrial Electronics* , vol. 60, no. 2, pp. 720-727, 2013.

[9] S. Fazeli, H. Ping, H. Zarchi and J. Soltani, "Robust Maximum Torque per Ampere (MTPA) Control of Interior Permanent Magnet Synchronous Motor Drives using Adaptive Input-Output Feedback Linearization Approach," in *TECHPOS*, Kuala Lumpur, 2009.

[10] S. Morimoto, Y. Tong, Y. Takeda and T. Hirasa, "Loss Minimization Control of Permanent Magnet Synchronous Motor Drives," *IEEE Transaction on Industrial Electronics,* vol. 41, no. 5, pp. 511-517, 1994.

[11] M. N. Uddin and R. S. Rebeiro, "Performance Analysis of an FLC-Based Online Adaptation of Both Hysteresis and PI Controllers for IPMSM Drive," *IEEE Transactions on Industry Applications,* vol. 48, no. 1, pp. 12-19, 2012.

[12] Z.-h. Liu and H.-m. Li, "Precise Torque Control and Reliable Field-Weakening Operation of IPMSM," in *ITEC*, Beijing, 2014.

[13] M. N. Uddin and M. M. I. Chy, "Online Parameter Estimation based Speed Control of PM AC Motor Drive in Flux-Weakening Region," *IEEE Transactions on Industry Applications,* vol. 44, no. 5, pp. 1486-1494, 2008.

[14] M. N. Uddin and M. Chy, "Development of a Nonlinear Speed Controller of IPMSM Drive Incorporating MTPA with Mechanical Parameter Estimation," in *IEMDC*, 2007.

[15] M. Karabacak and H. Eskikurt, "Speed and current regulation of a permanent magnet synchronous motor via nonlinear and adaptive backstepping control," *Elsevier Mathematical and Computer Modelling,* vol. 53, pp. 2015-2030, 2011.

[16] J. Lau and M. Uddin, "Nonlinear Adaptive Position Control of an Interior Permanent Magnet Synchronous Motor," in *IEEE Electric Machines and Drives*, San Antonio, 2005.

[17] C. Butt, M. Hoque and M. Rahman, "Simplified Fuzzy-Logic-Based MTPA Speed Control of IPMSM Drive," *IEEE Industry Applications,* vol. 40, no. 6, pp. 1529-1535, 2004.

[18] N. Oztuk and E. Celik, "Speed Control of Permanent Magnet Synchronous Motors using Fuzzy Controller based on Genetic Algorithms," *Elsevier Journal of Electric Power and Energy Systems,* vol. 43, no. 1, pp. 889-898, 2012.

[19] H. H. Choi and J.-W. Jung, "Takagi-Sugeno fuzzy speed controller design for a permanent magnet synchronous motor," *Elsevier: Mechatronics,* no. 21, pp. 1317-1328, 2011.

[20] P. Kundur, Power System Stability and Control, McGraw-Hill, 1994.

[21] S. Ozcira and N. Bekiroglu, "Direct Torque Control of Permanent Magnet Synchonous Motors," in *Torque Control*, InTech, 2011, pp. 130-151.

[22] Fujitsu, *AN706-00032-1v0-E: Coordinate Transform,* 2011.

[23] P. C. Krause, O. Wasynczuk and S. D. Sudhoff, Analysis of Electrical Machinery and Drive Systems, 2 ed., Piscataway: IEEE Press, 2002.

[24] D. Ohm, "Dynamic Model of PM Synchronous Motors," Drivetech Inc., Blacksburg, 2000.

[25] H. Chaoui and P. Sicard, "Adaptive Lyapunov-based neural network sensorless control of permanent magnet synchronous machines," *Neural Computing and Applications,* vol. 20, no. 5, pp. 717-727, 2011.

[26] H. Liu, Z. Zhu, E. Mohamed, Y. Fu and X. Qi, "Flux-Weakening Control of Nonsalient Pole PMSM Having Large Winding Inductance, Accounting for Resistive Voltage Drop and Inverter Nonlinearities," *IEEE Transactions on Power Electronics,* vol. 27, no. 2, pp. 942-952, 2012.

[27] M. Meyer and J. Bocker, "Optimum Control for Interior Permanent Magnet Synchronous Motors (IPMSM) in Constant Torque and Flux Weakening Range," in *EPE-PEMC*, 2006.

[28] P.-Y. Lin and Y.-S. Lai, "Voltage control of interior permanent magnet synchronous motor drives to extend DC-link voltage utilization for flux weakening operation," in *IECON*, 2010.

[29] K. Chang, "Loss Minimization Control of Permanent Magnet Synchronous Machine for Electric Vehicle Applications," 2013.

[30] Z. Fangyang, R. Feng, L. Jianjun and H. Peng, "Study on Flux–Weakening Control for PMSM," in *KAM International Symposium*, Sanya, 2011.

[31] H. K. Khalil, Nonlinear Systems, Upper Saddle River: Prentice Hall, 1996.

[32] J. Mash, M. Pahlevninezhad and P. Jain, "Nonlinear Control of Wind Energy Conversion System based on Control-Lyapunov Function," in *ECCE*, Denver, 2013.

[33] D. G. Holmes and T. A. Lipo, Pulse Width Modulation For Power Converters: Principles and Practice, Piscataway: IEEE Press, 2003.

[34] A. Kwasinski, P. T. Krein and P. L. Chapman, "Time Domain Comparison of Pulse-Width Modulation Schemes," *IEEE Power Electronic Letters,* vol. 1, no. 3, pp. 64-68, 2003.

[35] dSPACE GmbH, "DS1104 R&D Controller Board: Hardware Installation & Configuration," dSPACE GmbH, Paderborn, 2008.

[36] dSPACE GmbH, "DS1104 R&D Controller Board: RTLib Reference," dSPACE GmbH, Paderborn, 2008.

[37] dSPACE GmbH, "DS1104 R&D Controller Board: Features," dSPACE GmbH, Paderborn, 2008.

[38] Ametek, "Sorensen SGA Series DC Power Supplies," Ametek, 2011.

[39] D. Ohm, "Dynamic Model of Indcution Motors for Vector Control," Drivetech Inc., Blacksburg, 2000.

Appendix A

Parameters & Coefficients

This appendix provides numerical values for all system parameters, including machine, switch elements, and controller coefficients used in simulation and real-time scenarios.

Table A-1: IPMSM parameters

Parameter	Label	Value	Unit	Abbreviation/Symbol
Rated power	P_{rated}	3.7	Kilo-watt	kW
Rated voltage[20]	V_{rated}	183	volt	V
Rated current	I_{rated}	14.2	Ampere	A
Rated Frequency	f_{rated}	87.5	cycle/second	Hz
Rated speed	ω_{rated}	183.3	rad/second	rad/s
Pole pairs	n_p	3		
d-axis inductance	L_d	5.06	milli-Henry	mH
q-axis inductance	L_q	6.42	milli-Henry	mH
Stator resistance	R_s	0.242	Ohm	Ω
Inertia constant	J	0.0133	Kg(meter^2)	Kgm^2
Damping coefficient	B_m	0.001	Nm/rad/s	Nm/rad/s
Magnetic flux constant	Φ_m	0.2449	volt/rad/s	v/rad/s

Table A-2: Switch element parameters

Parameter	Label	Value	Unit
Transistor saturation voltage	V_{ce}^{sat}	2.5	V
Transistor resistance	R_{trans}	2.00E-02	Ω
Diode threshold	V_{thresh}	2	v
Diode resistance	R_{diode}	2.20E-02	Ω

---

[20] Voltages cited in line-line root mean square quantity unless otherwise specified

Table A-3: Design coefficients

Coefficient	Description	MATLAB	Co-Simulation	Real Time
Kw	speed	|25-35|[21]	17	|1200-1600|
Kd	d-axis current	2000	2000	|2000-5000|
Kq	q-axis current	3000	1200	|25-55|
nMu	mechanical coefficient	|140-160|	|7e-12|	1e-4
nLambda	load estimation	|1.3e-4|	|40-120|	|0.1-3|
nQ	q-axis inductance			

---

[21] Range indicates that the design coefficient may be varied over the operational range of the motor to attain desired operational performance

Appendix B

PSIM Co-Simulation Block

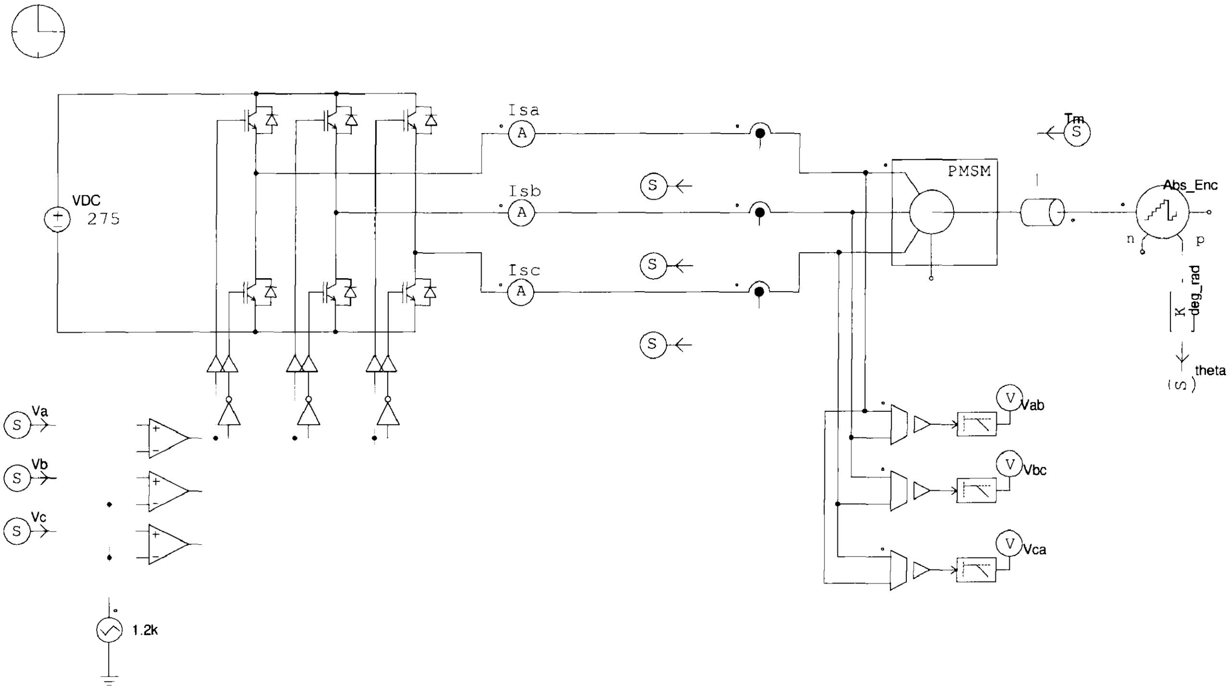

Figure B-1: Power electronics and motor drive system

Appendix C

Real-Time Block

The following diagram details the major components of the real-time implementation block, with peripheral interface modules at the left (inputs) and right (outputs) margins. All major components of the system are depicted as implemented, with reference to derived control equation numbers corresponding to appropriate functional blocks.

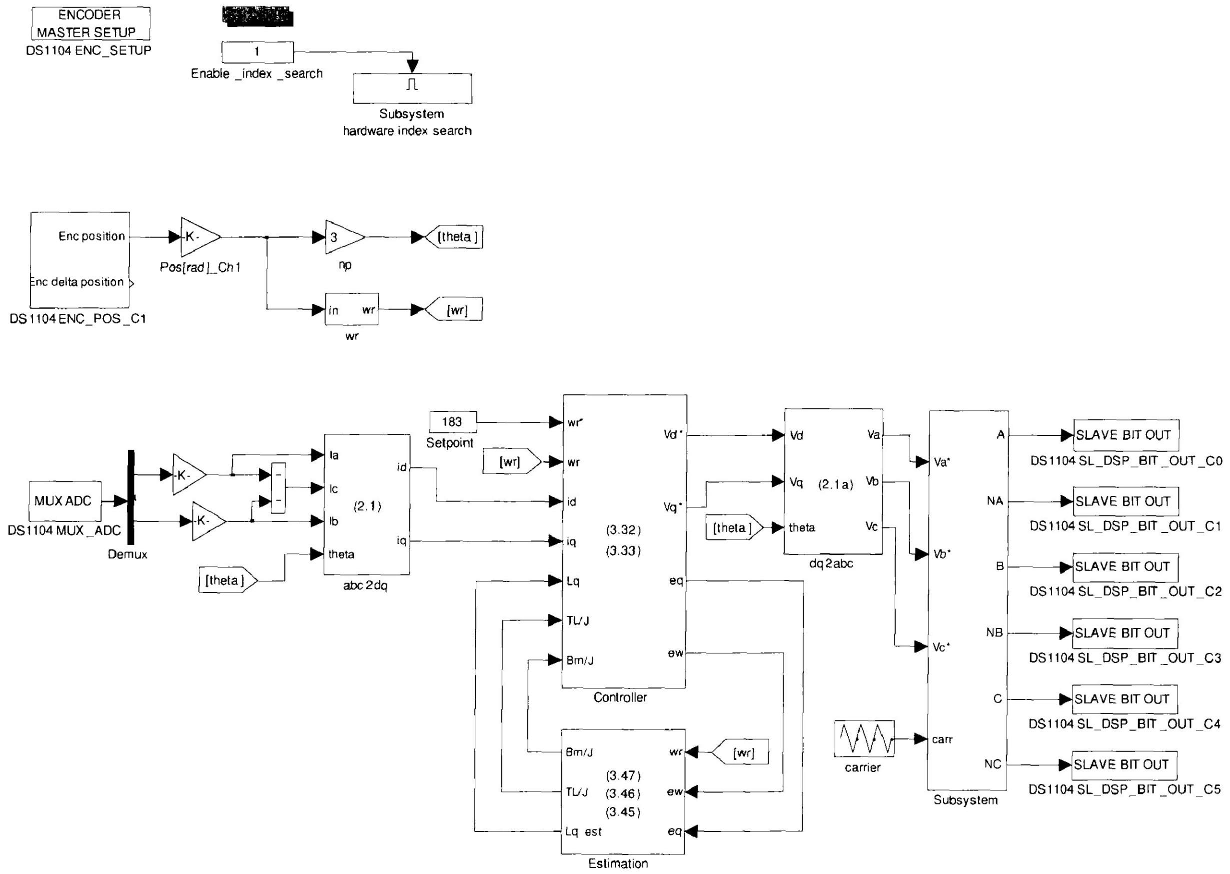

Figure C-1: Real-time Simulink blocks

Appendix D

Real-Time Hardware Interface Circuits

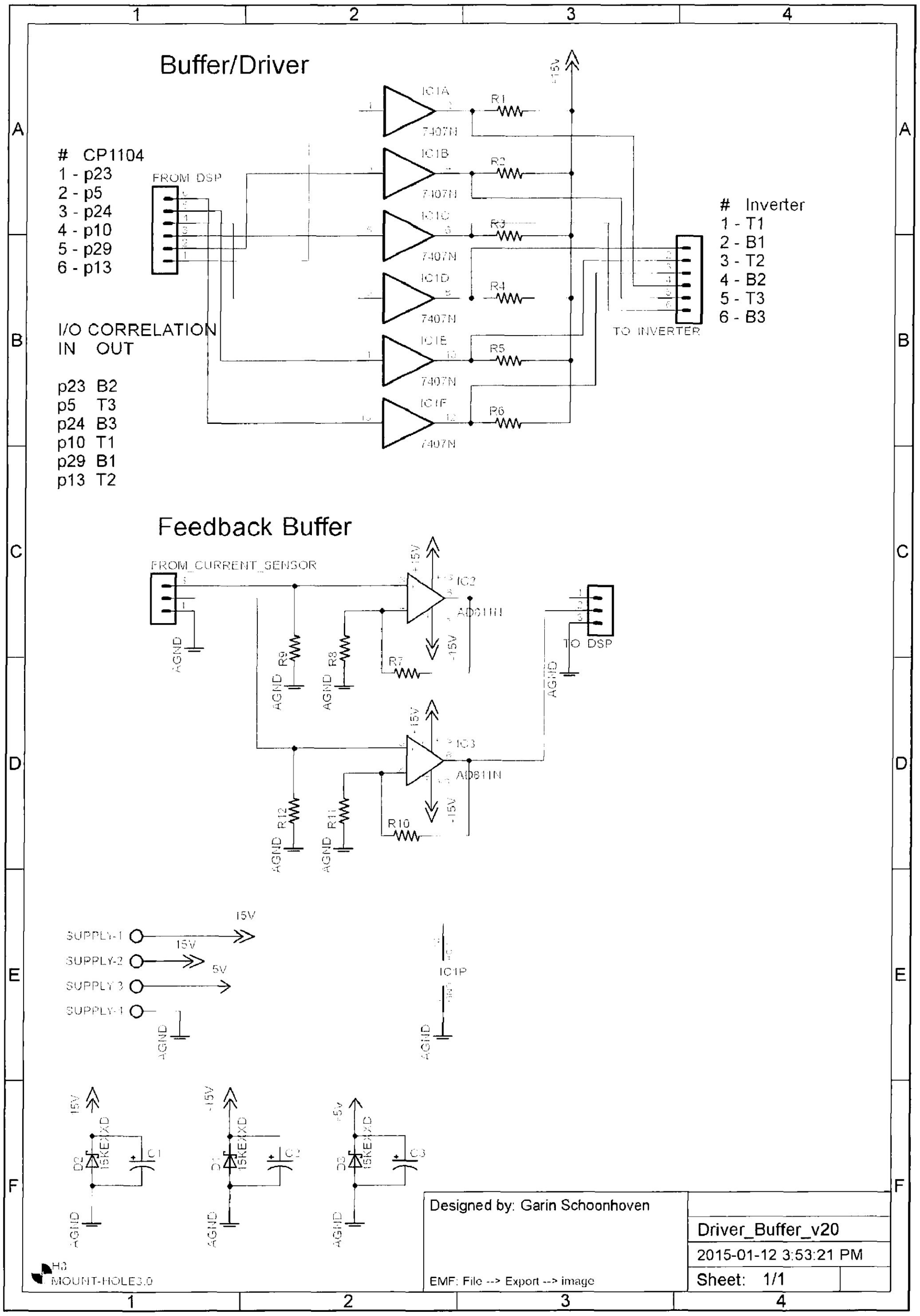

Figure D-1: Experimental interface circuit

Appendix E

DSPACE ControlDesk Interface Examples

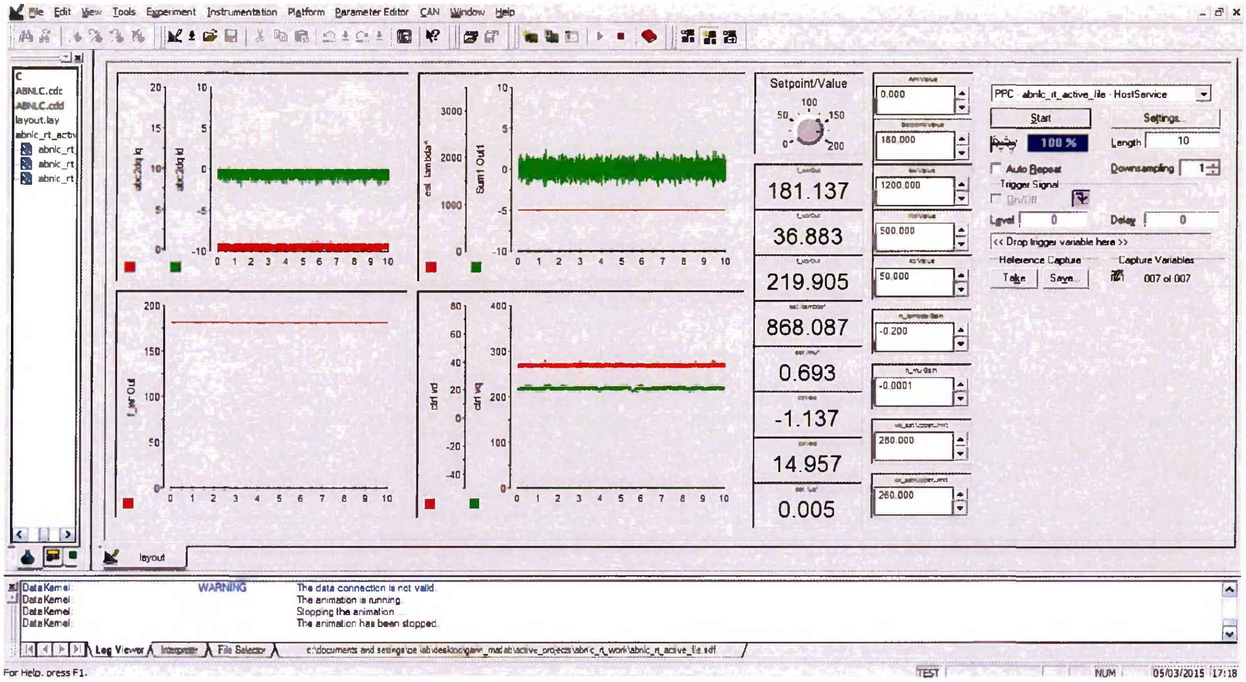

```
DataKernel:   WARNING   The data connection is not valid.
DataKernel:             The animation is running.
DataKernel:             Stopping the animation ...
DataKernel:             The animation has been stopped.
```

c:\documents and settings\pe lab\desktop\gann_matlab\active_projects\abnlc_rt_work\abnlc_rt_active_file.sdf

Figure E-1: dSPACE ControlDesk interface, steady state at rated speed, inertial load

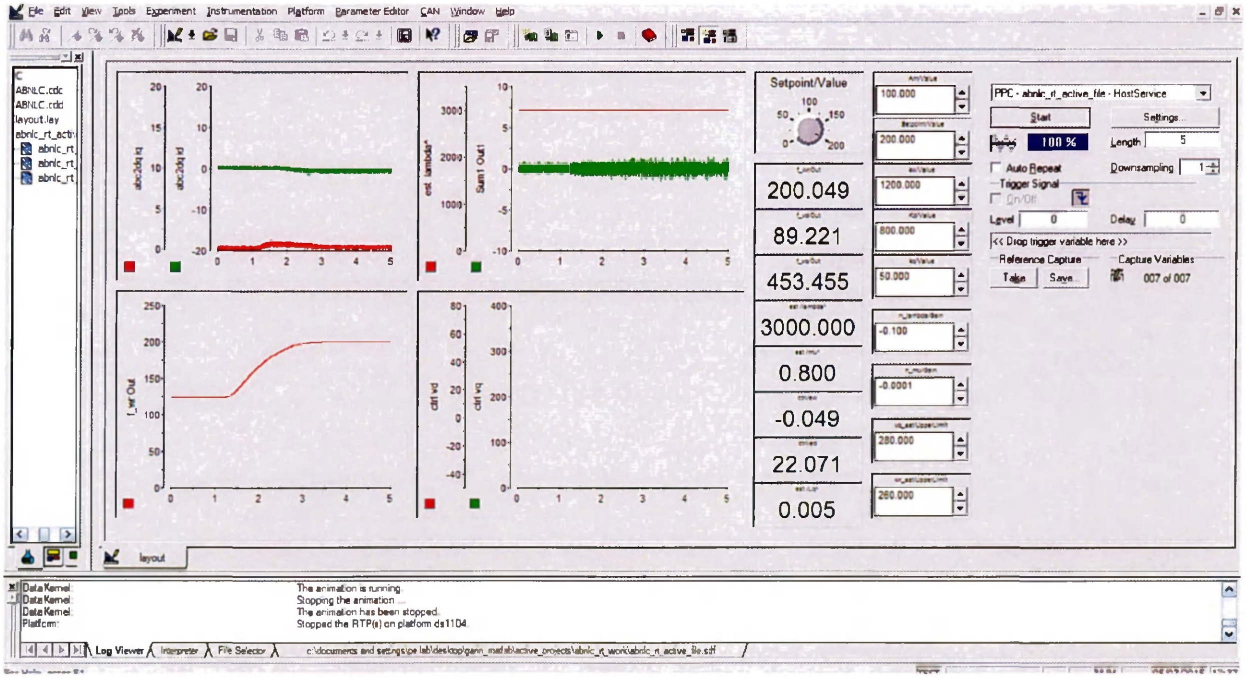

```
DataKernel:   The animation is running
DataKernel:   Stopping the animation ...
DataKernel:   The animation has been stopped.
Platform:     Stopped the RTP(s) on platform ds1104
```

c:\documents and settings\pe lab\desktop\gann_matlab\active_projects\abnlc_rt_work\abnlc_rt_active_file.sdf

Figure E-2: dSPACE ControlDesk interface, step speed reference 125-200 rad/s, inertial load

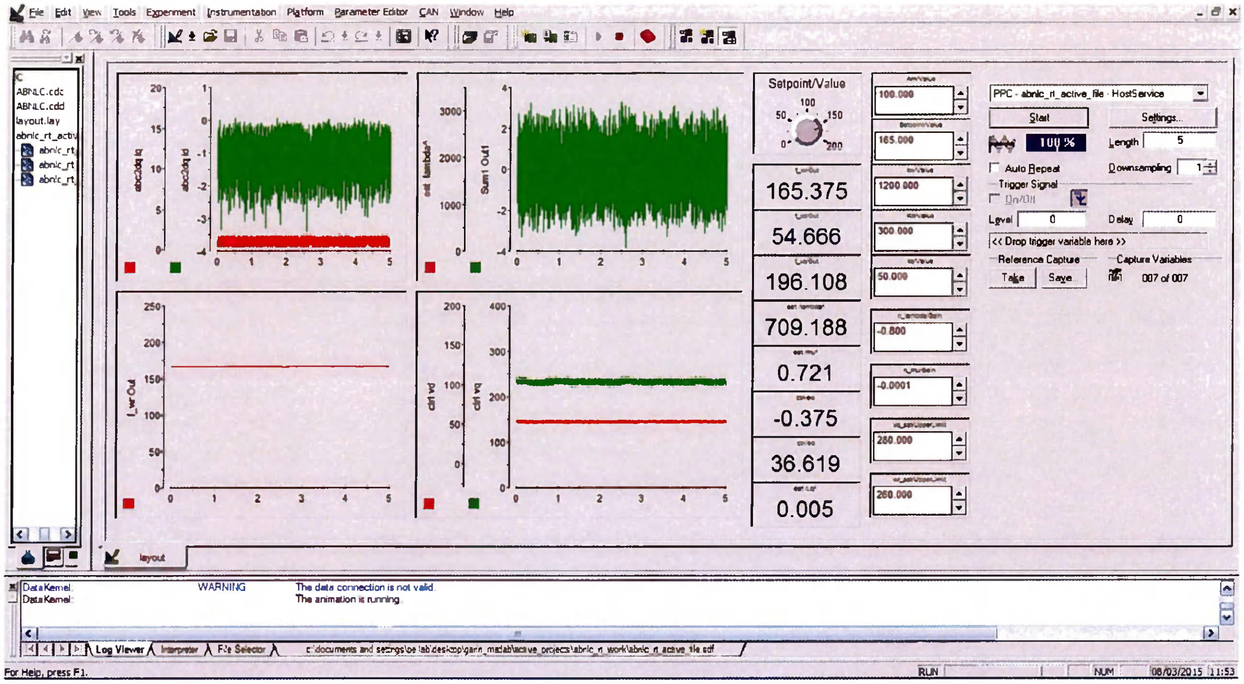

165.375
54.666
196.108
709.188
0.721
-0.375
36.619
0.005

100.000
165.000
1200.000
300.000
50.000
-0.800
-0.0001
280.000
260.000

Length 5
Downsampling 1
Level 0
Delay 0

```
DataKernel        WARNING        The data connection is not valid.
DataKernel                       The animation is running.
```

c:\documents and settings\pe lab\desktop\garin_matlab\active_projects\abnlc_rt_work\abnlc_rt_active_file.sdf

Figure E-3: dSPACE ControlDesk interface, steady state, 165 rad/s, 20% rated load

Appendix F
Application to Induction Motors

This appendix details results from application of the proposed nonlinear controller to cage type induction machines. Due to the inherent similarities between the induction and PMSM, it is possible to directly (with tuning) apply the proposed controller to an induction machine. The dynamic general model of the induction machine is presented below [39], with stator variables referred to the rotating rotor reference frame, as the PMSM model is developed in the main part of this thesis.

$$\begin{aligned} V_{ds} &= R_s i_{ds} - \omega_s \phi_{qs} + \tfrac{d}{dt}\phi_{ds} \\ V_{qs} &= R_s i_{qs} + \omega_s \phi_{ds} + \tfrac{d}{dt}\phi_{qs} \end{aligned}$$

With the stator flux quantities as follows:

$$\begin{aligned} \phi_{ds} &= L_s i_{ds} + L_m i_{dr} \\ \phi_{qs} &= L_s i_{qs} + L_m i_{qr} \end{aligned}$$

Notably, to derive control laws, it is necessary to express the system equations above in terms of only rotor referred stator state variables. Towards this end, the equations below may be used.

$$\begin{aligned} i_{dr} &= \tfrac{1}{R_r}\left(\omega_r \phi_{qr} - \tfrac{d}{dt}\phi_{dr}\right) \\ i_{qr} &= \tfrac{1}{R_r}\left(-\omega_r \phi_{dr} - \tfrac{d}{dt}\phi_{qr}\right) \\ \phi_{dr} &= L_m i_{ds} + L_r i_{dr} \\ \phi_{qr} &= L_m i_{qs} + L_r i_{qr} \end{aligned}$$

As the proposed controller is derived specifically for PMS machines, this additional section is intended as only as a side note to demonstrate robustness, and is thus relegated to the appendix. However, based on the model shown above, it is possible to derive the same controller specifically for induction type machines, which would have a similar structure to the proposed controller, and only differ in the nominal values of mutual inductances, phase resistance, mechanical frictional coefficient, etc.

The step speed response of the proposed controller applied to an induction motor is shown in Figure F-1, and illustrates the speed response and phase current.

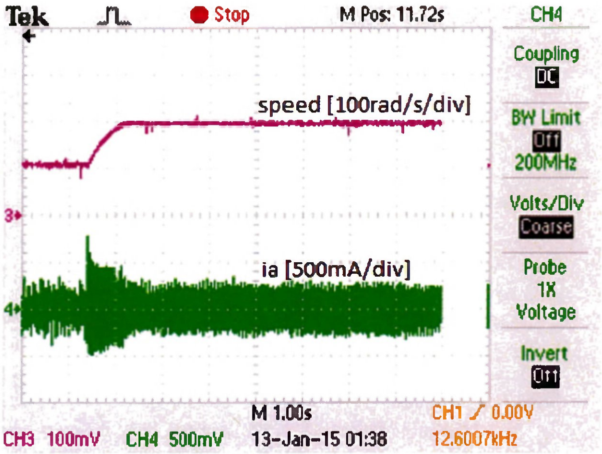

Figure F-1: Induction motor, step speed response 100-183 rad/s, light load: Speed (top) & phase current (bottom)

The steady state operation of the induction machine under control of the proposed controller is shown in Figure F-2, and demonstrates the phase current at rated speed operation, with only an inertial load.

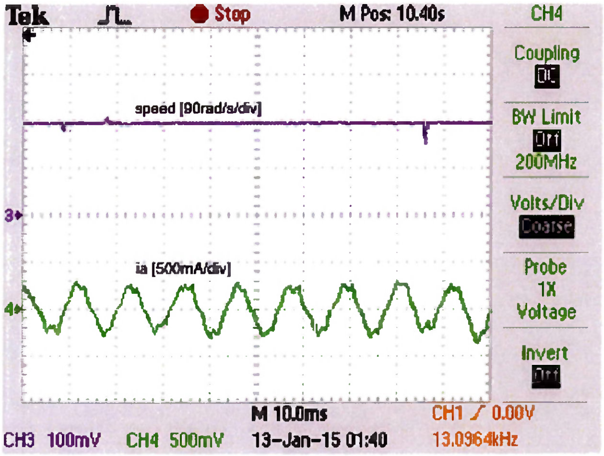

Figure F-2: Induction motor, steady state, 183 rad/s, light load: speed (top) & phase current (bottom)

In Figure F-3, the speed response for a step increase and decrease above rated speed is shown, and demonstrates the accurate speed control possible using the proposed controller.

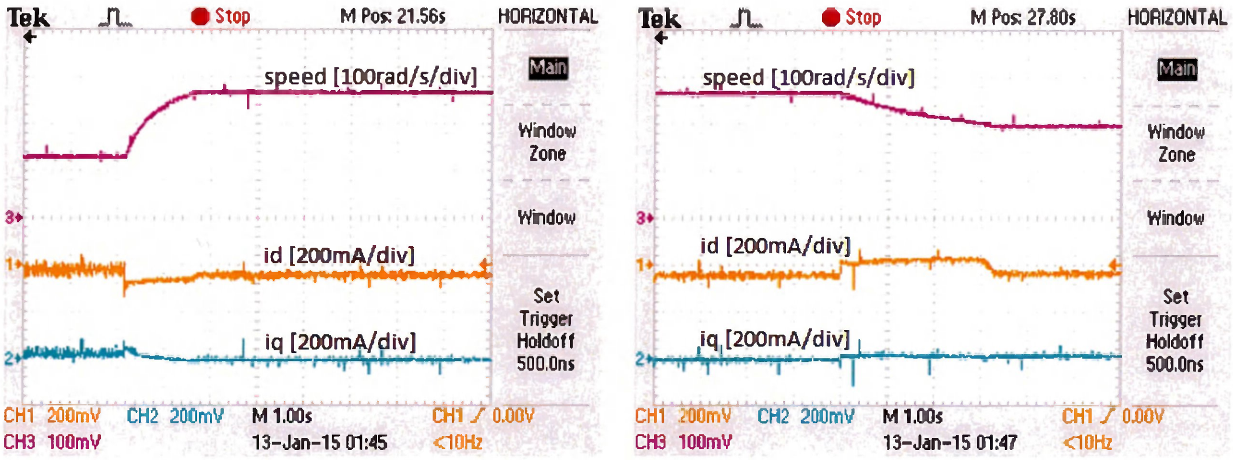

(a) (b)

Figure F-3: Induction motor, step speed change, light load: a) 120-250 rad/s b) 250-183 rad/s

Finally, a load variation is applied to the induction motor at rated speed, with the speed response shown in Figure F-4. The estimated load is also shown on the oscilloscope image, and demonstrates the rapid convergence of the proposed controller to the command speed following a load disturbance.

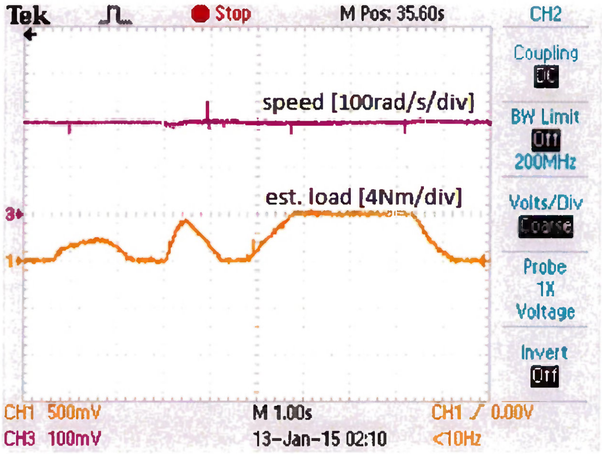

Figure F-4: Induction motor, rated speed, estimated load & speed response

To achieve improved performance, the d-q axis equivalent inductances were modified. Control gains were also adjusted as necessary to achieve optimal performance. While the control exhibited acceptable performance, it is a model based controller for PMSM machines and thus not specifically designed to drive induction machines and should not be used with the expectation of ideal performance. These results are provided merely as a proof of concept, to illustrate the similarities between PMSM and induction machines.

Appendix G

Application to Wind Energy Systems

Original work for the proposed controller began as a solution to the wide speed range operation of wind turbines in wind energy systems. The principle of operation for interior permanent magnet synchronous generators is identical to IPMSM, the only exception being the opposite current flow in the mathematical model. Thus, control laws are similar, while requiring a full derivation from the generator model. These control laws are shown below, with the knowledge that development of the laws is identical.

The derived stabilizing command voltage expressions:

$$v_d = \left\{ \begin{array}{l} -R_s i_d - \alpha n_p \omega_r \hat{L}_q i_q + \alpha k_d e_d \hat{L}_d + \frac{2\alpha(1-n)(\hat{L}_d - \hat{L}_q)\hat{L}_d}{\phi_m} i_q \dot{i}_q \\ -n\alpha\left(\frac{V_m^{'}}{n_p \omega_r^2} + \frac{n_p \hat{L}_q^2}{2V_m^{'}} (\dot{\omega}_r i_q^2 + 2\omega_r i_q \dot{i}_q) \right) - \frac{3\alpha n_p (\hat{L}_d - \hat{L}_q)\hat{L}_d e_\omega i_q}{2J} \\ + \frac{3\alpha n_p (\hat{L}_d - \hat{L}_q)\hat{L}_d e_\omega i_q}{2Je_d} \left(\frac{(1-n)(\hat{L}_d - \hat{L}_q) i_q^2}{\phi_m} - \frac{n}{\hat{L}_d}\left[\phi_m - \frac{V_m^{'}}{n_p \omega_r} + \frac{\hat{L}_q^2 n_p \omega_r}{2V_m^{'}} i_q^2 \right] \right) \end{array} \right\}$$

$$v_q = \left\{ \begin{array}{l} -R_s i_q + \alpha k_q e_q \hat{L}_q + \alpha n_p \phi_m \omega_r + \alpha n_p \hat{L}_d \omega_r i_d - \frac{3\alpha n_p \phi_m \hat{L}_q e_\omega}{2J} \\ + \frac{2\alpha J \hat{L}_q}{3n_p \phi_m} \left[\dot{\hat{\lambda}} - \hat{\mu}\dot{\omega}_r + k_\omega \dot{\omega}_r^{*} - \left(\frac{B_m + k_\omega J}{J} \right)\left(\hat{\lambda} - \frac{3n_p(\hat{L}_d - \hat{L}_q)}{2J} i_d i_q - \frac{3n_p \phi_m}{2J} i_q - \hat{\mu}\omega_r \right) \right] \end{array} \right\}$$

The error dynamics for estimated parameters are shown below:

$$\dot{e}_D = \frac{1}{n_D}\left[\begin{array}{l} \frac{2(1-n) i_q \dot{i}_q e_d}{\phi_m} + \frac{i_d i_q e_q}{\phi_m}\left(\frac{B_m + k_\omega J}{J} \right) + \frac{3(1-n) n_p (L_d - L_q) i_q^3 e_\omega}{2J\phi_m} \\ -\frac{3nn_p e_\omega i_q}{2JL_d}\left(\phi_m - \frac{V_m^{'}}{n_p \omega_r} \right) - \frac{3n_p i_q e_\omega e_d}{2J} + \frac{n_p \omega_r i_d e_q}{L_q} \end{array} \right]$$

$$\dot{e}_Q = \frac{1}{n_Q}\left[\begin{array}{l} \frac{3nn_p e_\omega i_q}{2JL_d}\left(\phi_m - \frac{V_m^{'}}{n_p \omega_r} \right) - \frac{2(1-n) i_q \dot{i}_q e_d}{\phi_m} + \frac{3n_p i_q e_\omega e_d}{2J} - \frac{i_d i_q e_q}{\phi_m}\left(\frac{B_m + k_\omega J}{J} \right) \\ -\frac{3(1-n) n_p (L_d - L_q) i_q^3 e_\omega}{2J\phi_m} - \frac{nn_p L_q e_d}{L_d V_m^{'}} (\dot{\omega}_r i_q^2 + 2\omega_r i_q \dot{i}_q) - \frac{n_p \omega_r i_q e_d}{L_d} \end{array} \right]$$

$$\dot{e}_{\lambda} = \frac{1}{n_{\lambda}}\left[-\frac{2(B_m + k_{\omega}J)e_q}{3n_p\phi_m} - e_{\omega}\right]$$

$$\dot{e}_{\mu} = \frac{1}{n_{\mu}}\left[\frac{2(B_m + k_{\omega}J)\omega_r e_q}{3n_p\phi_m} + \omega_r e_{\omega}\right] = -\frac{n_{\lambda}}{n_{\mu}}\omega_r \dot{e}_{\lambda}$$

The topologies for three typical wind energy systems are shown in Figure G-1, the doubly fed induction generator (DFIG) requires external excitation for the rotor magnetic field. Slip rings are required for transfer of current through the rotor windings, and thus entail maintenance.

The squirrel cage induction generator (SCIG) uses the principle of magnetic induction to induce current in the stator windings when rotated at slightly above rated speed, requiring an external capacitor bank or supply for excitation current. Once the air gap magnetic field is established, the machine will be operating as a generator.

The permanent magnet synchronous generator (PMSG) provides higher power density due to the rotor construction, and enables a wider speed operation range through the use of flux control methods applied through three-phase controlled conversion to DC.

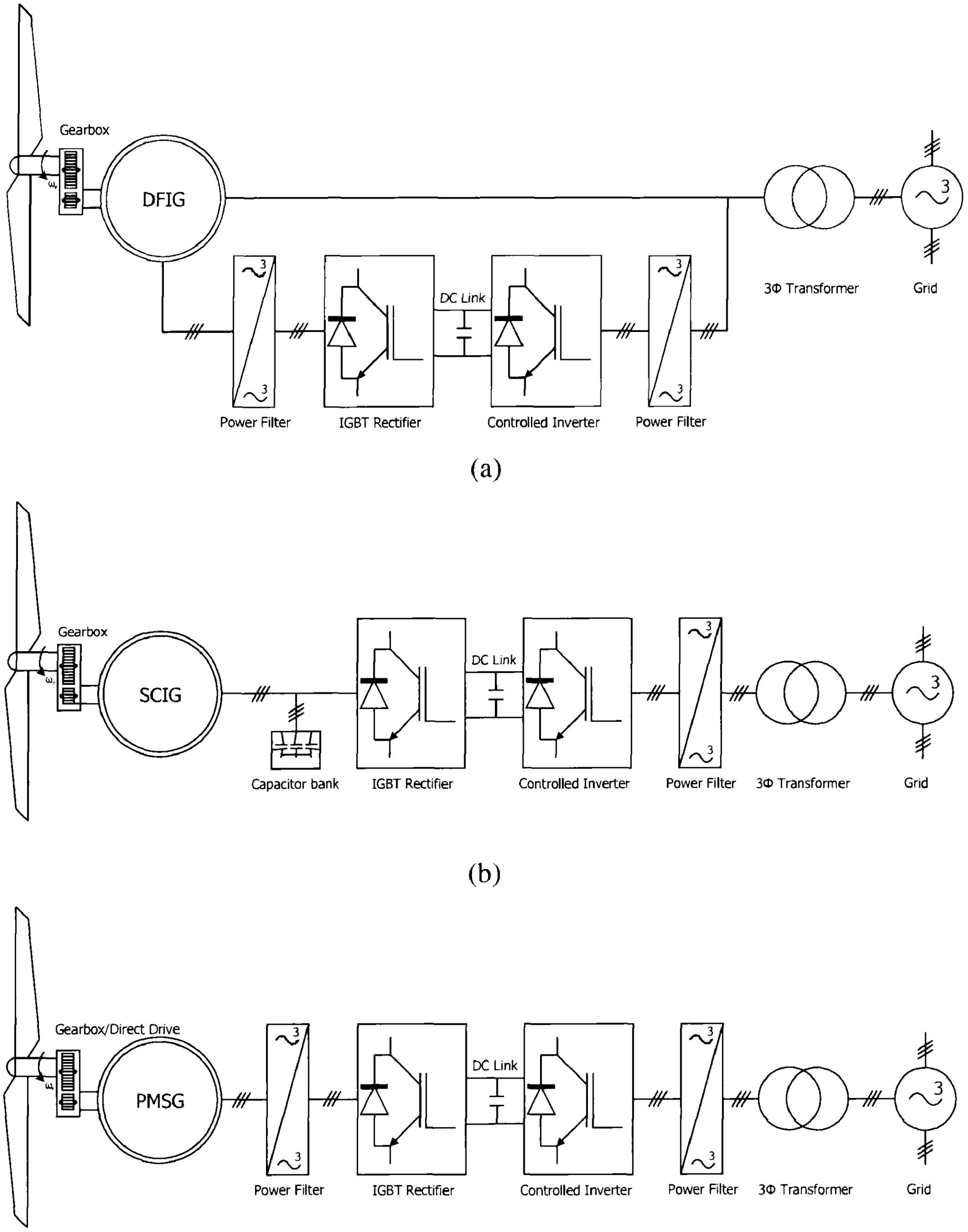

(a)

(b)

(c)

Figure G-1: Wind energy system topologies: a) DFIG b) SCIG c) PMSG

The proposed controller applied to wind energy conversion systems is shown in Figure G-2 and includes adaptive nonlinear control with critical parameter estimation for a wide speed range and robust operation. The maximum power tracking algorithm is shown for completeness only and illustrates the basic concept expressed in the form of a typical rule based algorithm for convergence to maximum power.

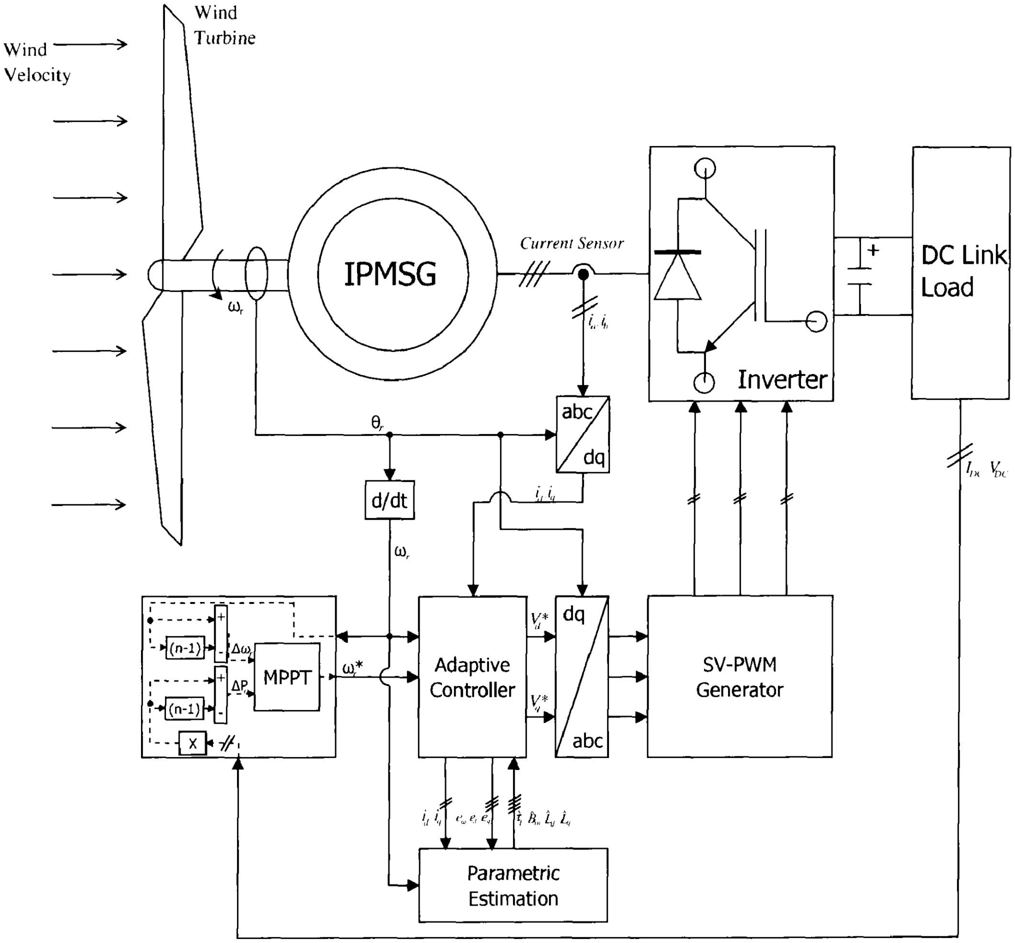

Figure G-2: Proposed wind energy conversion system

Appendix H

Associated Publications

Published/Accepted

1) Schoonhoven, G.M., Uddin M.N. "Wide speed range operation of PMSM drives using nonlinear flux control techniques" - ICECE 2014, Dhaka, Bangladesh, pp. 603 – 606.

2) Schoonhoven, G.M., Uddin M.N. "MTPA and FW based robust nonlinear speed control of IPMSM drive using Lyapunov stability criterion" – Proceedings of IEEE IAS 2014 Annual Meeting, Vancouver, Canada, pp. 1 – 8

3) Schoonhoven, G.M., Uddin M.N. " Adaptive Nonlinear Speed Control of IPMSM with Increased Linear modulation Range for Natural Sampling" – PEDS 2015, Sydney, Australia

Submitted

1) Schoonhoven, G.M., Uddin M.N. "Harmonic Injection based Adaptive Control of IPMSM Motor Drive for Reduced Motor Current THD", IEEE IAS 2015 Annual Meeting, Dallas, Texas